Politecnico di Milano

Scuola di Ingegneria Industriale e dell'Informazione

Master degree (M. Sc.) in Engineering Physics

Department of Physics

Design and fabrication of a four-arm integrated photonic interferometer for quantum enhanced multiphase estimation

Supervisor: Dr. Roberto Osellame   Candidate

Co-supervisor: Dr. Giacomo Corrielli   Raffaele Farinaro

                                               ID: 875121

Academic Year: 2017-2018

«A poet once said, '*The whole universe is in a glass of wine.*' We will probably never know in what sense he meant it, for poets do not write to be understood. But it is true that if we look at a glass of wine closely enough we see the entire universe. There are the things of physics: the twisting liquid which evaporates depending on the wind and weather, the reflection in the glass; and our imagination adds atoms. The glass is a distillation of the earth's rocks, and in its composition we see the secrets of the universe's age, and the evolution of stars. What strange array of chemicals are in the wine? How did they come to be? There are the ferments, the enzymes, the substrates, and the products. There in wine is found the great generalization; all life is fermentation. Nobody can discover the chemistry of wine without discovering, as did Louis Pasteur, the cause of much disease. How vivid is the claret, pressing its existence into the consciousness that watches it! If our small minds, for some convenience, divide this glass of wine, this universe, into parts - physics, biology, geology, astronomy, psychology, and so on - remember that nature does not know it! So let us put it all back together, not forgetting ultimately what it is for. Let it give us one more final pleasure; drink it and forget it all!»

Richard P. Feynman

Abstract

In this thesis work, we present the fabrication and the full characterization of the components required for the realization of an integrated photonic multi-mode interferometer. In particular, two distinct 4-modes coherent optical splitters (quarters) are fabricated in two glass substrates by means of femtosecond laser waveguide writing. Interestingly, this fabrication techniques allows for a three-dimensional prototyping of the devices, that can therefore be fabricated in a simple and cost-effective fashion. The optical characterization of the quarters testified their correct functioning, with an average power division of $25\% \pm 0.16\%$ among all possible input-output channels. Each of the two optical chips incorporate six thermo-optics phase shifters, for both ensuring a balanced phase-operation of the quarters, and for the active manipulation of all the internal phases of the interferometer. Each phase shifter allows to provide a full 2π modulation on its optical mode with a maximum power dissipation of 500 mW, and with reduced cross talks to the other modes. As it will be discussed thorough the thesis, the realization of these low-loss and reliable quarters required to improve beyond the state of the art both the optical circuit inscription and the micro-heaters deposition processes. The devices presented can be considered ready for being combined by butt coupling and glued, in order to complete the realization of a four-modes reconfigurable interferometer. We expect that this device will have a strong impact in the field of quantum metrology, as it enables the robust benchmarking of several protocols of quantum multi-parameters estimation, with a precision beyond the Standard Quantum Limit.

Sommario

La metrologia è la scienza della misura e si occupa diverse attività, dalla definizione delle unità di misura alla realizzazione degli standard sperimentali, come anche dello sviluppo di nuove tecniche per effetturare le misure. Con particolare riferimento all'ultimo decennio, un'area di ricerca affine si è sviluppata: la metrologia quantistica. Essa sfrutta delle risorse quantistiche, come gli stati squeezed o entangled, per aumentare l'accuratezza nella stima di un parametro fisico ignoto rispetto ad un approccio classico. In particolare ha come obiettivo quello di superare lo Standard Quantum Limit (SQL), che rappresenta il limite di accuratezza massimo in una misura classica a causa della presenza di rumore. Assieme all'importante sviluppo delle tecnologie quantistiche avvenuto negli ultimi anni, la metrologia quantistica ha trovato importanti applicazioni. Quella più di successo dimostrata ad oggi è sicuramente la rivelazione di onde gravitazionali tramite l'utilizzo di stati coerenti spremuti (squeezed state). Altre applicazioni si trovano nella biologia quantistica, dove molti esperimenti sono limitati dai danni prodotti dalle sorgenti ottiche. Non potendo aumentare l'intensità per migliorare la risoluzione, con sistemi entangled si può massimizzare quest'ultima senza danneggiare il campione. Altre applicazioni possono essere la sincronizzazione degli orologi e la litografia, giusto per citarne alcune.

Nel caso di un singolo parametro da stimare, il limite massimo di precisione è dato dal limite fondamentale di Heisenberg. E' possibile dimostrare che in questo caso possiamo sempre ottenere il risultato massimo. Il problema sta nel fatto che un grande numero di problemi coinvolge più di un singolo parametro fisico, come nel caso dell'imaging delle fasi. La piattaforma più adatta per implemen-

tare un algoritmo di stima multi-fase è rappresentato da interferometri integrati a più braccia, nei quali vengono iniettati stati di multi-fotone. Questi dispositivi presentato una serie di vantaggi in termini di stabilità, tunabilità e compattezza.

Lo scopo di questa tesi è quello di disegnare, fabbricare e caratterizzare un interferometro fotonico integrato a quattro braccia. Questo disposivito, composto dalla cascata di due diversi splitter a quattro porte chiamati quarter, è scritto in un substrato di vetro tramite la tecnica della Femtosecond Laser Micromachining (FLM). Questa ci permette di ottenere una grande flessibilità nel design e un'ottima stabilità del circuito. In entrambi i circuiti, 6 parametri interni possono essere attivamente controllati attivando degli sfasatori termo-ottici. Questa alta riconfigurabilità permette al dispositivo di essere usato sia per misure super risolute a singolo parametro che per implementare algoritmi di stima multi-fase. Un'ottimizzazione del processo di fabbricazione di questi sfasatori termo-ottici è stato condotto all'interno di questo lavoro di tesi. Una completa caratterizzazione dei due quarter è stata svolta, confermando un comportamento in linea con le specifiche di progetto. L'esperimento finale, che utilizzerà stati di luce non classica, verrà condotto nel QUANTUM LAB del Dipartimento di Fisica dell'Università La Sapienza a Roma, ma non riguarda lo scopo di questa tesi.

Contents

List of Figures

List of Tables

Introduction

Metrology is the science of measurement and it regards several aspects, from the definition of the unity of measurements until the realization of the standards units, as well as the the development of new methods of measurement. It is especially during the last decades that a research area named quantum metrology has been developed. Quantum metrology aims to exploit quantum resources, such as squeezed and entangled states, to enhance the sensitivity in the estimation of unknown physical parameters with respect to classical approaches. In particular its aim is to devise measurement strategies with sensitivity beyond the Standard Quantum Limit (SQL), which is the sensitivity bound for classical measurements due to the presence of noise. Together with the important developments of quantum technologies obtained in the past years, quantum metrology has found a number of important applications. The most successful one demonstrated so far is the detection of gravitational waves by employing quantum squeezed states. Other applications can be found in quantum biology, where optical damage is a limiting factor in many experiments. Since we cannot improve the precision by simply increasing the optical power, with entangled photons we can maximize the accuracy without damaging the sample. Other application are clock synchronization and lithography, just to cite some. In the single parameter case, the estimation of an unknown physical quantity with quantum resources is bounded by the fundamental Heisenberg limit. It is possible to demonstrate that, in this case, the optimal limit for single parameter estimation can be always saturated. The problem is that a large variety of estimation problems involve more than a single physical quantity, such as phase imaging. The most suitable platform

to implement multiphase estimation algorithms is provided by integrated multi-arm interferometers injected by multiphoton states. Such devices present several advantages in terms of stability, tunability and compactness.

The aim of this thesis work is the design, the fabrication and the characterization of an integrated photonic four-mode interferometer. This device, made up by the cascade of two different four-port splitters chips called quarters, is written in a glass substrate through the Femtosecond Laser Micromachining (FLM) technique. This technique allows for a great flexibility in the design and an optimal stability of the circuit. In both chips, 6 internal parameters can be actively controlled by operating thermo-optical phase shifters. This high reconfigurability allows this device to be used both to perform quantum-enhanced single phase measurement and to implement quantum multiphase estimation task. An optimization of the fabrication method of these thermal-shifter has been conducted during this thesis work. An extended characterization of the two quarter is performed, revealing a behavior faithful to the design specifications.

The thesis is organized as follows. The firsts three chapters are focused on the basics and theoretical background. In Chapter 1 the basics of quantum metrology and some of its applications are discussed. Chapter 2 deals with the basic principles of femtosecond laser micromachining technique. Chapter 3 is dedicated to the description of the experimental setup and the characterization method employed in the development of the integrated circuits. In the following chapters, instead, the fabrication and the characterization of the four-arm interferometer elements are presented. In Chapter 4 it is explained the aim of the experiment and the general design of the circuit. In Chapter 5 there is a full treatment regarding the fabrication of the optical device. The realization and characterization of the thermal phase shifter is presented in Chapter 6. The final experiment, which will employ no-classical light states, will be conducted in the QUANTUM LAB of the Physics Department of La Sapienza University in Rome, but lies outside the aim of this thesis work.

Quantum metrology

1.1 History of metrology

«And the whole earth was of one language, and of one speech. And it came to pass, as they journeyed from the east, that they found a plain in the land of Shinar; and they dwelt there. [...] And they said, Go to, let us build us a city and a tower, whose top may reach unto heaven; and let us make us a name, lest we be scattered abroad upon the face of the whole earth. And the LORD came down to see the city and the tower, which the children of men builded. And the LORD said, Behold, the people is one, and they have all one language; and this they begin to do: and now nothing will be restrained from them, which they have imagined to do. Go to, let us go down, and there confound their language, that they may not understand one an other's speech. So the LORD scattered them abroad from thence upon the face of all the earth: and they left off to build the city. Therefore is the name of it called Babel; because the LORD did there confound the language of all the earth: and from thence did the LORD scatter them abroad upon the face of all the earth.»

(Gen. 11, 1-9)

THE history of the Tower of Babel is one of the most known passages of the Bible and it is an origin myth meant to explain why people in the world speak different languages. Even though it's a very old (and fictional) story, it can still teach us something: when people understand each other with ease, speaking the same language, even building a tower to reach the sky is possible. What if, centuries after, humans decided not to build a tower, but a worldwide community of people that wants to systematically study the structure of the physical world through observations and experiments? We have learned that, in order to achieve big results, people need to speak the same language. This task, however, is not easy to achieve. Even though the need of a unique system for measuring the physical quantities was already clear in the ancient times, every population developed its own units system. With the rise of the big empires, first local standardization attempts took place. But we have to wait until the French revolution to witness the born of the modern metrology as the science of measurement, together with the metric system, which, in 1960, evolved in our International System of Units [1]. This common understanding of units is crucial in linking human activities [2]. Metrology is divided into three basic overlapping tasks. The first one is the definition of the units of measurement for each observable quantity. The second one is the realization of the model units in practice. The last one is the creation of protocols for traceability, which regards the linking of practical measurements to the reference standards. Nowadays, almost all fundamental units are derived from invariant constants of nature, such as the speed of light and the triple point of water, which can be observed and measured with great accuracy. The sole exception is the unit of mass, which is defined by a physical artifact, the international prototype kilogram certified in 1889, consisting in a cylinder made of platinum-iridium, with nominal mass of one liter of water at the freezing point at 1 bar. [3]. The stability of the mass unit defined in this way has been a matter of significant concern, since it has lost around 50 micrograms since it was created. A proposed revision based entirely in terms of constants of nature is indeed expected to be put into effect in May 2019[1]. Once measurements units are defined and realized, we need to study their traceability, that is "the property of a measurement result whereby the result can be related to a reference through a documented unbroken chain of calibrations, each contributing to the measurement uncertainty", as stated in the "International Vocabulary of Metrology". The

---

[1]During the writing of this thesis, the new kilogram unit has been proposed. In this redefinition, the unit of mass will be linked to the fixed value $6.62607015 \cdot 10^{-34}$ of the Planck constant h when expressed in $kg \cdot m^2/s$.

concept of uncertainty has a key role in this definition and it's highly correlated with the method of measurement adopted. In particular quantum mechanics tells us that what we thought as the lower limit of accuracy in a measurement can be overcome down to an unavoidable bound, as we will explain in the next sections.

1.1.1 From classical to quantum metrology

Any measurement can be described by a three parts algorithm: the preparation of a probe, its interaction with the system to be measured, and the probe readout. This process is often plagued by systematic or statistical errors. The former derives from a bad implementation of the set-up, like an offset in the measure, and once individuated can be, in theory, removed. The source of the latter can be accidental or fundamental. It is accidental when it derives from an insufficient control of the probes and the measured system, like laser flactuations and vibrations, or from the finite resolution of the instrumentation. It is fundamental when it derives from a physical reasoning, like the Heisenberg uncertainty relations.

Taking into account just the statistical errors, the measured value ϕ of a quantity ϕ_0 will be:

$$\phi = \phi_0 \pm \Delta\sigma \tag{1.1.1}$$

in which $\Delta\sigma$ is the uncertainty related to the statistical errors. Whatever their origin, we can reduce their effect by repeating the measurement and averaging the resulting outcomes. This is a consequence of the central-limit theorem, stating that: given a large number n of independent measurement results (each one having an associated uncertainty $\Delta\sigma$), their average will converge to a Gaussian distribution with standard deviation $\frac{\Delta\sigma}{\sqrt{n}}$. This means that, repeating the measure, Equation 1.1.1 becomes:

$$\phi = \phi_0 \pm \Delta\phi \tag{1.1.2}$$

where $\Delta\phi$ is the uncertainty of measurement that can be expressed as:

$$\Delta\phi \geq \frac{\Delta\sigma}{\sqrt{n}} \tag{1.1.3}$$

The same result is achieved when our measure is performed by n independent probe, for example n photons. We typically refer to its lower bond in Equation 1.1.3 as the Standard Quantum Limit (SQL). This level of precision is very hard

to achieve in practice, due to all possible causes of extra noise, for example the technical noise (due to imperfection of the instrumentation). Still, SQL precision can be reached in practical measurements [4] and, possibly, overcome [5]. Indeed the SQL is not a fundamental quantum mechanical bound, as it arises from a non optimality in the choice of the preparation of the system in use. It can be surpassed by using "non-classical" strategies, quantum effects, such as entanglement among the probing devices or by the usage of squeezed states. Also in this new scenario, however, theory tells us that the precision of measurements cannot be infinite, and new fundamental bounds replace the SQL [6]. Quantum metrology studies these bounds and the (quantum) strategies which allow us to attain them. In general, this discipline deals with measurement and discrimination procedures that receive some kind of enhancement (in precision, efficiency, simplicity of implementation, etc.) through the use of quantum effects.

1.1.2 Quantum enhancement of the precision

In order to overcome the SQL we can follow two different paths. On the one hand, using squeezed state, we can reduce the uncertainty related to the probe, decreasing directly $\Delta\sigma$. On the other hand, we can increase the precision by correlating the results of the measure using entangled probes. In this section, we will explain these two strategies in more detail.

1.1.2.1 Squeezed states

In quantum mechanics we associate to each physical observable a mathematical self-adjoint linear operator, whose spectrum represents the set of possible outcomes of a measurement of that quantity. The principle of complementarity, formulated by Niels Bohr, tells us that objects have pairs of complementary properties which cannot be observed or measured simultaneously with arbitrary high precision, like position and momentum of an electron, or energy and lifetime of an excited state. This concept is rigorously formalized by the well known uncertainty principle defined by Heisenberg, synthesized by the following equation:

$$\Delta\hat{A}\Delta\hat{B} \geq \frac{1}{2}\left|\langle[\hat{A},\hat{B}]\rangle\right|, \tag{1.1.4}$$

where $\Delta\hat{A}$ and $\Delta\hat{B}$ are the uncertainties associated to two complementary quantities described by the operators $\hat{A}$ and $\hat{B}$, while $[\hat{A},\hat{B}] = \hat{A}\hat{B} - \hat{B}\hat{A}$ is the commutator between $\hat{A}$ and $\hat{B}$. This fundamental property, the impossibility to know

with infinite precision two non commuting quantities, leads to an unavoidable level of uncertainty. However, if we are just interested in the precision associated with one of the two quantities, using squeezed states we can improve the performances. Squeezed state are quantum state in which the uncertainty in the monitored observable is very small, at the cost of a very large uncertainty in the complementary one. Mathematically we have:

$$\left\langle \left\langle \Delta \hat{A} \right\rangle^2 \right\rangle < \frac{1}{2} \left| \langle \hat{C} \rangle \right| \qquad \left\langle \left\langle \Delta \hat{B} \right\rangle^2 \right\rangle > \frac{1}{2} \left| \langle \hat{C} \rangle \right| \qquad (1.1.5)$$

where $\left[\hat{A}, \hat{B} \right] = i\hat{C}$. For example, if we want to measure the refractive index of a material, we can use a squeezed state of light. Indeed this kind of measures are typically performed by interference, so we are using the phase of light as a probe. Being phase and amplitude two correlated variable, squeezing the former we will reduce the uncertainty related to the probe and so $\Delta\sigma$, although we are loosing information on the number of photons (thus increasing the photon-counting noise).

1.1.2.2 Entangled states

Quantum entanglement is a physical phenomenon which occurs when pairs or groups of particles are generated, interact, or share spatial proximity such that the quantum state of each particle cannot be described independently of the state of the other(s). Even when the particles are separated by a large distance, a quantum state must describe the system as a whole. In this mixing of states the central limit theorem does not hold anymore, because the probes are no longer independent. This leads to the possibility to enhance the precision of the estimation of a parameter above the SQL. Indeed in this way we can correlate the result of the measure, maximizing the amount of information that can be extracted. Consequently, it is possible to demonstrate [7] that the SQL bound can be replaced with the so-called Cramer-Rao bound:

$$\Delta\phi \geq \frac{\Delta\sigma}{\sqrt{nF(\phi)}} \qquad (1.1.6)$$

where n is the number of repetitions of the measurement (or, equivalently, the number of the probing particles) while $F(\phi)$ is the Fisher information, that is the maximum amount of information about the parameter ϕ that we can extract from the system, and it is dependent from the measurement setting. The nature

of $F(\phi)$ is crucial in the determination of a lower bound [8]. Indeed:

- in the case of n independent measurements, the Fisher information is a constant and the mean square error scales as:

$$\Delta\phi \geq \frac{\Delta\sigma}{\sqrt{n}} \qquad (1.1.7)$$

  that is the SQL, as we've seen in the previous section.

- if all resources are used in a single-shot experiment, the Fisher information becomes proportional to the resource number n, and the mean squared error becomes:

$$\Delta\phi \geq \frac{\Delta\sigma}{n} \qquad (1.1.8)$$

  This limit is commonly know as the "Heisenberg bound" and it presents a gain of $\sqrt{n}$ over the SQL.

A schematic example of this highly correlated configuration is reported in Figure 1.1b.

1.1.3 Limitations

Even if we've shown that it's possible to go beyond the SQL, this is not an easy task. For example, in the previous section we were neglecting other quantum constraints such as the Margolus-Levitin theorem that impose limits on how accurately we can measure quantities given the amount of physical resources, e.g. energy, at hand to perform the measurement [6]. Another important issue is the fragility of the quantum states we have described in the previous subsection (such as squeezed and entangled states): the Heisenberg bound is valid from an ideally noiseless system; in practice, though, in most cases environmental decoherence (due to technical noise, thermal energy, vibrations and so on) imposes a more severe limitation on precision, making the quantum enhancement negligible. In order to preserve the coherence, various strategies have been developed, such as quantum error correction techniques [2] [9], optimization of the probing time [10], monitoring of the environment [11] and the use of non-Markovian effects [12]. One important consequence of the physical nature of measurement is the so-called 'quantum back action' [13]. The extraction of information from a

---

[2]Quantum error correction is a method to reduce noise in systems. In principle it enables a noisy quantum computer to simulate faithfully an ideal quantum computer, with reasonable overhead cost, if the noise is not too strong or too strongly correlated.
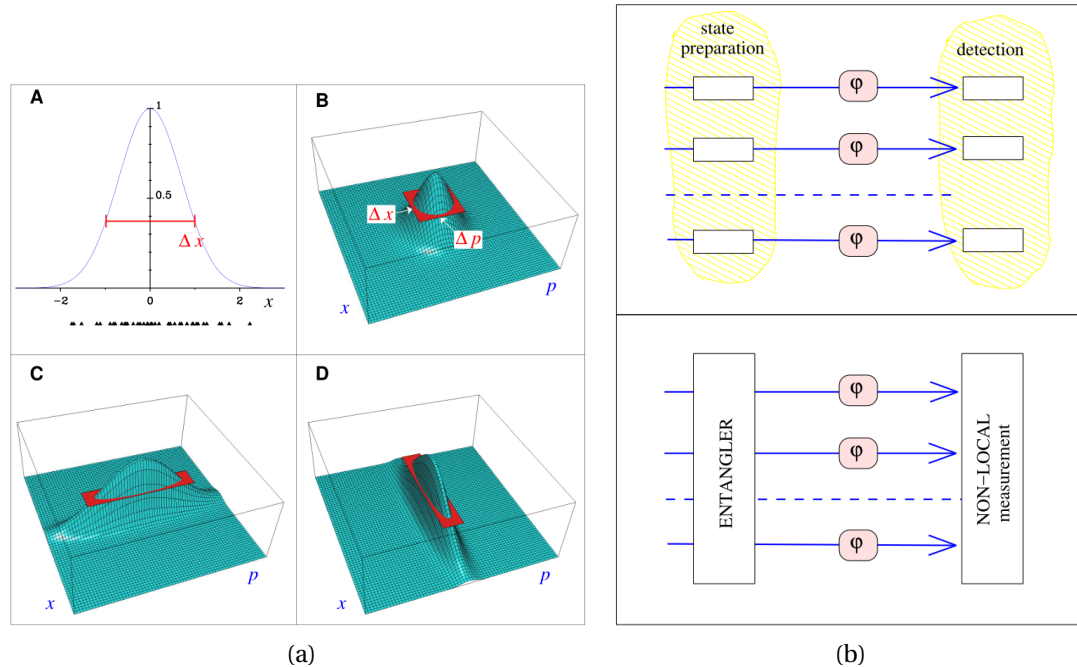
Figure 1.1: *(a)* In quantum mechanics the outcomes x_1, x_2, etc. of the measurements of a physical quantity x are statistical variables, so they are randomly distributed according to a probability determined by the state of the system. A measure of the "sharpness" of a measurement is given by the spread Δx of the outcomes: An example is given in (A), where the outcomes are distributed according to a Gaussian probability with standard deviation Δx. We've seen in Equation 1.1.4 that when simultaneously measuring incompatible observables (such as position x and momentum p) the product of the spreads is lower bounded. In (B) we see a coherent state: it has the same spreads in position and momentum $\Delta x = \Delta p$. In (C) and (D), squeezed states are shown: they have reduced fluctuations in one of the two incompatible observables [i.e. x for (C) and p for (D)] at the expense of increased fluctuations in the other. *(b)* Comparison between classical and quantum measuring strategies. In conventional measurement schemes (upper panel), N independent physical systems are separately prepared and separately detected. The final result comes from a statistical average of the N outcomes. In quantum-enhanced measurement schemes (lower panel), the N physical systems are typically prepared in a highly correlated configuration (i.e. an entangled state), and are measured collectively with a single non-local measurement that encompasses all the systems. Images taken from [6].

system can give rise to a feedback effect in which the system configuration after the measurement is determined by the measurement outcome. The most extreme case, the so-called von Neumann (or projective) measurement, produces a complete determination of the post-measurement state. Thus performing successive measurements, quantum back action can be detrimental, as earlier measurements can negatively influence successive ones. In order to avoid this issue a strategies known as "quantum non-demolition measurements" has been developed [14]. To conclude, we can say that a quantum enhancement of the precision is possible, but most standard measurement techniques do not account for these quantum subtleties and their results are limited by otherwise avoidable sources of errors.

1.2 Super-resolution in optical measurement

In this section, we will explain how the concepts of quantum metrology apply to optical interferometric measurements, giving the possibility to achieve super-resolution in the estimation of the phase (being it the aim of the device presented in this thesis work). In order to do that, we will focus on a simple Mach-Zender interferometer, studying its different behaviour when, as input, we use a classical coherent state or a quantum state of light.

1.2.1 Mach-Zender interferometer

The Mach-Zehnder interferometer (MZI) was proposed by the physicists Mach and Zehnder in the 1891 [15] and its setup is showed in Figure 1.2. A light beam impinges on a semi-transparent mirror (i.e. a beam splitter), which divides it into a reflected and a transmitted part. These two components travel along different paths and then are recombined by a second beam splitter. Information on the phase difference φ between the two optical paths of the interferometer can be extracted by monitoring the two output beams, typically by measuring their intensity (i.e. the photon number).

1.2.2 Classical approach

Suppose that a classical coherent beam with N average photons enters the interferometer through the input A. If there is no phase difference φ, all the photons will exit the apparatus at output D. On the other hand, if $\varphi = \pi$ radians, all
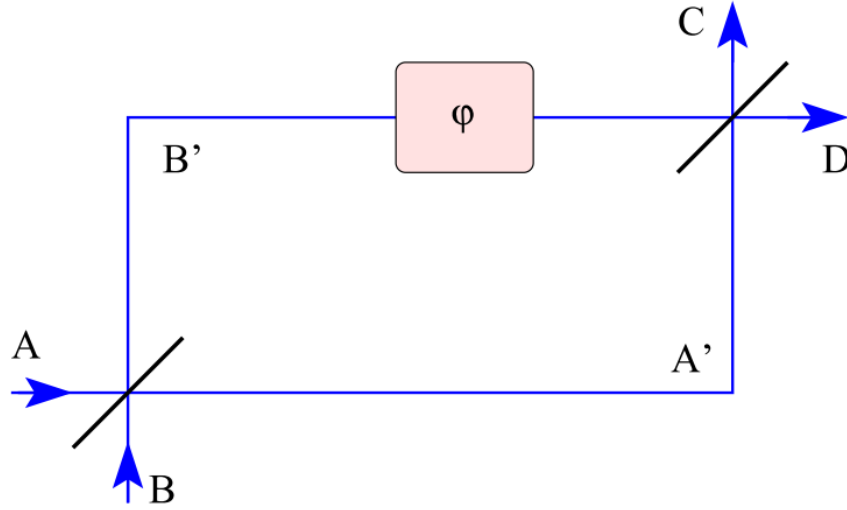
Figure 1.2: Mach-Zehnder interferometer setup. The light field enters the apparatus through the input ports A and B of the first beam splitter and leaves it through the output ports C and D of the second beam splitter. By measuring the intensities (photon number per second) of the output beams one can recover the phase difference φ between the two internal optical paths A' and B'.

the photons will exit at output C. Now, let's suppose to enter from the port A with a classical coherent state of light: we can describe it's electric field as

$$E = E_0 e^{i(\omega t - k\bar{r})} \tag{1.2.1}$$

where ω is the angular frequency and k the wavenumber of he beam. If we assume to have perfectly balanced beam splitters, 50% of the beam will be reflected towards B' while the other 50% will be transmitted toward A'. The reflected beam will also acquire a π shift: this is due to the fact that light passes from a lower refractive index (air) to an higher one (dielectric coating of the mirror), as stated by the Fresnel equations. Thus at the second beam splitter, taking into account the phase difference φ,that can be a geometrical difference in the path or an induced phase difference (i.e. by changing the refractive index of the medium) we will have:

$$E_{A'} = \frac{E_0}{\sqrt{2}} e^{i(\alpha + \pi + \varphi)}$$

$$E_{B'} = \frac{E_0}{\sqrt{2}} e^{i(\alpha)} \tag{1.2.2}$$

in witch we referred to $\omega t - k\bar{r}$ as α to simplify the notation. If we focus on the exit port C, $E_{B'}$ will gain another π shift in its phase, thus the interference of the

two fields will result, in intensity, as

$$
\begin{aligned}
I_C \;\; &\propto\;\; \frac{1}{2}\left(E_{A'}+E_{B'}\right)\left(E_{A'}^*+E_{B'}^*\right) && (1.2.3) \\
&=\;\; \frac{1}{2}\left(E_{A'}E_{A'}^*+E_{B'}E_{A'}^*+E_{A'}E_{B'}^*+E_{B'}E_{B'}^*\right) \\
&=\;\; \frac{1}{2}\left(|E_{A'}|^2+|E_{B'}|^2\right)+\frac{|E_0|^2}{2}\left(e^{i(\varphi+\pi)}+e^{-i(\varphi+\pi)}\right) \\
&=\;\; \frac{|E_0|^2}{2}\left(1+\cos\left(\varphi+\pi\right)\right) \\
&=\;\; \frac{|E_0|^2}{2}\left(1-\cos\left(\varphi\right)\right)
\end{aligned}
$$

The same reasoning is valid for the port D, at witch we will have

$$
I_C \propto \frac{|E_0|^2}{2}\left(1+\cos\left(\varphi\right)\right) \tag{1.2.4}
$$

By measuring the intensity at the two output ports one can estimate the value of φ with a statistical error proportional to $\frac{1}{\sqrt{N}}$: this is a consequence of the quantized nature of electromagnetic field of the poissonian statistics of classical light, witch, in some way, prevents any cooperative behaviour among the photons. The statistical demonstration, out of the scope of this thesis, can be found in [13].

1.2.3   Quantum approach

In order to describe the behaviour in a total quantum regime, we need to take a step back and focus on the description of the beam splitter cause at the level of a single or few photons, the classical approach to beam splitting produces erroneous and quite misleading results. In the classical picture of the beam splitter there is an unused "port" which, being empty of an input field, has no effect on the output beams. However, in the quantum-mechanical picture, the "unused" port still contains a quantized field mode albeit in the vacuum state [16]. To provide a correct quantum description we need to take it into account, as in Figure 1.3. We can now express the beam-splitter transformations for the field operators as

$$
\begin{pmatrix} \hat{a}_2 \\ \hat{a}_3 \end{pmatrix} = \begin{pmatrix} t' & r \\ r' & t \end{pmatrix}\begin{pmatrix} \hat{a}_0 \\ \hat{a}_1 \end{pmatrix} \tag{1.2.5}
$$

in witch r, r', t and t' need to be respect the energy conservation principle. This constrain lead to a multiple possible description of these values. We will proceed
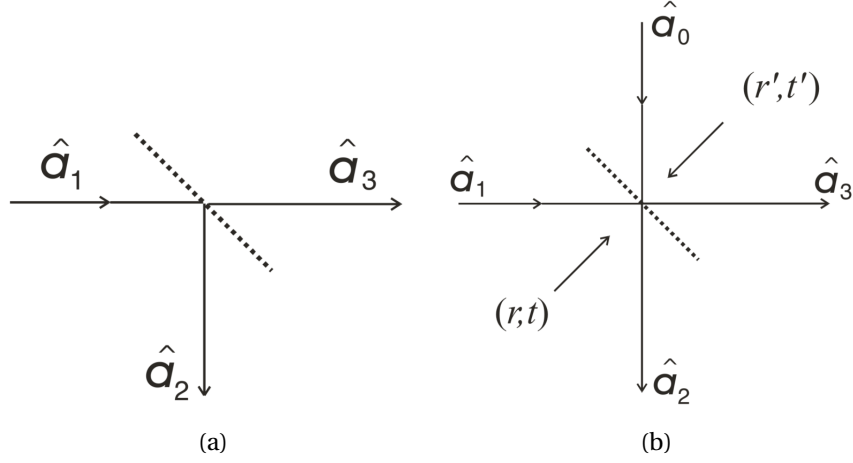
Figure 1.3: (a) Classical depiction of a beam splitter. (b) Quantum-mechanical depiction of a beam splitter.

using the "symmetric configuration", in witch $r = ir'$ and $t = t'$ so that we do not have to distinguish the side of the beam splitter. For a 50/50 BS, Equation 1.3 become

$$
\begin{pmatrix} \hat{a}_2 \\ \hat{a}_3 \end{pmatrix} = \frac{1}{\sqrt{2}} \begin{pmatrix} 1 & 1 \\ i & 1 \end{pmatrix} \begin{pmatrix} \hat{a}_0 \\ \hat{a}_1 \end{pmatrix}
\tag{1.2.6}
$$

1.2.3.1 Single photon interference

Consider the single photon input state $|0\rangle |1\rangle$, so a single photon entering from B. For the beam splitter described by 1.2.6 we obtain

$$
|0\rangle |1\rangle \overset{\text{BS}_1}{\to} \frac{1}{\sqrt{2}} \left(i |1\rangle |0\rangle + |0\rangle |1\rangle \right)
\tag{1.2.7}
$$

This is an entangled state, before the measure we cannot know in witch path the photon has taken [17]. Then we need to take into account the phase shifter on the upper arm, so

$$
\frac{1}{\sqrt{2}} \left(i |1\rangle |0\rangle + |0\rangle |1\rangle \right) \overset{\varphi}{\to} \frac{1}{\sqrt{2}} \left(i |1\rangle |0\rangle + e^{i\varphi} |0\rangle |1\rangle \right)
\tag{1.2.8}
$$

Finally, at the second beam splitter we have

$$
\frac{1}{\sqrt{2}} \left(i |1\rangle |0\rangle + e^{i\varphi} |0\rangle |1\rangle \right) \overset{\text{BS}_2}{\to} \frac{1}{2} \left[i \left(e^{i\varphi} + 1 \right) |1\rangle |0\rangle + \left(e^{i\varphi} - 1 \right) |0\rangle |1\rangle \right]
\tag{1.2.9}
$$

13

so that the probability to have a count on the detector C is $P_{01} = \frac{1}{2}\left(1 - \cos\varphi\right)$, while for the detector D we obtain $P_{10} = \frac{1}{2}\left(1 + \cos\varphi\right)$. These are the same results we obtained in the classical approach, so we can conclude that we have no improve with just one photon.

1.2.3.2 Two-photon interference

Let's consider now the case in witch we enter the beam splitter with two photon, one per port. After the first BS we have

$$|1\rangle\,|1\rangle \overset{\mathrm{BS_1}}{\to} \frac{i}{\sqrt{2}}\left(|2\rangle\,|0\rangle + |0\rangle\,|2\rangle\right) \tag{1.2.10}$$

There will always be two photon in the same arm, even if we do not know in which. The absence of the output $|1\rangle\,|1\rangle$ it's a consequence of the quantum interference and has no classical counterpart. This behaviour, know as Hong–Ou–Mandel effect [18], is possible only if the photons are perfectly indistinguishable. Proceeding with the calculations, we take into account the phase shift

$$\frac{i}{\sqrt{2}}\left(|2\rangle\,|0\rangle + |0\rangle\,|2\rangle\right) \overset{\varphi}{\to} \frac{i}{\sqrt{2}}\left(|2\rangle\,|0\rangle + e^{i2\varphi}\,|0\rangle\,|2\rangle\right) \tag{1.2.11}$$

and the second BS:

$$\begin{aligned}
\psi_{\mathrm{final}} \;=\; & \frac{1}{2\sqrt{2}}\left(1 - e^{i2\varphi}\right)\left(|2\rangle\,|0\rangle - |0\rangle\,|2\rangle\right) \\
& + \frac{i}{2}\left(1 + e^{i2\varphi}\right)|1\rangle\,|1\rangle
\end{aligned}$$

In order to get the information on the phase, we need to measure the parity (evenness or oddness of the photon numbers) of signal on the two detectors. In this way, as showed in [19], it is possible to obtain a probability that is proportional to $\left(1 + \cos\left(2\varphi\right)\right)$. This faster variation is linked to a better resolution of the experiment: indeed the standard deviation in this case is $1/2$ instead of the classical $1/\sqrt{2}$. We can conclude that, using an entangled state as the one in Equation 1.2.10, we can reach the Heisenberg limit of the measure.

1.2.3.3 Multi-photon interference

The state in Equation 1.2.10 is a particular NOON state, a general state made by the superposition of N particles in a mode A and with zero particles in mode

B, and vice versa. The general formula is

$$\psi_{\text{NOON}} = \frac{|N\rangle\,|0\rangle + |0\rangle\,|N\rangle}{\sqrt{2}} \qquad (1.2.12)$$

Using a state like this, is possible to enhance the resolution on the phase reaching N-faster oscillation [20], obtaining, in theory, the Heisenberg limit in every measure. The real problem is the creation of these NOON states: if the generation of the $N = 2$ case is easy, the higher order is not. There have been several theoretical proposals for creating photonic NOON states: Kok, Lee, and Dowling proposed the first general method based on post-selection via photodetection [21] while Pryde and White [22] introduced a simplified method using intensity-symmetric multiport beam splitters, single photon inputs, and either heralded or conditional measurement. A different approach, involving the interference of non-classical light created by spontaneous parametric down-conversion and a classical laser beam on a 50/50 beam splitter, was used by Afek et al. to experimentally demonstrate the production of NOON states up to $N = 5$ [23].

1.3   Applications

The quantum-enhanced parameter estimation presented above has found applications in the most diverse fields. In this section we give an overview of some of them, making a distinction between an enhancement based on squeezed state and entangled systems.

1.3.1   Squeezed state enhancement

1.3.1.1   Gravitational wave observation

In 1916, the year after the final formulation of the field equations of general relativity, Albert Einstein predicted the existence of gravitational waves. He found that the linearized weak-field equations had wave solutions: transverse waves of spatial strain that travel at the speed of light, generated by time variations of the mass quadrupole moment of the source [24]. Experiments to detect gravitational waves began with Weber and his resonant mass detectors in the 1960s [25], while interferometric detectors were first suggested in the early 1960s [26]. Recently, on September 14 2015 at 09:50:45 UTC[3], B. P. Abbott et al. were able to validate the

---

[3]It took 1.3 billion years for the waves to arrive at the LIGO detector in the USA.

observation of gravitational waves from a binary black hole merger [27]. The observation, that lead to the Nobel prize in Physics in 2015 [28] was made possible by the simultaneous acquisition of the signal GW150914 by the the LIGO Hanford (WA), and the LIGO Livingston (LA) facilities: these are basically Michelson-like interferometer, whose resolution allow them to detect a change in the 4 km mirror spacing of less than a ten-thousandth the charge diameter of a proton, equivalent to measuring the distance from Earth to Proxima Centauri ($4.0208 \cdot 10^{13}$ km) with an accuracy smaller than the width of a human hair. This incredible precision is mandatory in the observation of a signal weak as the one predicted by Einstein, cause a fundamental limit to the sensitivity of a Michelson interferometer with quasi-free mirrors comes from the quantum nature of light, which reveals itself through two fundamental mechanisms: photon counting noise (shot noise), arising from statistical fluctuations in the arrival time of photons at the interferometer output, and radiation pressure noise, which is the recoil of the mirrors due to the radiation pressure arising from quantum fluctuations in the photon flux. Caves [29] showed that replacing coherent vacuum fluctuations entering the anti-symmetric port of the interferometer with correctly phased squeezed vacuum states decreases the "in-phase" quadrature uncertainty of the electromagnetic field, and thus the shot noise, below the quantum limit. Following this result, the experiment performed by Aasi et al. [30] demonstrated a enhancement of the precision with respect to a classical measurement, as showed in Figure 1.4a.

1.3.2 Entangled system enhancement

1.3.2.1 Quantum lithography and two-photon microscopy

When we try to resolve objects smaller than the wavelength of the employed light, the wave nature of radiation becomes important: the light tends to scatter around the object, limiting the achievable resolution. This defines the Rayleigh diffraction bound, which restricts many optical techniques: it is not always practical to reduce the wavelength (technical impossibility or power limitation as we've seen in biology). Quantum effects could be used in order to decrease the effective wavelength of the light while keeping the wavelength of the radiation field constant. The idea is to employ physical devices that are sensitive to the de Broglie wavelength: in quantum mechanics we can associate to every object a

wavelength $\lambda = \frac{2\pi\hbar}{p}$ where p is the object's momentum [4]. Obviously the wavelength of a single photon is the wavelength of its radiation field, but what happens if we are able to employ a "biphoton" (i.e. a single entity constituted by two photons)? We find that its wavelength is $\frac{2\pi c}{2E} = \frac{\lambda}{2}$: half the wavelength of a single photon, thus half the wavelength of its radiation field. Of course, using "triphotons", "quadriphotons", etc. would result in further decreases of wavelengths: we can go beyond the classical Rayleigh diffraction bound. The most important applications are quantum lithography [31], where smaller wavelengths help to etch smaller integrated circuit elements on a two-photon sensitive substrate, and two-photon microscopy [32], where they produce less damage to the speciments. In this context, entanglement is a useful resource in creating the required biphotons and in enhancing the cross-section of two-photon absorption.

1.3.2.2 Quantum biology

Since biological samples are often highly photosensitive and optical damage is a limiting factor in many biophysical experiments, we cannot improve the precision by simply increasing the optical power. The quantum enhancement is particularly relevant in a situation like this, where we're limited by power constrains [33]: typical damages are due to heating, strongly correlated with the presence of water, and to the photo-chemical effect, correlated with the increase of photon energy. Entangled photon pairs have now been applied in absorption imaging [34], tissue imaging [35], or to measure the protein concentration in a solution, as explained in the work of Crespi et al. [36] (Figure 1.4b). Squeezed states of light have been used, for example, to measure dynamic changes [37]. These experiments have demonstrated the prospects of quantum correlations for new capabilities and unrivalled precision in practical biological measurements.

---

[4]For radiation p is the energy E divided by the speed of light c.

(a)   (b)
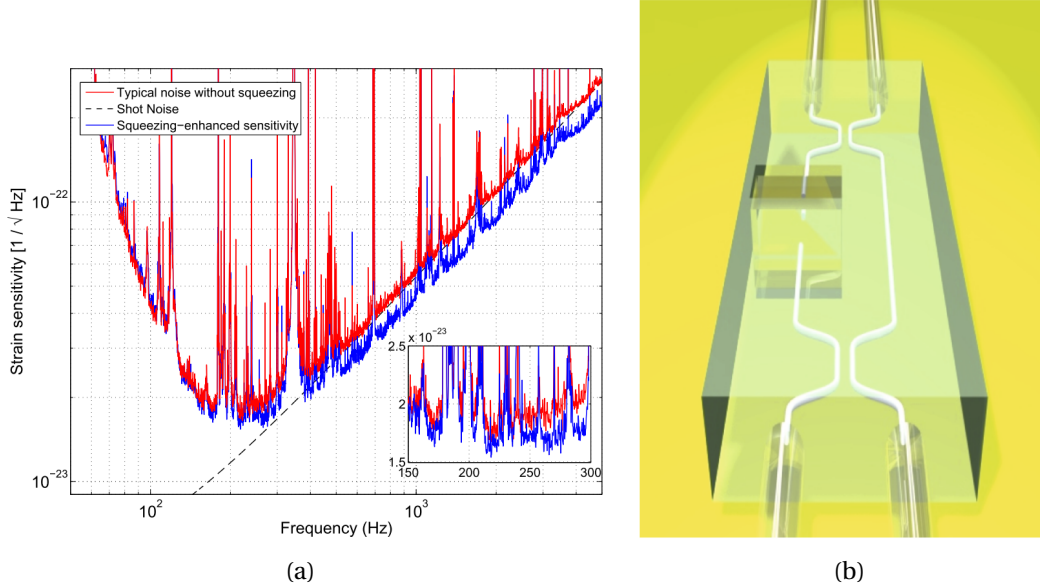
Figure 1.4: *(a)* Strain sensitivity of the H1 detector measured with and without squeezing injection. The improvement is up to 2.15 dB in the shot noise limited frequency band. Several effects cause the sharp lines visible in the spectra: mechanical resonances in the mirror suspensions, resonances of the internal mirror modes, power line harmonics, etc. As the broadband floor of the sensitivity is most relevant for gravitational wave detection, these lines are typically not too harmful. The inset magnifies the frequency region between 150 and 300 Hz, showing that the squeezing enhancement persists down to 150 Hz. From [30]. *(b)* Crespi et al. fabricated, by FLM techniques, a Mach-Zehnder interferometer coupled with a microfuidic channel passing through one of its arm. In this channel flows a light-sensitive solution and a phase shift, induced by the concentration-dependent refractive index, is acquired by the photons which travel inside the interferometer. Thus, depending on the concentration of a certain protein inside the solution, a different pattern of the interference fringes is detected. In this work it is proofed, employing entangled photons, the overcoming of SQL and the achievement of super-resolution. In the image, a schematic of the Mach-Zehnder interferometer (MZI) interfaced to the microchannel is presented. The fluidic channel has rectangular cross-section 500 μm × 55 μm and extends from the top to the bottom surface of the glass substrate (∼1 mm thickness). The MZI consists of two 50:50 directional couplers and has two arms of equal geometrical length; one waveguide crosses perpendicular to the microchannel, while the other passes externally. Image taken from [36].

Femtosecond Laser Micromachining

2.1 Introduction

Mainly depending on the kind of substrate that one wants to use, together with the desired refractive index contrast and the specific applications, different techniques have been developed for fabricating waveguiding circuits. The most common technique for waveguides fabrication consists in creating a bidimensional layer of high refractive index material (a planar waveguide) on top of a substrate wafer and then define the circuit lateral walls, by adopting standard lithographic techniques (like UV or electron beam lithography). This technique allows for a very well engineered refractive index contrast together with a good cross section geometry, and the resulting waveguides can exhibit very low propagation loss ($\approx 1 \div 5\,\mathrm{dB/m}$), with bending radii down to few millimeters or lower. However, due to the planar nature of any lithographic process, these techniques suffer from the limitation that they can only be used for the fabrication of bidimensional circuits. Moreover, the need of lithographic masks for the definition of the circuit geometry makes the prototyping of new devices very slow and expensive. A somehow complementary approach for fabricating optical circuits is that of direct writing techniques, where the circuit geometry is defined by scanning the substrate under a laser beam or a beam of accelerated particles. Direct optical circuit fabrication by means of ultrafast laser irradiation was first demonstrated in 1996 by Davis et al. [38], who employed the non-linear absorption of a

focused infrared femtosecond laser beam to locally increase the refractive index of a fused silica substrate and, by tailoring the fabrication parameters (e.g. pulse energy and repetitions rate), were able to obtain a high quality waveguide. The advantages of femtosecond laser waveguide micromachining (FLM) are numerous:

- **Fast prototyping**: since FLM does not require the use of dedicated photo-lithographic masks, it is a direct and single-step fabrication technique that allows to create optical waveguides or more complicated photonic devices (splitters, interferometers, etc.) with a relatively simple setup, not requiring the use of special facilities, such as clean rooms. This brings to a consistent cost reduction and process speed-up, very useful for the prototyping of new circuit designs on small scale production.

- **High flexibility**: with a suitable choice of the irradiation parameters (wavelength, pulse energy, repetition rate, focusing conditions, translation speed, etc.) one can inscribe waveguides in almost any type of glasses. In addition, the FLM (actually the technique has been extended to crystalline dielectric materials, such as YAG and lithium niobate [39], and to polymers [40].

- **Three-dimensional technique**: because of the nonlinear nature of the interaction, absorption is confined to the focal volume inside the bulk material. This implies that the focusing depth can be changed without altering, at least in first approximation [41], the properties of the induced modification. By scanning the sample relative to the laser focus with computer-controlled motion stages, a region of increased refractive index could be formed along an arbitrary three-dimensional path.This permits to fabricate the waveguides with a 3D geometry and to develop circuit designs with configurations otherwise impossible to get.

2.1.1 Laser-material interaction

Unlike the laser processing of photosensitive glasses, which relies on single photon absorption of high energy ultraviolet (UV) light, the FLM technique relies on the multiple absorption of photons with energies smaller than the bandgap of the material. The advantage of this method is the fact that the energy deposition is localized at the focus since the material is otherwise transparent at the writing wavelength. This also means that virtually any transparent dielectric can be
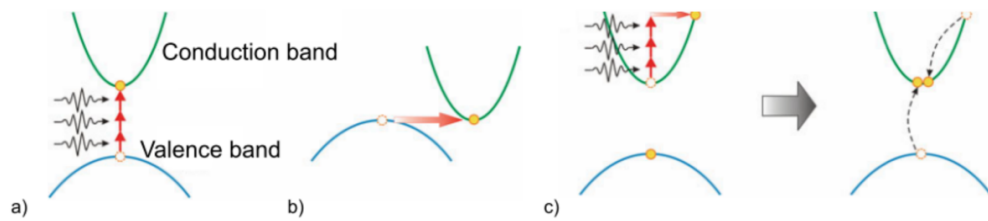
Figure 2.1: Non-linear light absorption processes: (a) multiphoton absorption; (b) tunneling; (c) avalanche ionization. Image taken from [43].

processed using the FLM technique, including glasses, ceramics and even crystalline materials. However the morphology of the induced material modification can vary significantly depending on the material and exposure conditions [42]. In order to achieve such multiphoton absorption, high peak intensities per pulse ($\approx 10\,{}^{TW}/cm^2$) are required, and they can be produced by focused femtosecond laser pulses from today's commercial laser systems. The interaction process can be divided into two main steps: the initial generation of a free electron plasma followed by energy relaxation and modification of the material.

2.1.1.1 Free electron plasma formation

Linear absorption of light at frequency ω takes place in a certain material when the energy carried by a photon is higher than the material band gap: $\hbar\omega \geq E_g$. As we said, in FLM we want to avoid this linear absorption (the material must be transparent at the fabrication wavelength) while enhancing non linear absorption; the latter absorption is mainly driven by three kind of process (as shown in Figure 2.1):

- **Multiphoton absorption**: it is the dominant mechanism at low laser intensities and high frequencies. A valence electron is promoted to the conduction band after the simultaneous absorption of m photons, in such a way that the overall absorbed energy is higher than the bandgap ($mh\nu \geq E_g$, where $h\nu$ is the energy of a single photon).

- **Tunneling ionization**: for increasing field intensities, the band structure is deformed and the potential barrier between the valence and conduction bands reduces. Direct band to band transitions may then proceed by quantum tunneling of the electron from the valence to conduction band. As shown by Keldysh [44], it is worth mentioning that multiphoton and tunneling photoionization can be described in the same theoretical frame-

work, and the transition between the processes is parameterized by the Keldysh parameter.

- **Avalanche ionization and generation of plasma**: the seed of free electrons promoted in the conduction band by tunneling or multiphoton absorption, together with thermally excited electrons, can now linearly absorb other photons from the same laser pulse, increasing their kinetic energy. This can lead, by impact ionization, to the promotion of other electrons from the valence to the conduction band: this process is called avalanche ionization.

2.1.1.2 Plasma relaxation and modification of the material

The number of the promoted electrons grows as a hot plasma, until the density of plasma frequency, $\omega_p = \sqrt{n_e e^2 / m_e \epsilon_0}$, is reached. At this point the energy transfer from the laser field to the electronic plasma becomes very efficient and the light gets almost entirely absorbed by it [45]. After the generation of the hot electrons plasma, the energy is released to the lattice. The physical effects leading to the permanent modification of the exposed material are not completely understood yet. However, three different regimes can be distinguished according to the deposited energy, depending on the fabrication parameters (e.g. pulse energy and duration, repetition rate, scan speed) [46]:

- **Smooth refractive index change**: at low pulse energies just above the modification threshold, a smooth and permanent refractive index change can be obtained [47]. This regime is ideal for the fabrication of waveguides, since the material maintains its transparency. This modifications can be explained by the coexistence of several mechanisms, such as rapid quenching of the melted glass in the focal volume [48], color centers formation [49], ion migration effects [50] and pulse-induced shock waves [51]

- **Birefringent refractive index change**: for higher pulse energies, birefringent refractive index changes have been observed in the bulk of fused silica glass [52]. The most accredited explanation is the presence of periodic nanostructures that were caused by interference of the laser field and the induced electron plasma wave [53], together with the possibility of an inhomogeneous dielectric breakdown that causes the formation of nanoplasma with the subsequent growth of nanoplanes.

- **Void formation**: by further increasing the pulse energy, a shock wave is generated after the energy transfer from plasma to ions, leaving a hollow core surrounded by a cladding of higher refractive index. This kind of modification can be employed for 3D optical memory applications (this is the case of microvoids representing voxels (volume pixels) [54]) or the fabrication of photonic bandgap materials [55], but are not suitable for optical waveguides.

At this point it is possible to explain why a sub-picosecond pulse duration is an essential ingredient in FLM. On the one hand, processes of multiphoton and tunneling ionization require very high pulse peak intensities to take place and trigger the avalanche photoionization in a deterministic fashion, while for longer pulses (i.e with lower peak intensity) the plasma creation relies on seeds electrons provided only by thermally excited impurities or defects states. These are usually few and randomly distributed in the material, reflecting in a less uniform machining. On the other hand, the plasma relaxation mechanisms take place in a temporal scale of the order of tens of picoseconds. Thus, using femtosecond pulses is it possible to decouple the processes of plasma excitation and the lattice heating. This, together with the fact the small focus that trigger the whole process, leads to a substrate modification that is strongly localized in a micrometric volume [56].

2.2   Fabrication parameters

Besides the pulses duration and energy, whose effects have already been discussed with respect to the physics behind the laser-substrate interaction, the irradiation parameters that mostly influence the waveguides fabrication with FLM are the focusing numerical aperture (NA) and depth, the beam repetition rate, and the fabrication geometry and speed.

2.2.1   Focusing condition

The incident laser pulses are focused inside the substrate by means of some focusing optics, in order to reach the needed high peak intensity. This is typically done through a microscope objective, compensated both for spherical and chromatic aberrations, in order to avoid as much as possible beam distortions at the focus. The most important objective parameter is its NA, since it determines the size of the focal volume. In the linear propagation approximation of a focused

Gaussian beam inside the glass, the waist radius w_0 and the Rayleigh range z_0 can be calculated as:

$$w_0 = \frac{M^2\lambda}{\mathrm{NA}\pi} \qquad z_0 = \frac{nM^2\lambda}{\mathrm{NA}^2\pi} \qquad (2.2.1)$$

where M^2 is the beam quality factor, λ is the laser free space wavelength and n is the glass refractive index. These expressions underline that the choice of higher NA objectives allow to obtain tighter and less elongated focuses. In fact, the ratio between the waist radius and the Rayleigh range is equal to NA/n, so with a higher NA we obtain a more spherical focal volume. The high dependence of the fabrication on the focusing depth as a consequence of using a high numerical aperture objective can be solved by using oil-immersion objectives, since the oil layer reduces the mismatch in refractive index between air and substrate. Nevertheless, this kind of objectives has low working distances, thus reducing the versatility of the fabrication. An alternative solution is using dry objectives with collars, that enable the compensation of spherical aberrations at different depths, but with limited fine length resolution. An analysis of the non-linear refractive index of the material under processing should always be performed, to compensate effects such as self-focusing and light filamentation .

2.2.2 Fabrication geometry

There are two possible waveguide fabrication geometries for FLM, namely the "longitudinal" and the "transverse" one [57], as shown in Figure 2.2.

2.2.2.1 Longitudinal geometry

The substrate is translated in the direction parallel to the incident laser beam, leading to waveguides that exhibit cylindrical symmetry and a round cross section. However, this configuration is not practical in most of the cases, because the processing length is limited by the working distance of the objectives, that, even for a moderate NA, is hardly longer than few millimeters.

2.2.2.2 Transverse geometry

The sample is translated orthogonally to the laser propagation direction, giving the possibility to write much longer waveguides, limited only by the travel range of the sample movement stages. In this case the waveguide cross section is
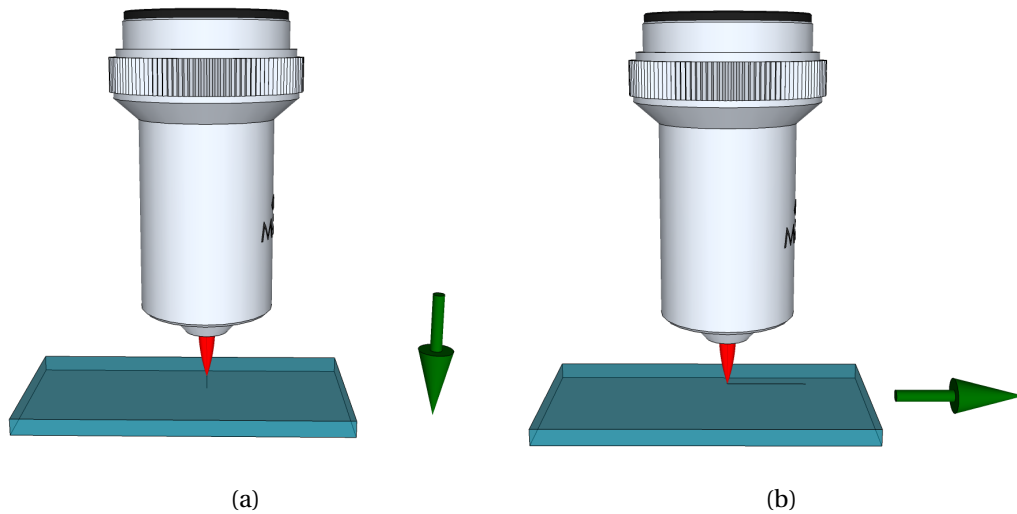
Figure 2.2: Waveguides fabrication geometries: (a) longitudinal and (b) transverse. The green arrows represent the sample translation direction.

no longer circular but elliptical, and strongly influenced by the focal spot shape: this asymmetry leads to an intrinsic waveguide birefringence that may limit certain applications or be a key feature in others, for example having the need to have elliptical guided modes. In order to reduce these effects, beam shaping techniques [58] or multiscan writing approaches [59] can be employed for fabricating waveguide with a more symmetric cross section.

2.2.3 Repetition rate

Laser systems that work at low repetition rate regime (less than 100 kHz) generally deliver highly energetic pulses, that allow more flexibility in the choice of the focusing optics; however, in this regime, the time interval between two consecutive pulses is long enough to permit a complete thermal relaxation of the substrate before the next pulse arrives. This is the so-called single pulse modification regime [61]. It leads to less uniform waveguides (highly asymmetric cross section in transverse geometry) and accumulation of birefringent stress, in addition to a low fabrication speed. On the contrary, when a high repetition rate is used (up to several tens of MHz), the heat generated after a pulse energy deposition does not have time to diffuse away and we can observe a high heat accumulation at the focal spot, with a consequent big temperature increase. At these temperature, the substrate undergoes to a partial melting and a consequent re-
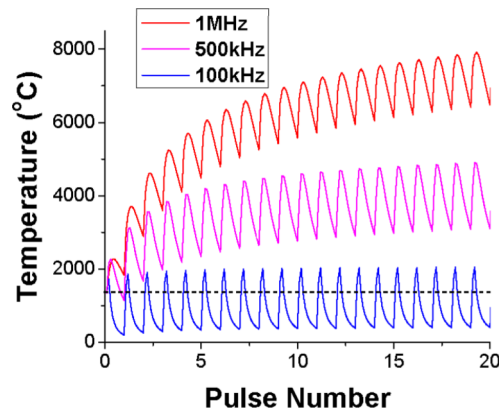
Figure 2.3: Effect of the repetition rate on the heat accumulation. Finite-difference model of the glass temperature at different repetition rates. Image taken from [60].

solidification. The waveguides fabricated in this regime exhibit a more uniform structure and a rounder cross section, with benefits both on the propagation loss and the coupling loss to fibers; working with high repetition rates allows also to increase the fabrication speed, up to 50 ⟷ 100 mm/s. This regime is ideal for the fabrication of optical waveguides in *boro-* and *allumino*-silicate glasses, as demonstrated by Eaton et al. [62].

2.2.4 Others

There are many other parameters that can be tuned to find the optimum waveguide processing window for a given material, such as the sample translation speed that affects the energy deposition rate per unit volume (so to fine tuning of the refractive index change) or the wavelength of the laser employed, that influences the fabrication process determining the order of the multiphoton absorption. Also light polarization can have a role in FLM as well [52].

2.3 Thermal annealing

In order to reduce the internal stress accumulated during fabrication, thermal treatments are traditionally used in glass manufacturing [63]. Indeed, the quick cool down of the melted silica, necessary to avoid crystallization, creates a gradient of cooling rates between the surface and the bulk. This lead to a different volumetric shrink, thus to an accumulation of strong mechanical stress. The resulting glass would then be very brittle at room temperature. To avoid
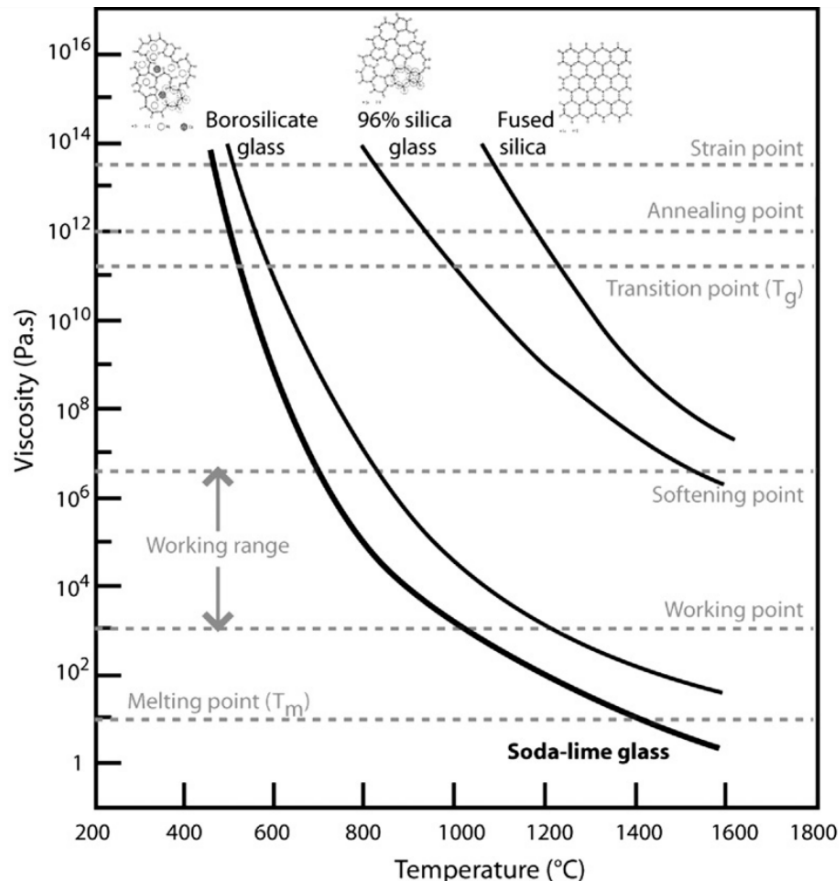
Figure 2.4: Viscosity dependence on temperature for different glasses. The principal characteristic temperatures are highlighted. Image taken from [65].

this drawback, the glass must be heated again below the melting point, and then slowly cooled down. To understand why, it is useful to introduce the characteristic temperatures of glass, defined on it's viscosity [64]. These relations can be summarized by introducing some characteristic temperatures of glass:

- Strain point: temperature corresponding to a viscosity of $10^{14.5}$ Poise. The glass is still solid and the internal stresses are released in few hours. Below this point it is not possible to relieve stress, but the glass can be quickly cooled down without introducing additional stresses.

- Annealing point: temperature corresponding to a viscosity of $10^{13.4}$ Poise. At this point, stresses are released in few minutes by viscous relaxation

- Softening point: temperature corresponding to a viscosity of $10^{7.65}$ Poise. The glass is soft enough to deform under its own weight at a rate of 1 mm/min.

- Working point: temperature corresponding to a viscosity of 10^4 Poise. At

this viscosity, glass is sufficiently soft to be shaped by blowing or pressure.

- Melting point: distinguish a soft glass from a liquid on, since a proper melting point cannot be defined for an amorphous structure.

The annealing process consist in heating the glass, typically near the annealing point, to relax its internal stress. For the first time in 2013, Arriola et al. [66] applied this process on FLM waveguides, studying the effect of annealing on waveguides properties, particularly concerning refractive index profile and bending losses. Indeed, using low pulse repetition rates (kHz) the repetitive modification of the material creates Gaussian-like refractive index profile, ideal for guiding light as its behavior is similar to a step-index profile, but the drawback is that for complex devices long fabrication times are required (1-100 hours) due to the low sample translation speeds (typically tens of microns per second) involved. In contrast, by using high pulse repetition rates (MHz) an accumulation of heat occurs because the inter-pulse spacing is shorter than the thermal diffusion time of the material, resulting in local melting, strong heat diffusion followed by rapid quenching of the material due to the high translation speeds (typically millimeters per second). Under these conditions, fabrication times are greatly reduced buts complex refractive index profiles are created in multicomponent silicate glasses. This lead to large losses for tightly bent waveguides compared to a step-index waveguide [67]. To face this problem, they propose a two steps fabrication to get single mode waveguides in boro-aluminosilicate glass (EAGLE 2000 by Corning) with very low bending losses at 1550 nm:

1. A multimode waveguide is written by employing a higher energy per pulse and a lower translational speed than the usual ones (90 nJ and 500 mm/min instead of 40 nJ and 1000÷1500 mm/min). This causes a high energy deposition, with a relevant modification of the substrate and the formation of a cladding between the core and the unmodified material (Figure 2.5a).

2. The fabricated chip undergoes an annealing procedure, consisting in a heating ramp until 750 °C (with a slope of 100 °C/h until 600 °C, then 75 °C/h), followed by a slow cooling, with a rate of -6 °C/h until room temperature is reached. Such temperature is set in order to be above the annealing point of borosilicate glass (722 °C).

This process brings to stress relaxation in the glass, with the removal of the outer modification ring (Figure 2.5b) of the waveguide and single mode operation. More-
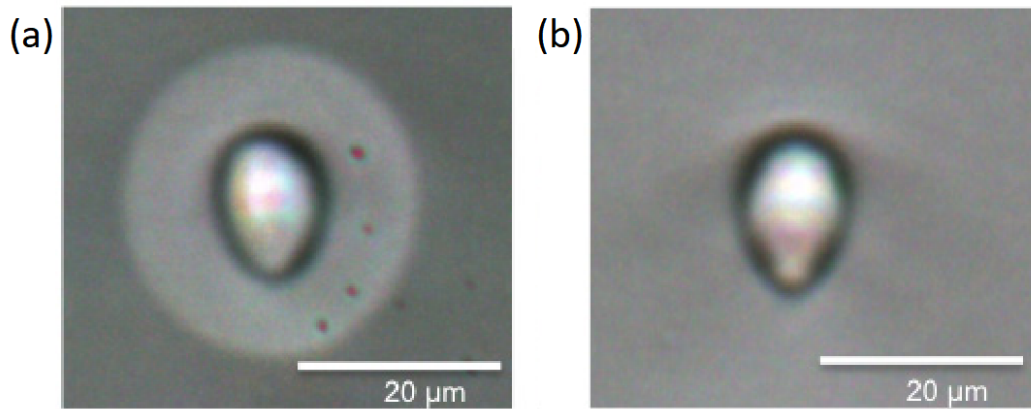
Figure 2.5: Example of waveguide section before (a) and after (b) annealing. It is possible to notice that the outer modification ring is removed, causing a reduction of the mode diameter. Image taken from [66].

over, the refractive index profile is now shown to be Gaussian-like, with a reduction of the mode diameter. Finally, the fabricated waveguides show lower bending losses: e.g., a radius of 20 mm exhibits a 20% of losses, while traditionally it would barely guide light. This thermal process has been recently adoperated by Corielli et al. to demonstrate symmetric polarization insensitive directional couplers fabricated by femtosecond laser waveguide writing [68].

2.4 FLM photonic quantum circuits

Since the first demonstration of waveguide writing [38], many of active and passive photonic devices have been successfully demonstrated on a vast range of substrates, from fiber Bragg gratings [69] to waveguide amplifiers and lasers [70]. Due to the huge diversity of such functional devices that benchmark the versatility of FLM and the creativity of the researchers working in this field, we will focus here on the most relevant ones, employed also in the integrated circuits developed in this thesis.

2.4.1 Directional couplers

In most of applications, optical power splitting is achieved by means of a directional coupler (DC), that is a beam splitter (BS) in its integrated circuit version. Thanks to the low losses and the possibility to tune an arbitrary splitting ratio, DC are widely used in many integrated optics applications. However, its functioning is strongly wavelength and polarization dependent and a careful engineering is
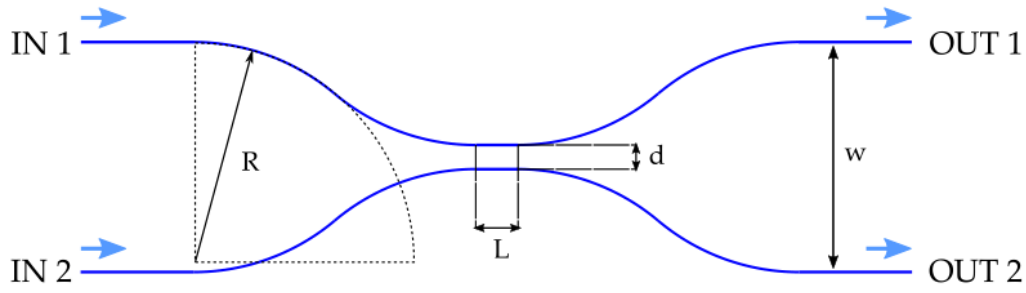
Figure 2.6: Schematic layout of a directional coupler. R is the radius of curvature of the bent waveguide tracts, w is the distance between input (output) ports, d and L are the interaction distance and length of the region where evanescent coupling takes place. As see will show, changing these parameters we can tune the splitting ratio of the coupler.

needed in order to have broadband and polarization insensitive devices. In this device two waveguides get close and, due to evanescent coupling, a light power exchange takes place. This phenomenon can be modeled in terms of coupled mode equations, as fully shown in [43].Taking a look at the solutions reported there, under the hypothesis of symmetrical and identical waveguides we obtain a modulated power exchange P_{ex} between the waveguides which can be mathematically written as

$$P_{exc} = \sin^2(k \cdot L) \tag{2.4.1}$$

where L is the length of the coupling region, whereas κ is the coupling coefficient. Thus, from the tuning of these parameters, it is possible to set the amount of exchanged power and so, the reflectivity R and transmissivity T. Coupling light in one of the two input, for example IN_1, we can define these quantities, for a loss-less DC, as:

$$R = \frac{P_{OUT_1}}{P_{IN_1}} \qquad T = \frac{P_{OUT_1}}{P_{IN_2}} \tag{2.4.2}$$

In order words, the reflectivity is the amount of light power which remains in the first waveguide after the coupling (bar state), while the transmissivity is the power that crosses to the second (cross state). A more complete reasoning on the physical functioning of the DCs will be given in Chapter 5. It's easy to see that even a slight difference or imperfection in the writing of these waveguides would lead to visible consequences in the performances of the device. For this reason, directional coupler fabrication is a benchmark for the success or not in the employment of FLM technique. The first validation of a laser-written directional
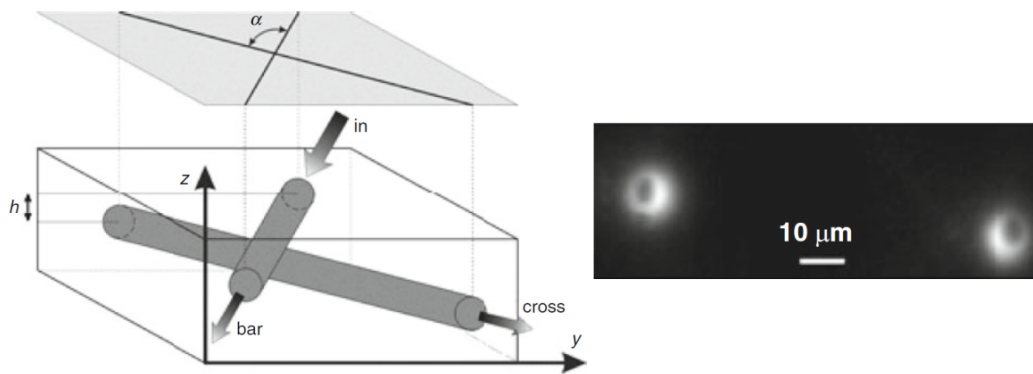
Figure 2.7: Schematic of an X-coupler, where the power coupling takes place at the angle α. The near field profile of the output facet when a 1550 nm light is coupled is shown on the right. Image taken from [72].

coupler has been reported in 2001 and it is due to Streltsov and Borrelli [71]. The coupler was fabricated with an asymmetric geometry, composed by a straight and a curved flanked waveguides, with a core to core distance at the coupling region of $3.5\,\mu$m. The single mode operation and a splitting ratio of $1.9\,$dB was demonstrated for visible light at 633 nm. The 3D capability of FLM has been exploited extensively also in the fabrication of directional couplers. For example, Osellame at al demonstrated in 2005 the possibility to fabricate an X coupler, a power coupler with a 3D geometry shown in Figure 2.7 [72] . In this case, the waveguides at the coupling region are fabricated in non-collinear directions, at two different depths. The power transfer is still achieved via evanescent waveguide coupling, but the splitting ratio is determined by the height difference h and by the coupling angle α. An equal power splitting was demonstrated with this device for 1550 nm light. The wavelength dependence of the splitting ratio of femtosecond laser written directional couplers has been exploited to fabricate wavelength multi and demultiplexers [73], devices that play a crucial role in optical networks and for sensing purposes. However, this wavelength sensitivity can also represent a limit for other applications and it can be overcome by a careful choice of the geometric parameters in the coupler design. For example, Chen et al demonstrated the functioning of a wavelength insensitive directional coupler over a bandwidth of 400 nm, centered at 1450 nm [74]. Even polarization dependence can be exploited in some technologies (i.e. polarization sensitive devices) or avoid it in others where it is prejudicial [75].
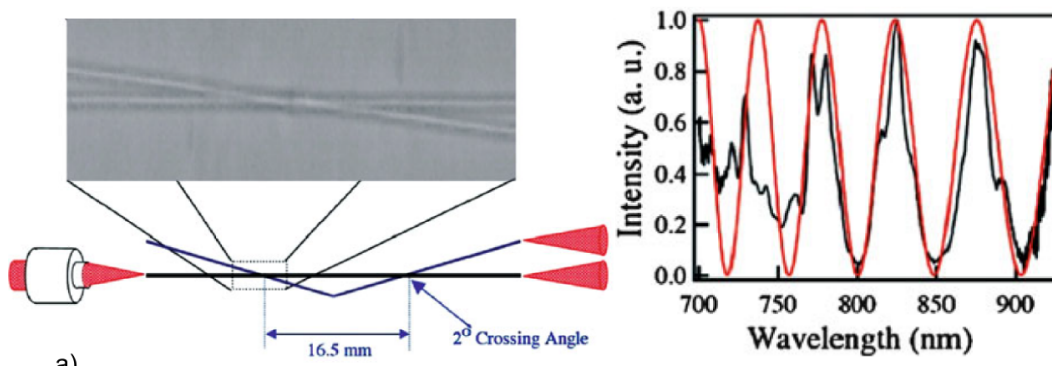
Figure 2.8: Mach-Zehnder interferometer fabricated by the concatenation of two X-couplers. In the right panel the measured output spectrum is shown (black line) and compared to the theoretical model (red curve). Image taken from [76].

2.4.2 Mach-Zehnder and multi-port interferometers

A Mach-Zehnder interferometer is a device where a light beam is divided at a first splitter along two branches, then recombine on a second splitter or coupler. The output power depends on the phase difference established between the two beams as they were following different routes: constructive or destructive interference can happen via geometric imbalance of the optical paths or modulation of the refractive index by one of many physical phenomena. The first demonstration of an integrated Mach-Zehnder interferometer fabricated by FLM is due to Minoshima et al in 2002, fabricated by cascading two X-couplers [76]. A schematic of this device is depicted in Figure 2.8. The simple layout saw two waveguides intersecting in two X-coupler sections at an angle of 2°, with a geometrical path difference of 10 μm in the intermediate section. Due to such difference, interference fringes were observed in the output light spectrum when broadband light, emitted from a Ti:Sapphire laser, was introduced in the device. The functioning of the interferometer as a spectral (or wavelength) filter was thus validated.

2.4.2.1 Thermo-optic phase shifter

A further step towards practically reconfigurable Mach-Zehnder devices was made in 2015, with the extension of thermal phase shifters to femtosecond laser waveguide inscription [77]. After the fabrication of a Mach-Zehnder interferometer in an alumino-borosilicate glass sample, a 50 nm thick gold layer was sputtered on the upper surface and etched with the same femtosecond laser, in order to pattern thin resistors aligned with the interferometric arms (Figure 2.9).

The idea behind these implementation is easy: when an electric current is forced in these resistive sections, electrical power is dissipated in the form of heat, by Joule effect. Thus a temperature gradient, decreasing radially from the axis of the heater, is created inside the material (being the thermal conductivity of glass much higher than that of air at standard conditions). In the hypothesis in which the temperature-induced refractive index variation in the glass is linear, the induced phase difference between the arms $\phi = \phi_1 - \phi_2$ is linear with the dissipated power P_{diss}. Considering a single resistor acting on a single interferometer, for coherent light injected in one input, interference fringes can be observed by monitoring the intensity of either one of the two outputs, as follows:

$$I_{out} = \frac{I_{tot}}{2} \left[1 + \mathcal{V} \cos \phi \right] = \frac{I_{tot}}{2} \left[1 + V \cos \left(\phi_0 + \alpha P \right) \right] \tag{2.4.3}$$

where I_{tot} is the sum of the intensities on the two outputs, $\mathcal{V}$ is the fringe visibility, and ϕ_0 is a phase term present in the interferometer when no power is applied to the heater. α is a constant that depends on all the geometric, thermal, and optical properties of the interferometers. Assuming a wire-like heater and neglecting power dissipation from the top surface of the glass (air is an insulator), a logarithmic decay law for the temperature as a function of the distance from the heater can be easily determined. Within this simplified model, an analytic expression for α can be found:

$$\alpha = \frac{2 n_T}{\lambda} \frac{1}{\kappa} \frac{L_{arm}}{L_{wire}} \ln \frac{\rho_1}{\rho_2} \tag{2.4.4}$$

where κ is the thermal conductivity of the glass substrate, n_T is its thermo-optic coefficient, λ is the wavelength, L_{arm} is the length of the straight segments in the interferometer's arms, and L_{wire} is the length of the wire-like heater. Once the laser and the substrate is fixed, the coefficient α depends just on the distances ρ_1 and ρ_2 of the interferometer's arms from the heater. A measurement of interferometric fringes allowed to retrieve high-visibility oscillations in the output intensity, and to validate a linear modulation of the phase with the dissipated power. A proportionality factor of $\alpha = 13.43$ rad/w was extracted from a sinusoidal fit. The thermo-optical technology discussed in this last paragraph was also largely employed in the present thesis work, in order to achieve reconfigurable phases in the final device, as we will explain later on.
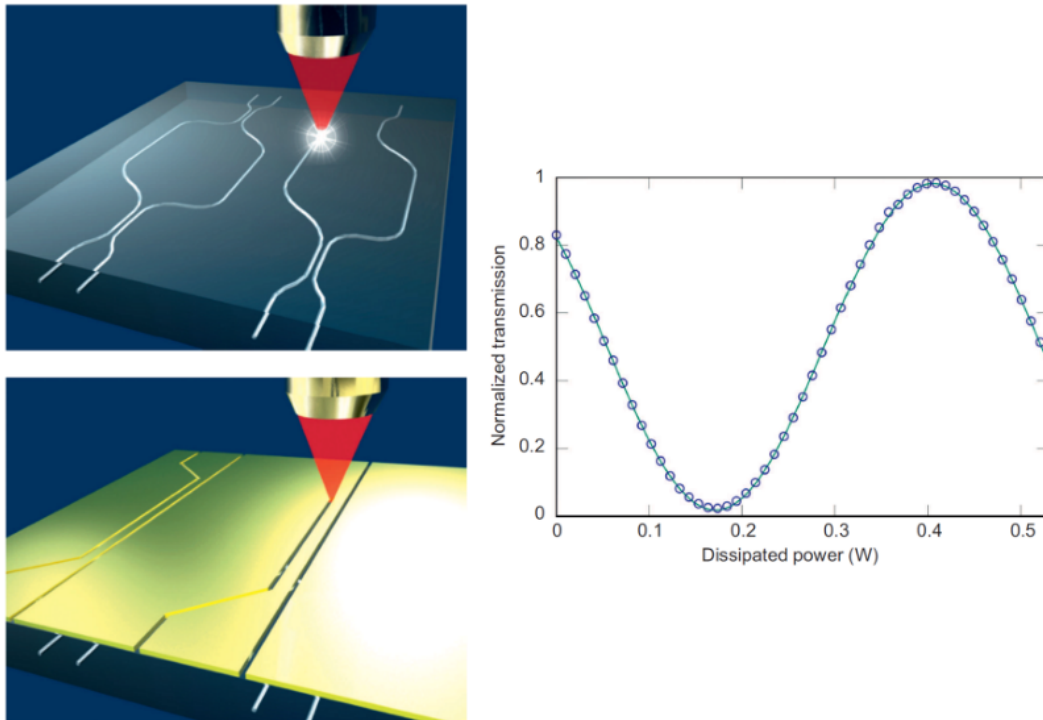
Figure 2.9: Left: computer rendering of FLM patterning of thin gold thermal shifters, aligned with the arms of the Mach-Zehnder interferometers underneath. After gold coating the sample top surface, the resistors are patterned by ablation using the same femtosecond laser. Accurate alignment ($\simeq 1\,\mu$m) between the resistors and the Mach-Zehnder arms is achieved by using the reference markers inscribed on the Right: Interference fringes of coherent light with $\lambda = 1550$ nm as electrical power was dissipated inside the shifter. Images taken from [77].

Experimental set-up

3.1 Fabrication setup

T$_{HE}$ schematic of the experimental setup used to fabricate the optical circuits described in this thesis is shown in Figure 3.1. A cavity-dumped mode-locked oscillator generates femtosecond laser pulses at 1030 nm, which is delivered through a system of dielectric mirrors to the machining area. Here, thanks to a microscope objective, the writing beam is focused inside the substrate (in this specific case a Eagle XG glass) that is glued on a computer driven, three dimensional, linear motion system. A precise alignment is provided by a series of mirrors and a gimbal-based adjuster (Thorlabs GM100) mounted on the translation stages. Several objectives are available for the beam focusing, with numerical apertures ranging from 0.3 to 1.4 (oil immersion). A CCD camera mounted above the objective is used to collect the collimated back-reflected light from the sample surface. This allows for a micrometric control in the positioning of the fabricated structures into the substrate, by setting to set correctly the reference system for the writing process. The average laser power delivered to the sample can be tuned by rotating a half-wave plate placed before a Glan-Thompson polarizer, which also sets the polarization used for the fabrication. Synchronized with the motion stage, a mechanical shutter (Thorlabs SH05) is present in order to fast switching the laser during the fabrication (ON-OFF cicle performed in about 10 ms) and to obtain the desired geometry. A second harmonic generation
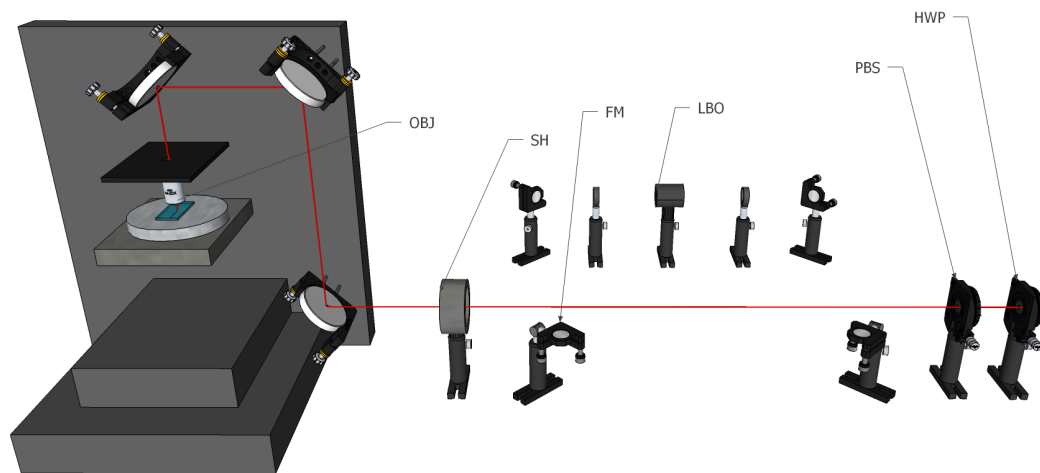
Figure 3.1: Schematic of the fabrication setup: a femtosecond laser beam at 1030 nm (Yb-based cavity-dumped mode-locked oscillator) is focused by a microscope objective (OBJ) on the substrate (Eagle XG), which is glued on a three-dimensional high precision translation stage (Aereothech a3200). A Glan-Thompson polarizer (PBS) and a half-wave plate (HWP) are used to tune the laser power, while a mechanical shutter (SH) synchronized with the motion stage allows a fast laser switching. Two flip mirrors (FM) are used to deviate the laser beam to a second harmonic generation stage (the second optical line on the table) where the beam is focused by a 15 mm focal lens into a temperature controlled lithium triborate crystal (LBO) and the generated light is collimated by a 30 mm focal lens. This allows to switch the laser wavelength from 1030 nm (displayed in red) to 515 nm (green), according to the processed material.

stage can be introduced in the optical path by using two flip mirrors, which deviate the beam to a temperature controlled lithium triborate crystal. This allows to choose, as fabrication wavelength, between the fundamental and its second harmonic (515 nm).

3.1.1   Laser source

The laser source used for the waveguide writing process is a cavity-dumped mode-locked oscillator, capable of providing pulses with 350 fs time duration and maximum energy of $1\,\mu J$. It was developed in a collaboration between the Max Planck Institute of Heidelberg (Germany) and HighQLaser GmbH (Austria) [78]. The active medium is a $KY(WO_4)_2$ (Potassium Yttrium Tungstate) crystal, doped with Ytterbium at 5% concentration, and the emission wavelength is 1030 nm. The pumping system is based on a InGaAs multi emitter laser diode bar at 980 nm and the optical pump power used is in the order of 15W. The laser cavity, about 8.9 m long, is actually reduced to a footprint of 90 cm x 50 cm by a series of mirrors. The passive mode-locking regime, which generate a train of pulses at 17 MHz, is reached with a SESAM (SEmiconductor Saturable Absorber Mirror) used as end mirror of the laser cavity. The cavity dumping (pulse extraction) is performed by a Pockels cell combined with a Thin Film Polarizer (TFP). In particular on the Pockels cell it acts an external electronic driver, synchronized to the train pulse, which can be tuned in its voltage and repetition rate. A laser pulse is extracted from the cavity when the Pockels cell induces a polarization rotation, causing the reflection of part of the pulse by the TFP. The available output repetition rate spans the integer submultiples of 17 MHz from few kHz to 1.1 MHz. Finally, acting on the dumping ratio, is possible to get a pulse duration from about 250 fs to 400 fs according to the pseudo-solitonic regime sustained by the cavity [43].

3.1.2   Translation stages

The relative motion between the focal spot of the laser and the sample is ensured by means of a three dimensional computer-controlled motion system (Aerotech FIBERGlide 3D). This system is composed by three independent linear translation stages, lying on air bearing and driven by a brushless linear electric motor. In this way, a smooth and uniform three dimensional movement is achieved, with a position accuracy of 100 nm, velocities up to 100 mm/s and trans-

lation ranges of 10 cm x 15 cm in the substrate plane and 5 mm in the vertical direction. Nanometric optical encoders monitor the stage position constantly with a resolution on 1 nm. This system is computer controlled and is programmable by G-Code language, typically used in CNC machining.

3.2   Characterization setup

Once fabricated, the optical circuits need to be characterized in order to study their properties and verify their functioning. For this reason, different measurements are performed.

3.2.1   Microscope inspection

The first circuit characterization is its visual inspection by means of an optical microscope. The observation from the top surface allows to check the uniformity of the waveguides, since they could be damaged by interruptions or by defects in their paths (Figure 3.2a), caused e.g. by the presence of dust on the sample surface during the fabrication. It is also possible to inspect the lateral sample facets for analyzing the cross-section of the waveguides (after a proper sample polishing, Figure 3.2b). The optical microscope employed is a Nikon ME600, equipped with an optional Differential Interference Contrast (DIC) module, allowing enhanced vision of small index contrasts by exploiting interference phenomena. In addition, a high resolution CCD camera (PixeLINK B871) is mounted on the microscope for pictures acquisition.

3.2.2   Device coupling with classical light

A crucial step in the characterization of the waveguides is the measurement of the radiation confinement characteristics, since this allows to infer all the information about their behavior in terms of guiding properties, supported mode profile and polarization behavior. In order to do that, we couple the waveguides with classical light. Here we will focus on two possible configuration, the "end-fire" and the "fiber-butt" configuration. These two configurations share the same input light, that is provided by a series of diode and solid state lasers, spanning from 607 nm to 1550 nm, and by a HeNe laser emitting at a wavelength of 633 nm.
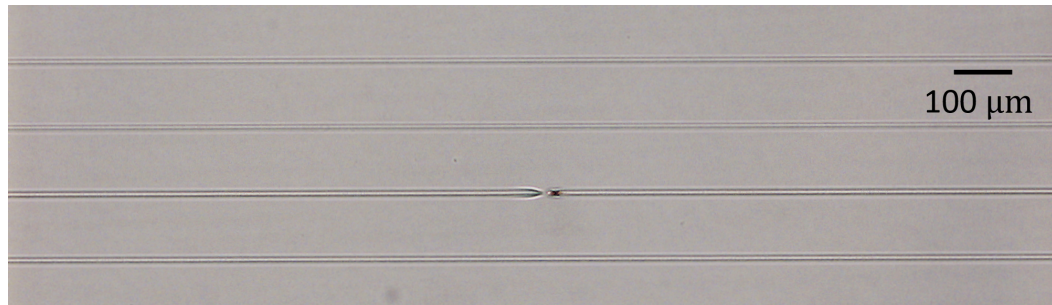
(a)

(b)
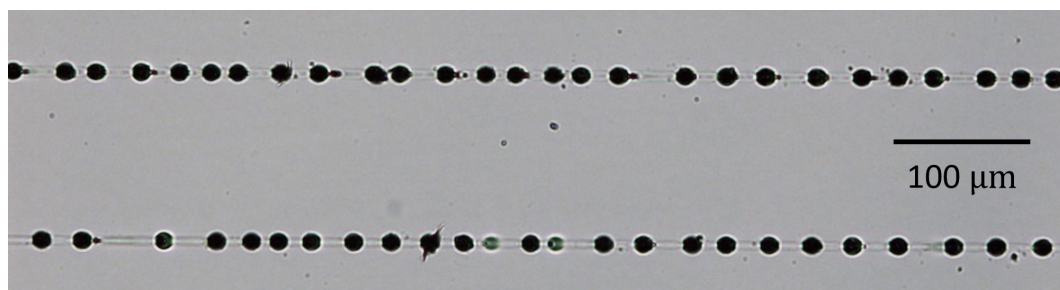
(c)

Figure 3.2: Some images taken with the optical microscope of details on chip fabricated by FLM. By visual inspection we can check the presence of interruptions (a) avoiding wrong conclusion on the quality of the guide; we can control the quality of the superficial polishing, avoiding scattering issue at the input and output faces (b); we can study the effect of different parameters in the fabrication process, for example in (c) a too high power led to this bubble-like ablation of the guide.
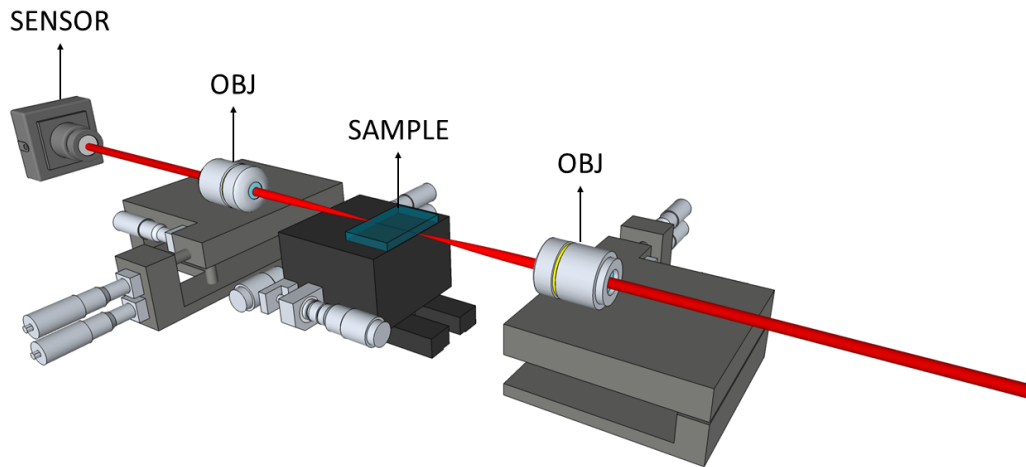
Figure 3.3: End-fire coupling configuration: a microscope objective (OBJ) focuses the laser beam in the waveguide (WG) input facet. Another objective (OBJ) is used to collect the output light and to focus it either on a powermeter head (PM) or an imaging camera (IC).

End-fire configuration   It consists in using a microscope objective or an aspheric lens to focus a collimated coherent light beam into the input facet of the waveguide. In order to get an optimal coupling, both the numerical aperture and the focal spot size of the objective should match as much as possible the waveguide NA (~ 0.1 in FLM waveguides) and mode size. The output light is then collected by another objective and imaged on a sensor, usually a powermeter (Ophir NovaII and Anritsu ML9001A) or an imaging camera (CCD camera Emdund OpticsEO-1312M for visible light, vidicon camera Hamamatsu C2400-03A and InGaAs camera Xenics Bobcat-640 for infrared light).

Fiber-butt configuration   In this case, the laser beam is coupled in a single mode fiber, whose end, after a proper peeling and cleaving, is brought close to the waveguide input facet. This configuration is used when a comparison between waveguide and fiber properties must be performed.

The objectives, the fiber and the optical chip are positioned on sub-micrometric positioning systems, to guarantee a precise and stable alignment of the objective (since the waveguides mode is in the order of ten micrometer radius). Because of this, a three-axis micro-positioner (Melles Griot NanoMAX) with 50 nm resolution on each axis is employed to move the input objective (or the fiber), while the
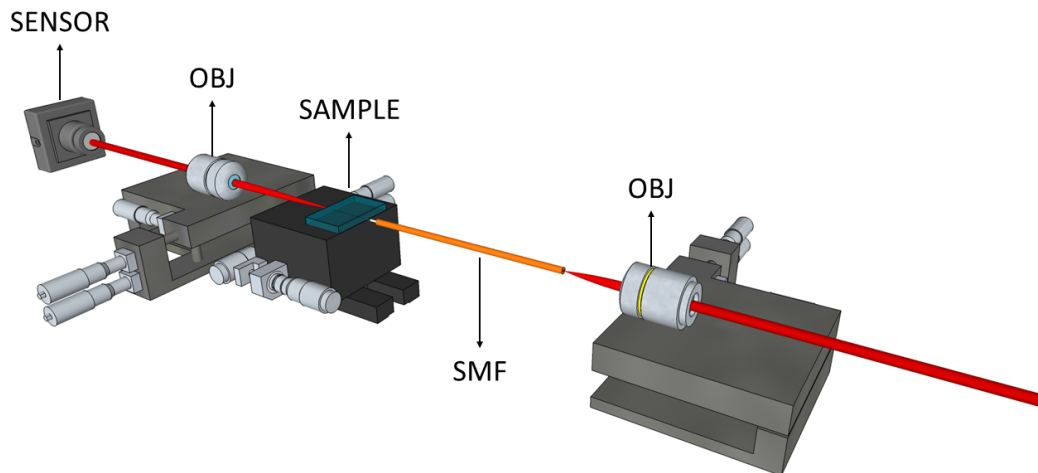
Figure 3.4: Fiber-butt coupling configuration: the laser beam is focused by a microscope objective (OBJ) into a single mode fiber (SMF), which is then coupled to the waveguide (WG) by bringing it close to its input facet.

sample is hold on a second stage, a four-axis manipulator (Thorlabs MBT 402). In the latter, besides two linear translations (on the plane), there are two independent tilting adjustments. Finally, the collection of the output light is made with another microscope objective with higher NA mounted on a three-axis manipulator and the imaged on a power meter head or a video-camera.

3.2.2.1 Mode profile

A fundamental waveguide property that has to be measured is the spatial intensity profile $I_{wg}(x, y)$ of the guided light. By its analysis it is possible to distinguish between single and multimode waveguides, to measure the size of the guided mode and to obtain information on the coupling losses. Single mode operation is crucial for the vast majority of integrated optical applications, since it avoids inter-modal power transfers and thus it allows a proper engineering of the waveguides coupling, as it will be explained in the following paragraph.A possible method for its measurement is by employing the fiber butt-coupling configuration (Figure 3.4). The near field image of the output mode is imaged, by a microscope objective, onto a CCD camera (attenuation of the input laser beam can be necessary to cover the whole camera dynamics without saturating its response). Once the image is acquired via software, the device is removed and the fiber end is brought close to the collection objective, without moving the objec-

tive and the camera, to keep constant the magnification ratio. In this way we can collect the fiber output intensity profile in order to calibrate the image dimension of the waveguide intensity profile (since the fiber mode diameter is known). Finally a numerical analysis on the acquired images is performed: in fact, in case of single mode waveguides, the theory guarantees that the fundamental guided mode does not present any sign inversion and so the spatial field distribution is:

$$\left| E_{wg}(x,y) \right| \propto \sqrt{I_{wg}(x,y)} \qquad (3.2.1)$$

so we can retrieve the information on the field modulus by simply looking at the normalized intensity profile.

3.2.2.2   Losses characterization

Another important characterization regards the unavoidable losses of the fabricated integrated circuit. It is crucial to quantify accurately the losses in quantum applications since they can heavily effect the performances (for example decreasing the efficiency of the device and so increasing of the time of execution of a measurement). The first measurement to be performed is about the insertion losses (IL) of the device. IL are defined as the total losses introduced by the presence of the circuit, and are usually expressed in decibel:

$$IL_{dB} = -10 \log_{10}\left(\frac{P_{out}}{P_{in}}\right) \qquad (3.2.2)$$

where P_{out} and P_{in} are respectively the waveguide output and input power, i.e. measured at the fiber output in the case of fiber-butt configuration. The insertion losses can be measured with the same setup described for the mode profile measurement, but with a powermeter head replacing the camera. The insertion losses are actually the result of different physical processes and can be decomposed in four different kind of terms: Fresnel Losses (FL), Propagation Losses (PL), Coupling Losses (CL) and Bending Losses (BL). The relation between the losses can be expressed as:

$$IL_{dB} = 2\,FL_{dB} + CL_{dB} + PL_{dB/cm} \cdot l + BL_{dB/cm} \cdot l_c \qquad (3.2.3)$$

The meaning of the different terms is explained in the following paragraphs.

Fresnel Losses (FL)   Are caused by the refractive index discontinuity at the air substrate interface which brings to a partially refection of the light. From the Fresnel equation for refection, this kind of losses can be expressed as:

$$FL_{dB} = -10 \log_{10} \left[1 - \left(\frac{n_2 - n_1}{n_2 + n_1} \right)^2 \right] \qquad (3.2.4)$$

where n_1 and n_2 are refractive indexes of glass and air respectively. In a common situation we have air ($n_1 = 1$) and glass ($n_2 = 1.5$) so that $FL = 0.177\,\text{dB}$ for both interfaces, input and output. The factor 2 in front of the FL term in Equation 3.2.3 takes into account both input and output facets.

Coupling Losses (CL)   Are related to the mismatch between the waveguide and the incoming light distribution. They can be calculated as:

$$CL_{dB} = -10 \log_{10} \left(\frac{\left| \iint E_{wg} E_{in} \partial x \partial y \right|^2}{\iint |E_{wg}|^2 \partial x \partial y \cdot \iint |E_{in}|^2 \partial x \partial y} \right) \qquad (3.2.5)$$

where the logarithm argument represents the overlap integral between the two electric field modes, retrieved from the two intensity distributions as explained in section 3.2.2.1.

Bending Losses (BL)   When a waveguide is curved, the guided mode distribution is distorted and a partial coupling with radiation modes occurs. This phenomenon can be understood also in the ray description. Indeed, if a waveguide is bent, the guided rays will impinge on the core-cladding interface with a higher incidence angle, thus increasing the probability of being transmitted in the cladding. In particular, we look at the losses produced by a curved segment with radius R: as R increases, the contribution of losses decreases exponentially. To measure the BL dependence on the radius of curvature, straight waveguide and a series of bent ones, with different radii of curvature but the same bent path l_c, are fabricated. For every radius, the BL are computed by comparing the losses with the ones introduced by the straight waveguide:

$$BL_{dB} = \frac{(IL_i)_{dB} - (IL_{SWG})_{dB}}{l_c} \qquad (3.2.6)$$

where (IL_i) are the Insertion Losses for the bent waveguide and (IL_{SWG}) for the straight one.

Propagation Losses (PL)   Consist in the exponential attenuation of guided light during propagation, due to the rugosity and possible defects inside the waveguide, like small inhomogeneity of the refrative index. The propagation losses can be calculated as:

$$PL_{dB/cm} = \frac{10}{l} \cdot \log_{10}\left(\frac{P(0)}{P(l)}\right) \tag{3.2.7}$$

The most correct way to retrieve the propagation losses is to measure the output power of a straight waveguide for different lengths by cutting it several times: this method is time consuming and destructive for the sample. The commonly used method is the indirect one: we calculate the PL by inverting the Equation 3.2.3:

$$PL_{dB/cm} = \frac{1}{l}\left[IL_{dB} - (2\,FL_{dB} + CL_{dB} + BL_{dB/cm} \cdot l_c)\right] \tag{3.2.8}$$

Obviously this method introduces more uncertainty on the actual value, since all the uncertainties of the different measurements add up.

3.2.2.3   Splitting ratio characterization

The fundamental property of a DC is its splitting ratio, so the ratio between the reflectivity R and transmissivity T defined in Subsection 2.4.1. So in order to fully characterize a DC we need to gather information on R (being $T = 1 - R$). To do that, we can couple light in the sample both in the end-fire or in the fiber-butt configuration. Coupling light in one input, for example IN_1 in Figure 2.6, and acquiring both the output intensities of OUT_1 and OUT_2 with a powermeter, namely P_1 and P_2, we can define the reflectivity of the DC simply as:

$$R = \frac{P_1}{P_1 + P_2} \tag{3.2.9}$$

In this way we take in account the all the losses of the device, normalizing the value on the actual guided light. This simple method can be extended to more complex design so evaluate the splitting ratio in an interferometric device, as we will see in Chapter 5.

Aim and design of the project

4.1   Aim of the project

$\mathbf{A}$s we have seen in Chapter 1, quantum metrology aims to exploit quantum resources to enhance the sensitivity in the estimation of unknown physical parameters with respect to classical approaches. We have said that, in the single parameter case, the estimation of an unknown physical quantity with classical resources is bounded by standard quantum limit (SQL), while adopting quantum resources we can define the more fundamental Heisenberg limit (HL). Given a probe preparation, the optimal limit for single parameter estimation can be always saturated [79, 80]. The problem is that a large variety of estimation problems involve more than a single physical quantity, such as phase imaging [81], magnetic field imaging [82] and state estimation [83], just to cite some. Although multi-parameter estimation holds this broad range of applications, there are still several open questions with respect to the single parameter case. For instance, no complete recipes are known in the multi-parameter case to saturate the resolution of measurement [84]. The problem arises from the possible non commutativity of the quantum measurements required to simultaneously optimize the estimation of different parameters. However, in the case of compatible d parameters, a reduction of resources by a factor d can nevertheless be obtained with respect to single individual estimations [85]. The most suitable platform to implement multiphase estimation tasks is provided by integrated multi-arm
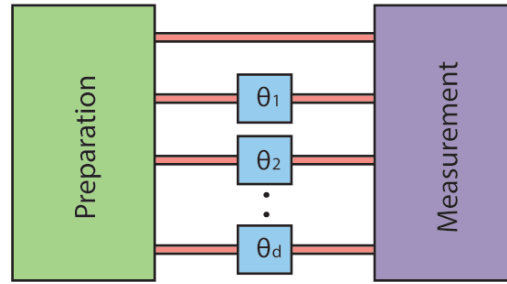
Figure 4.1: Discretised phase imaging model. We consider the simultaneous estimation of d phases using a setup consisting of state preparation (green), independent phase application in each mode (blue) and state measurement (purple). Image taken from [86].

interferometers injected by multiphoton states. Such platform presents several advantages in terms of stability, tunability and compactness of the devices, as we can conclude from Subsection 1.2.

The aim of this thesis work is the fabrication and characterization of a four-mode interferometer built through the femtosecond laser writing (FLW) technique. This device can be used both to perform quantum-enhanced single phase measurement and to implement quantum multiphase estimation task.

4.2 Design of a four-arm interferometer

4.2.1 Multimode interference device

Any linear optical component can be described by a transition matrix M that maps input fields to output fields. Ideally, a balanced 2×2 multimode interference (MMI) splitter should perform the same operation as a 2×2 directional coupler with a unitary matrix that describes the evolution from input to output:

$$\text{M}_{2\text{x}2} = \frac{1}{\sqrt{2}} \begin{pmatrix} 1 & i \\ i & 1 \end{pmatrix} \tag{4.2.1}$$

which equally superposes the two modes. In the 2×2 case, there is only one equivalence class of symmetric splitters, this corresponds to the fact that different physical implementations can have different external phase relations, but the general description of the transformation is dictated by the unitary evolution. [87]. In 1994, Reck et al. [88] presented an algorithmic proof that any discrete
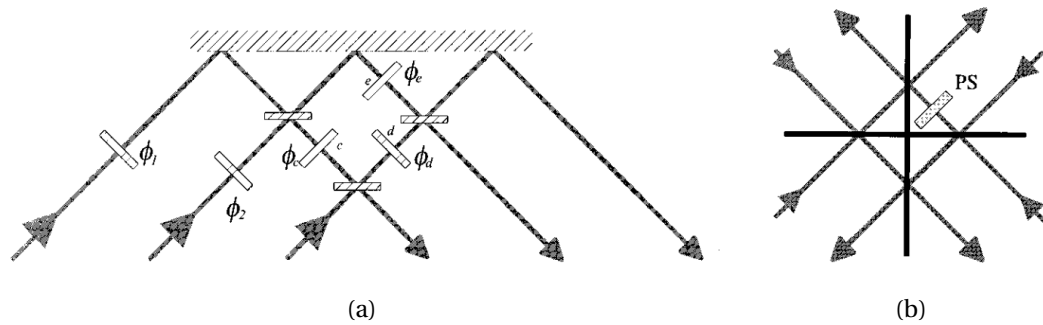
Figure 4.2: *(a)* Tritter. The lowermost beam splitter has a reflectivity $R = \frac{1}{3}$; for the other two $R = \frac{1}{2}$, and at the top we have a mirror, i.e., an $R = 1$ device. If suitable internal phase shifts are applied, the probabilities for a single photon entering via any input port to exit via any output are equal. *(b)* Quarter. All beam splitters have a reflectivity $R = \frac{1}{2}$ and the probabilities for a single photon entering via any input port to exit via any output are equal. An internal phase ϕ can be fixed by a single-phase shifter (PS) inserted into one of the internal paths within the device without modifing these probabilities. Each value of the phase defines equivalence class of symmetric eight-port beam splitters (i.e. quarter). Images taken from [87].

finite-dimensional unitary operator $U(N)$ can be constructed using a pyramid-like network of standard beam splitters (i.e. of two input and two output ports), mirrors and phase shifters. For example we can build a 3x3 MMI splitter, i.e. a tritter, just using three beam splitters and some phase shift (Figure 4.2a). Interestingly, the description of multiport splitters grows in complexity with N. For $N \leq 3$, all symmetric N×N splitters can be described by one equivalence class, as the requirement on the conservation of energy defines the matrix to within external phases on the input and outputs [89]. However, when $N \geq 4$, there exists an infinite number of distinct equivalence classes, and the internal free phase ϕ is independent of the conservation of energy.

4.2.2 Quarter

A quarter is a MMI device that splits the input power from one of its four input, equally into its four output. The transition matrix that describes an ideal
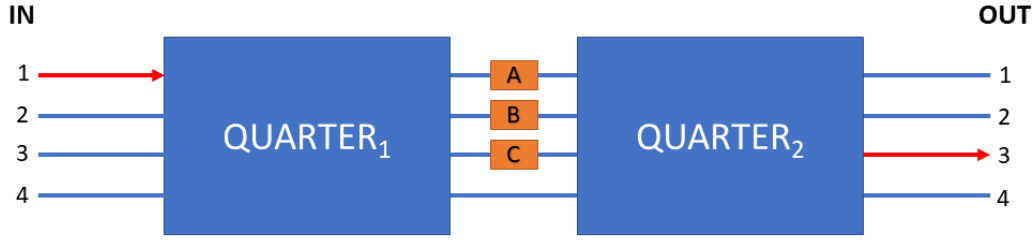
Figure 4.3: Schematic of the four-arm interferometer. When both internal phases ϕ_1 and ϕ_2 of the two quarter forming the four-arm interferometer are set equal to zero, a unique relation between an input and output guides can be found. For example, entering input 1 will produce an output just on output 3 ($1 \rightarrow 3$).

symmetric 4×4 MMI splitter is:

$$
M_{4x4}(\phi) = \frac{1}{2}
\begin{pmatrix}
e^{i\phi} & e^{i\phi} & 1 & 1 \\
-e^{i\phi} & -e^{i\phi} & 1 & 1 \\
-1 & 1 & -1 & 1 \\
1 & -1 & -1 & 1
\end{pmatrix}
\tag{4.2.2}
$$

where ϕ is the free internal phase. In general, two different physical implementations would correspond to a different equivalence class and a different value of ϕ. . The equivalence classes are continuously parameterized by the phase ϕ of the range between 0 and π [87]. An example of a symmetric eight-port beam splitter is reported in Figure 4.2b.

4.2.3   Four-arm interferometer

A four-arm interferometer is built by the combination of two consecutive quarters, with the addition of some phase terms in the middle region. We will referr to these phases as *A, B* and *C*, defined with respect to the phase on the fourth mode, as in Figure 4.3. The total matrix, calculated using the quarter matrix in Equation 4.2.2, can be written as:

$$
M_{\text{4-arm}} \quad = \quad M_{4x4}(\phi_2) \cdot M_{\text{phases}} \cdot M_{4x4}(\phi_1)
\tag{4.2.3}
$$

in which

$$M_{\text{phases}} = \begin{pmatrix} e^{iA} & 0 & 0 & 0 \\ 0 & e^{iB} & 0 & 0 \\ 0 & 0 & e^{iC} & 0 \\ 0 & 0 & 0 & 1 \end{pmatrix} \tag{4.2.4}$$

At the end we obtain:

$$M_{\text{4-arm}} = \frac{1}{4} \left(\begin{array}{cc} e^{iC} + e^{i(A+\phi_2+\phi_1)} - e^{i(B+\phi_2+\phi_1)} - 1 & 1 + e^{i(A+\phi_1+\phi_2)} - e^{i(B+\phi_1+\phi_2)} - e^{iC} \\ e^{iC} - e^{i(A+\phi_2+\phi_1)} + e^{i(B+\phi_2+\phi_1)} - 1 & 1 - e^{i(A+\phi_1+\phi_2)} + e^{i(B+\phi_1+\phi_2)} - e^{iC} \\ -e^{iC} - e^{i(A+\phi_1)} - e^{i(B+\phi_1)} - 1 & e^{iC} - e^{i(A+\phi_1)} - e^{i(B+\phi_1)} + 1 \\ e^{iC} - e^{i(A+\phi_1)} - e^{i(B+\phi_1)} + 1 & -e^{iC} - e^{i(A+\phi_1)} - e^{i(B+\phi_1)} - 1 \end{array}\right.$$

$$\left.\begin{array}{cc} -e^{iC} - e^{i(A+\phi_2)} - e^{i(B+\phi_2)} - 1 & -e^{iC} + e^{i(A+\phi_2)} + e^{i(B+\phi_2)} - 1 \\ -e^{iC} + e^{i(A+\phi_2)} + e^{i(B+\phi_2)} - 1 & -e^{iC} - e^{i(A+\phi_2)} - e^{i(B+\phi_2)} - 1 \\ e^{iA} - e^{iB} + e^{iC} - 1 & -e^{iA} + e^{iB} + e^{iC} - 1 \\ e^{iA} - e^{iB} - e^{iC} + 1 & -e^{iA} + e^{iB} - e^{iC} + 1 \end{array}\right) \tag{4.2.5}$$

Is interesting to note that, when both internal phases (ϕ_1 and ϕ_2) and the inter-ferometric phases (*A*, *B* and *C*) are set equal to zero, we find a unique relation between an input and output guides. Indeed, entering, for example, from input 1 will produce an output just on output 3 ($1 \rightarrow 3$). In the same way

$$2 \rightarrow 4 \qquad 3 \rightarrow 1 \qquad 4 \rightarrow 2 \tag{4.2.6}$$

A graphic example is shown in Figure 4.3.

4.3   Quantum enhanced estimation of parameters

In this section, we will briefly show how to take advantages from a four-arm interferometer to enhance the estimation in case of single and multi parameters. Since the experiments on this device will be performed by the QUANTUM INFOR-MATION LAB at La Sapienza University, we will just give an overview of them.

4.3.1 Single-parameter estimation

Whereas optical interferometry relying on classical interference is intrinsically a single-particle process, quantum advantages arise when quantum-correlated states of more than one particle are employed, as we've seen in Subsection 1.2.3.1. N00N states, in particular, allow to saturate the HL of sensitivity. Increasing the number of modes to more than two represents an interesting possibility to extend the concept of multiparticle interferometry, but this requires multi-port devices, instead of simple two-mode beam-splitters, for building multi-arm interferometers. Considering the action of a single quarter on an input Fock state

$$\psi_{\text{in}} = |1, 1, 1, 1\rangle \qquad (4.3.1)$$

we can calculate the output wavefunction [16]:

$$\psi_{\text{out}} = c_1 |1, 1, 1, 1\rangle + c_2 |2, 2, 0, 0\rangle + c_3 |4, 0, 0, 0\rangle \qquad (4.3.2)$$

where the c_is are probability amplitude. To simplify the notation, we are condensating all the possible permutation of the last two terms. As in the $N = 2$ case, we observe that some terms of the output states (the $|3, 1, 0, 0\rangle$ and $|2, 1, 0, 0\rangle$) are suppressed due to quantum interference. This is the N-mode analogue of the Hong-Ou-Mandel effect that we have yet observed in lower NOON states. The peculiar cooperative behavior of these entangled photons lead to a specific probability factor that varies as $\cos(4\varphi)$, thus giving the possibility to obtain a measurement on the phase φ with an uncertainty of $1/4$ (instead of the classical $1/\sqrt{4}$).

4.3.2 Multi-parameter estimation

The same four-arm interferometer can be adopted to perform a two (or three) parameter estimation process, consisting of the simultaneous measurement of two (or three) optical phases. The theory behind multiparameter estimation in a four-port interferometer goes beyond the scope of this thesis. However, a brief introduction to the topic will be given to complete the dissertation. The problem has to be found in the possible non-commutativity of the quantum measurements required to simultaneously optimize the estimation of different parameters. However, different groups are trying to put the basis of a general method to find the optimal quantum estimator ans evaluate it's precision bounds [90, 91].

The basic idea is that, in order to reach the maximum precision allowed we need to prepare the system in a specific configuration. This is due to the fact that different hamiltonians have different bounds, so to achieve the optimal result we need to act on the device: in the case of multiple phase estimation, we need to have controllable phases in addition to the unknown one. This degree of freedom allow the implementation of an adaptive estimation scheme [92]: once obtained a rough estimate of the unknown phases, a second step is exploited to tune the system to operate in the optimal regime by means of appropriate phase shifts. This is an iterative procedure, and at each step of the protocol, the measurement outcomes are analyzed by a Bayesian approach assuming no a-priori knowledge on φs, updating the probability distribution. A practical example can be found in the work of Spagnolo et al [93].

Fabrication of the optical device

5.1 Waveguide fabrication process

5.1.1 Thermal annealing

I N Section 2.3 we have seen how Arriola et al. had applied a typical industrial process as the thermal annealing to FLM written waveguide, obtaining low losses and a almost no birefringence. Due to this reason, we decided to apply the annealing technique to our fabrication process and so on the Eagle XG®substrate, whose thermal key points are listed in Table 5.1.

Annealing point [°C]	722
Softening point [°C]	971
Strain point [°C]	669

Table 5.1: Thermal key points of Eagle XG® substrate from Corning®.

Searching in the literature, once the glass is brought above the annealing point, two possible cooling-schedule can be implemented [94]:

- a constant cooling rate, that consist in cooling at a constant rate the glass in such a way that all parts of the glass receive exactly the same time-temperature treatment. The Arriola routine falls into this category.
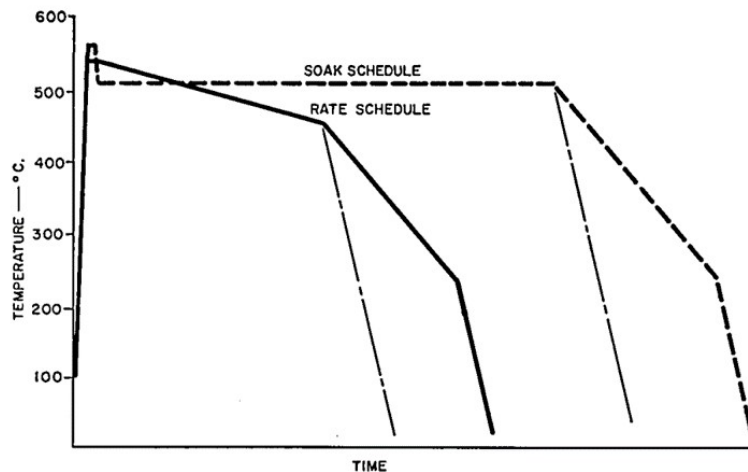
Figure 5.1: Comparison of soak and rate annealing schedules for a borosilicate glass. Image taken from [94].

- a constant temperature soaking, that consist in quickly drop the temperature in the lower end of the transformation range. Here, a long soak is performed to release the stresses, due to the grater the time constant of glass. Low soaking temperatures require very long periods of holding, but the rate of subsequent cooling can he relatively slow without destroying the established uniformity. A comparison between the two method can be found in Figure 5.1.

Thus we tried different annealing routine:

1. A constant heating ramp at $100\,^{\circ C}/h$ up to 600°C, then up to 750°C at $75\,^{\circ C}/h$ followed by a constant cooling ramp at $-12\,^{\circ C}/h$ (Figure 5.4a). The same routine was repeated changing the highest temperature to $820\,^{\circ C}/h$.

2. Same as routine 1, but we introduced two slabs of high conductive metals, in our case silicon, above and below the sample, in order to bring about isothermal boundary conditions by virtue of the high thermal conductivity of the semiconductor [94].

3. A constant heating ramp at $100\,^{\circ C}/h$ up to 600°C, then up to $820\,^{\circ C}/h$ at $75\,^{\circ C}/h$. After a plateau of 3 hours, the temperature is dropped to 600°C at a symmetric cooling rate of $-75\,^{\circ C}/h$, followed by a soaking of 30 hour of holding and a constant cooling ramp at $-20\,^{\circ C}/h$ (Figure 5.4b).

4. A constant heating ramp at $100\,^{\circ C}/h$ up to 600°C, then up to $750\,^{\circ C}/h$ at $75\,^{\circ C}/h$. The cooling tale was divided in two part: a first constant cooling

(a)   (b)
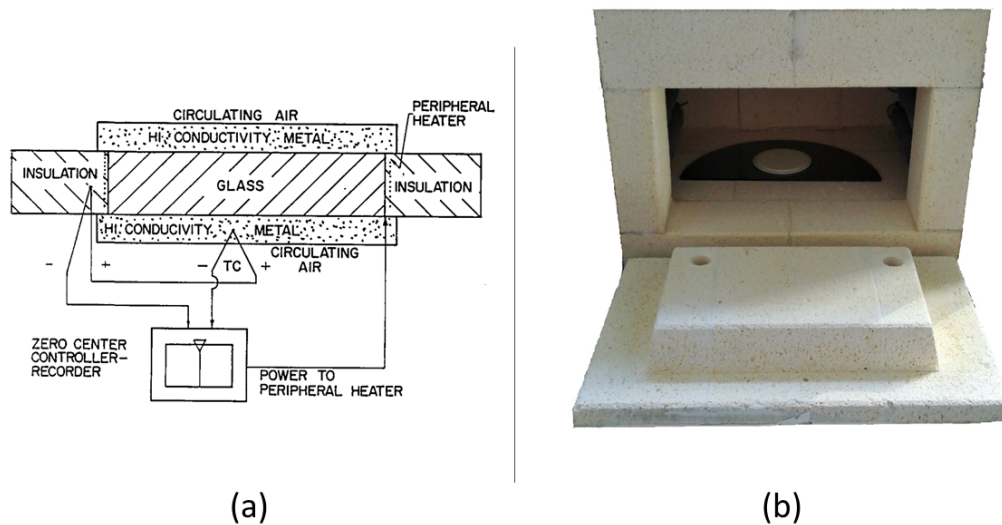
Figure 5.2: (a) Ideal heating set-up, as reported in [94]. (b) Our set-up implementation. The sample is placed between two slabs of silicon trying to bring about isothermal boundary conditions by virtue of the high thermal conductivity of the metal. A ceramic plate on top of the slab guarantee a uniform contact of the latter with the glass.

ramp brought the temperature down to $400°C$ at $-6°C/h$, the second one finally cool down the sample at $-20°C/h$ (Figure 5.5a).

5. A constant heating ramp at $100°C/h$ up to $600°C$, then up to $720°C/h$ at $75°C/h$ followed by a constant cooling ramp at $-12°C/h$, doubling the rate with respect to the first one to see is the process was still adiabatic (Figure 5.5b).

To test the routine, we implemented the interferometric device schematically reported in Figure 5.3a. It allowed us to test the effect of the annealing on the losses, the birefringence and the phase stability of the wave-guides. While for the first two aspect gave good and similar results, no one was satisfying on the phase-stability side. This problem can be faced by using thermal-phase shifter, as we have seen in Subsection 2.4.2.1. Therefore we decided to implement the last routine, being the less time consuming. Indeed this heating routine last about three days and it perfectly suites for a weekend processing of the sample.
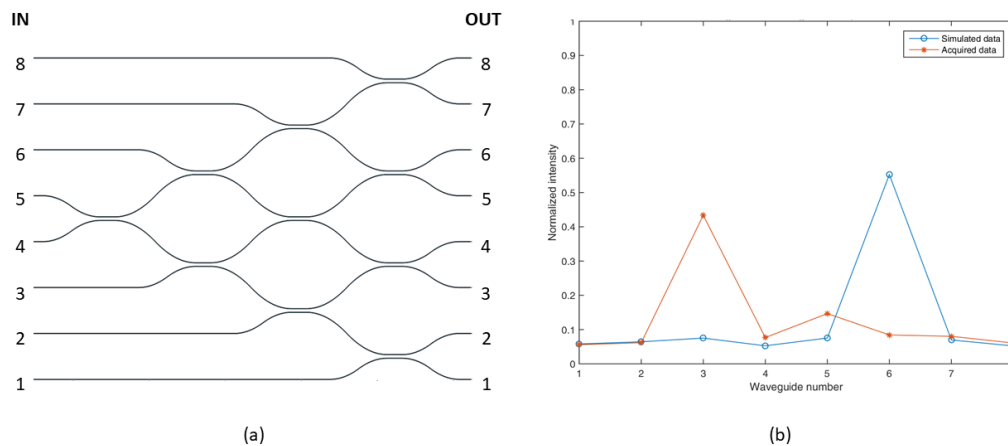
Figure 5.3: (a) A schematic representation of the interferometric device used to characterize the phase stability of th annelaing ruotine. (b) An example of the measure performed. A comparison between the theoretical and the real output intensity is performed. Via a multiparameter fit, the real phases are estimated in order to match the results.

5.1.2 Fabrication depth

The choice of the right depth is crucial in the fabrication process, and it is strictly related to the one of the microscope objective for the focusing of the laser beam. Thus we tried different solution:

1. a depth of $25\,\mu m$ using a 50x microscope objective. This value assure a good efficiency of the thermal phase shifters, being very close to the surface.

2. a depth of $25\,\mu m$ using a 20x microscope objective.

3. a depth of $170\,\mu m$ using a 50x microscope objective. This value was chosen accordingly to previous results obtained in the group.

Even tough the first two solution allowed the fabrication of valuable wave-guides, a main problem arised. Optically inspecting the fabricated device, we noticed that a lot of guides were interrupted. An example can be found in Figure 5.7. The reason has to be found in the proximity of the inscription depth to the surface: this make the fabrication very sensitive to dust, roughness and imperfection of the glass. This also implies a small repeatability of the fabrication process, so we had to continue with the fabrication at $170\,\mu m$. Indeed in this configuration this dependence on the surface was removed, giving at the same time results in line with the expectation.
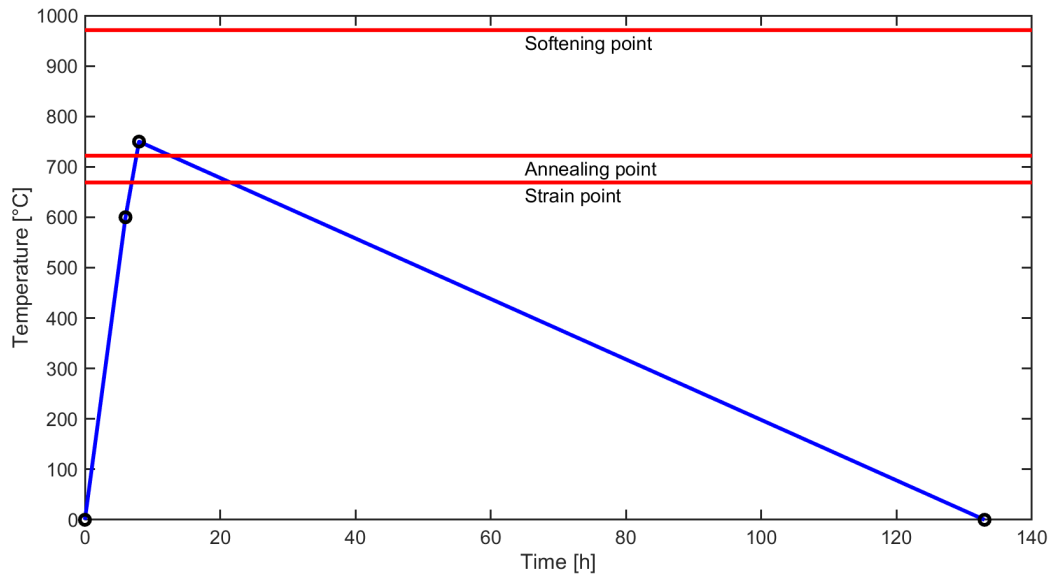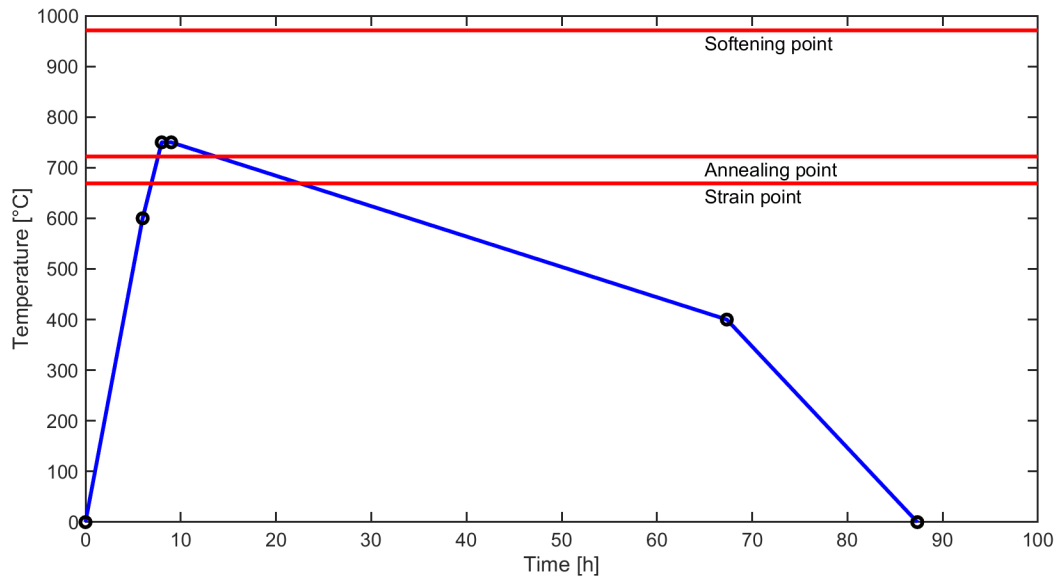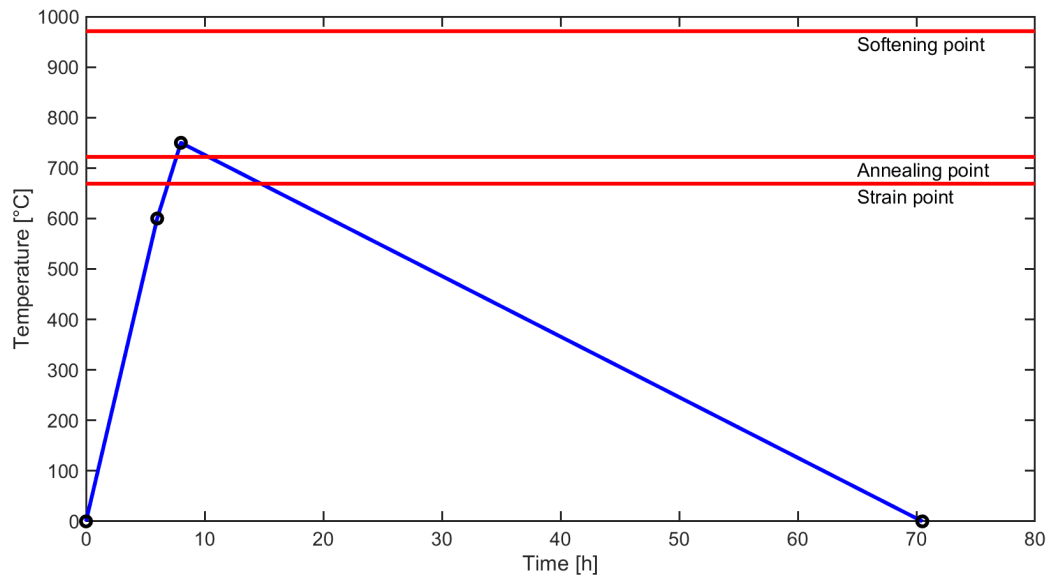
(a)
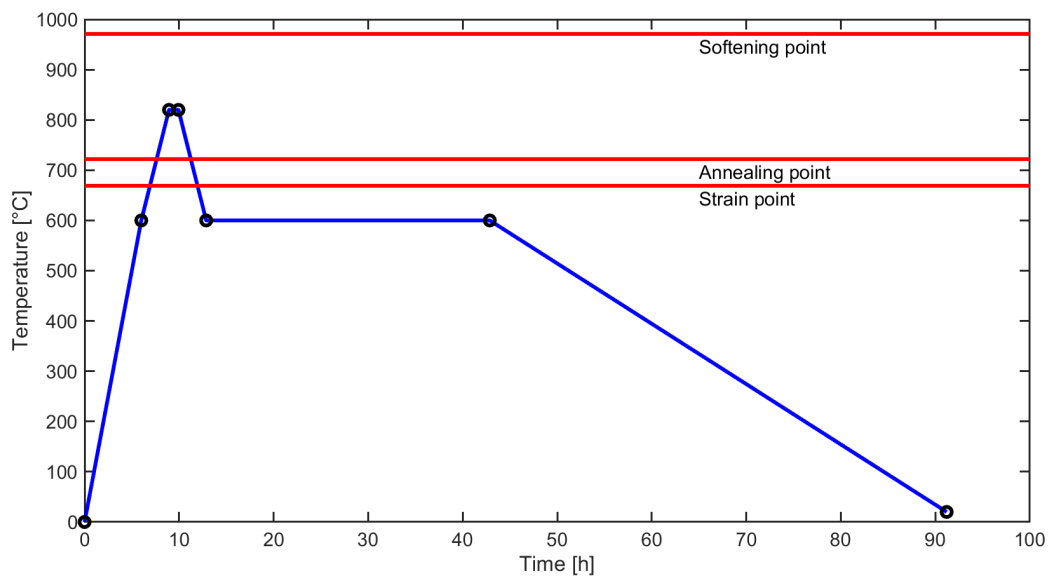
(b)

Figure 5.4: (a) Constant cooling rate routine, as proposed by Arriola et al. (b) Constant temperature soaking routine.

(a)

(b)

Figure 5.5: (a) Two-step constant cooling rate routine. We sped up the cooling rate once we were safely below the strain point of glass. (b) Compact cooling rate routine. With respect to Figure 5.4a, we are reducing the needed time from 5 to 3 days using a faster cooling rate (from $-6 \rightarrow -12\,^\circ$C).
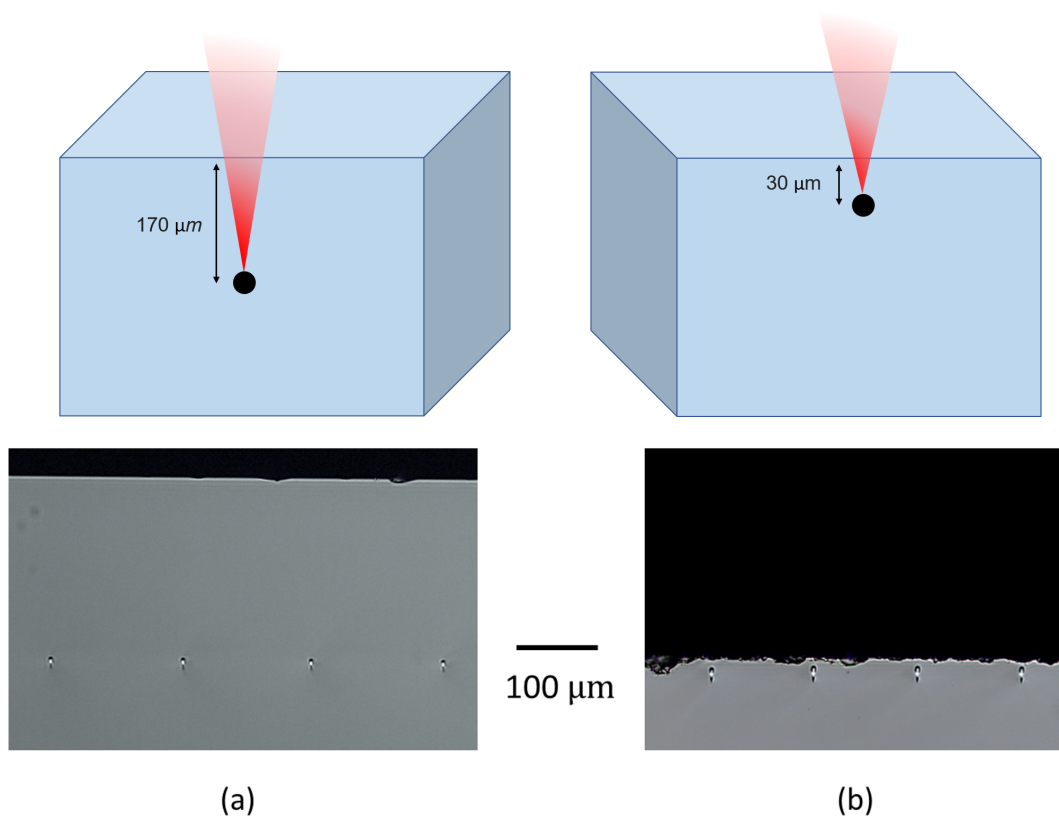
Figure 5.6: Input facet of the waveguides written at $170\,\mu m$ (a) and $25\,\mu m$ (b) using a 50x microscope objective.

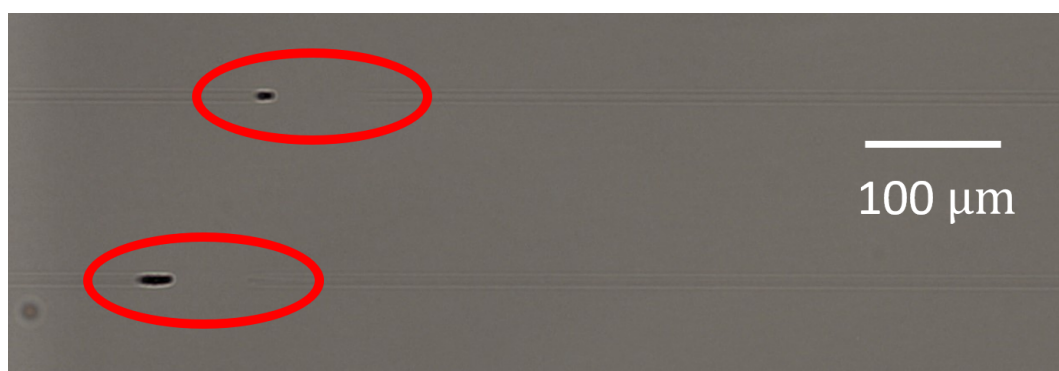

Figure 5.7: Waveguide interruptions in the fabrication at $20\,\mu m$ using a 20x microscope objective. These are probably due to the proximity of the inscription depth to the surface: this make the fabrication very sensitive to dust, roughness and imperfection of the glass.
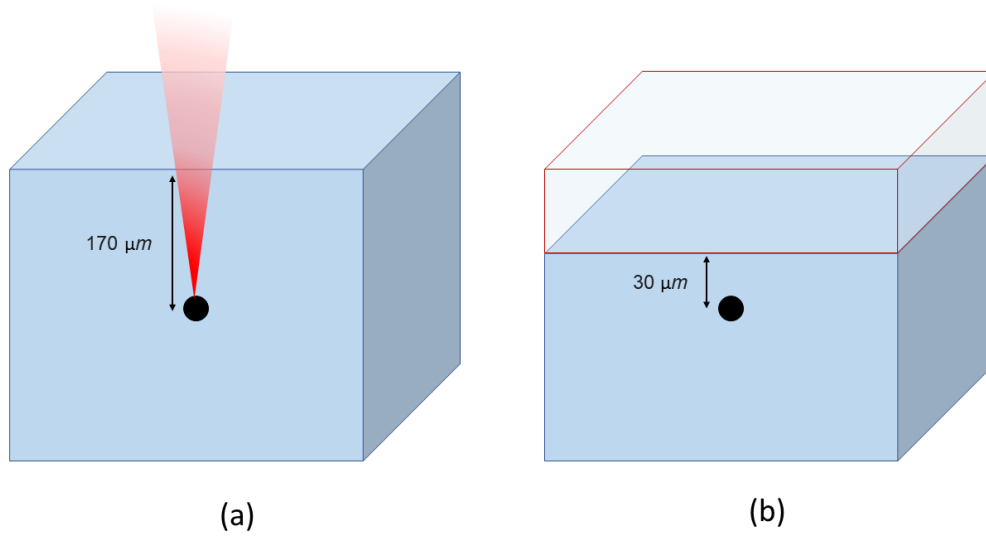
Figure 5.8: Deep written waveguides (a) show better performances, but reduce the effect of the microheater. In order to reduce their distance from the surface, we can perform a chemical etching after the fabrication process (b).

5.1.3 Chemical etching

The chosen depth imposes a minimum distance between the thermal phase shifters and the waveguide that would make their implementation useless. Thus, in order to maintain the benefits of the deep written waveguides, we can reduce their distance from the surface by a chemical etching after the fabrication (Figure 5.8). In order to do so, we put our sample in a bath of hydrofluoric acid. As glass consists predominantly of SiO_2, the etching reaction is based on breaking down the covalent bonds that silicon forms within the three-dimensional network:

$$SiO_2 + 4HF \rightarrow SiF_4 + 2H_2O \tag{5.1.1}$$
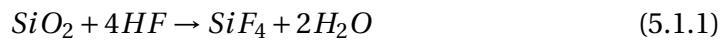
The reaction product SiF_4 evaporates. The added B_2O_3 groups in borosilicate glass form additional bonds with the silicon atoms that have to be broken down simultaneously [95], slowing the etching rate with respect to a fused silica glass. Being this process isotropic, the acid would have etched all the exposed surfaces of the glass, while we needed only a superficial etch. Thus we glued the sample to another glass, in order not to loose to much glass and so having fragile samples to manage. Moreover, irradiated glass has a higher etching rate with respect to the standard glass [96], so we need to cover the the input and output faces of the device to preserve them or at least to slow down the process. To do that, we cover

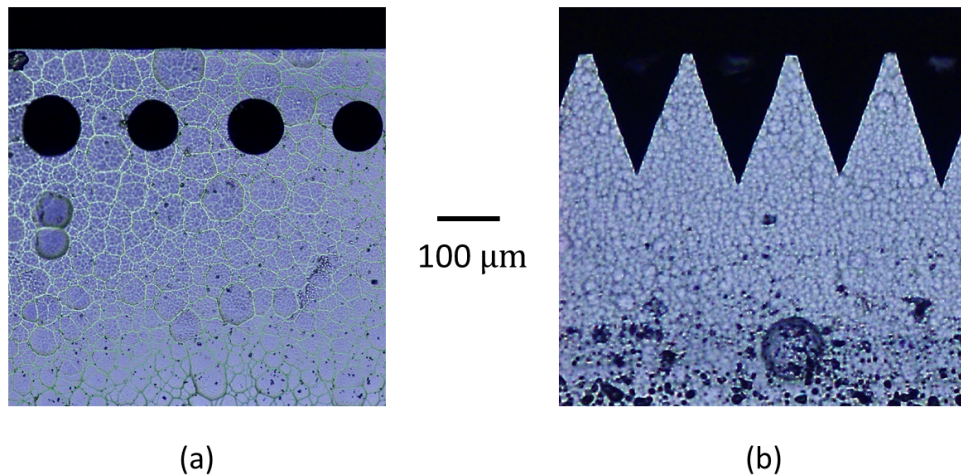(a)   (b)

Figure 5.9: Effects of chemical etching effect on the device. Lateral (a) and top (b) view are showed after bath of 2 hours in a solution of HF with concentration of 10% at 22 °C. The acid penetrated the irradiated waveguides glass up to 200 μm (b).

the input and output facet with ceramic paste. In any case the HF penetrates the protection, etching also some on the input and output region of the waveguides. This problem can be easily tackled by polishing the sample, as we said in Section 3.2.1. The effect on the guides is shown in Figure 5.9, while the device preparation is shown in Figure 5.10. After some etching test with other devices, we ended up with a stable recipe: we measured an etching rate of $\approx 0.7 \mu m / \text{min}$ at 22° C with an HF concentration of 10%.

5.1.4 Irradiation parameters

There are numerous parameters in femtosecond laser waveguide inscription to set and optimize for each different substrate and application. A first requirement is that the waveguides should support a single mode at the wavelength of this experiment (780 nm). Furthermore, of particular importance for all integrated quantum photonic experiments are low losses figures and good matching of the mode supported by the waveguides with the spatial profile of the mode carried by the input optical fibers (coupling losses).

Having fixed the writing wavelength at 1030 nm and the repetition rate at 1 MHz, corresponding to an intermediate regime between the single-pulse modification and the thermal accumulation regimes, we fabricated different guides varying the number of scan (5 $\longleftrightarrow$ 8), the writing speed (10 $\longleftrightarrow$ 40 mm/s), the laser power (between 195 $\longleftrightarrow$ 360 mW). By means of a powermeter we were
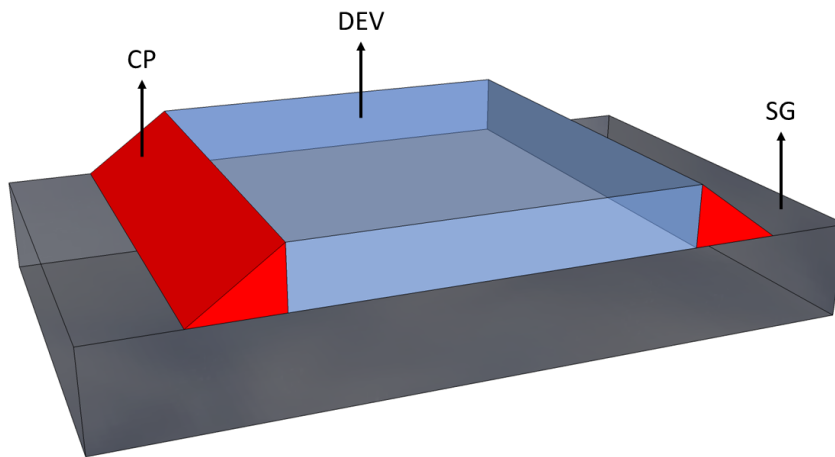
Figure 5.10: Sample preparation for the etching process. The device (DEV) is put on top of a support glass (SG) in order to preserve the lower surface of the glass. Input and output facet are protected by a ceramic paste that act also as glue between the two glasses.

able to characterize the insertion losses, while a mode inspection was performed through a CCD camera. The best guide resulted as a combination of 5 scan, a writing speed of $40\,mm/s$, showing propagation losses of 0.47 dB/cm. Once the irradiation parameters were chosen, we characterized the bending losses. In order to do that we wrote different S-bans, which are waveguides whose profile follow two symmetrical circular arcs, with a variable radius of curvature, connected to follow a 'S' shaped profile (Figure 5.11a). The total length of the waveguides was kept fixed, while the radius of the bends was changed from device to device. A straight waveguide was also fabricated in the same sample, in order to drop the propagation and coupling loss contributions from the measured losses. The measured bending losses as a function of the curvature radius are reported in Figure 5.11b. We decided to use a curvature radii of 30 mm, being the corresponding bending losses of just 0.35 dB/cm. In this way we were able to have shorter S-band and thus reducing the losses due to the propagation. The optimized fabrication and irradiation parameters are synthesized in Table 5.2.

5.2 Design of the integrated quarter

5.2.1 Geometrical layout

To implement the quarter introduced in Chapter 4, different solution are possible. One is to implement a direct coupling between the four modes, as pro-
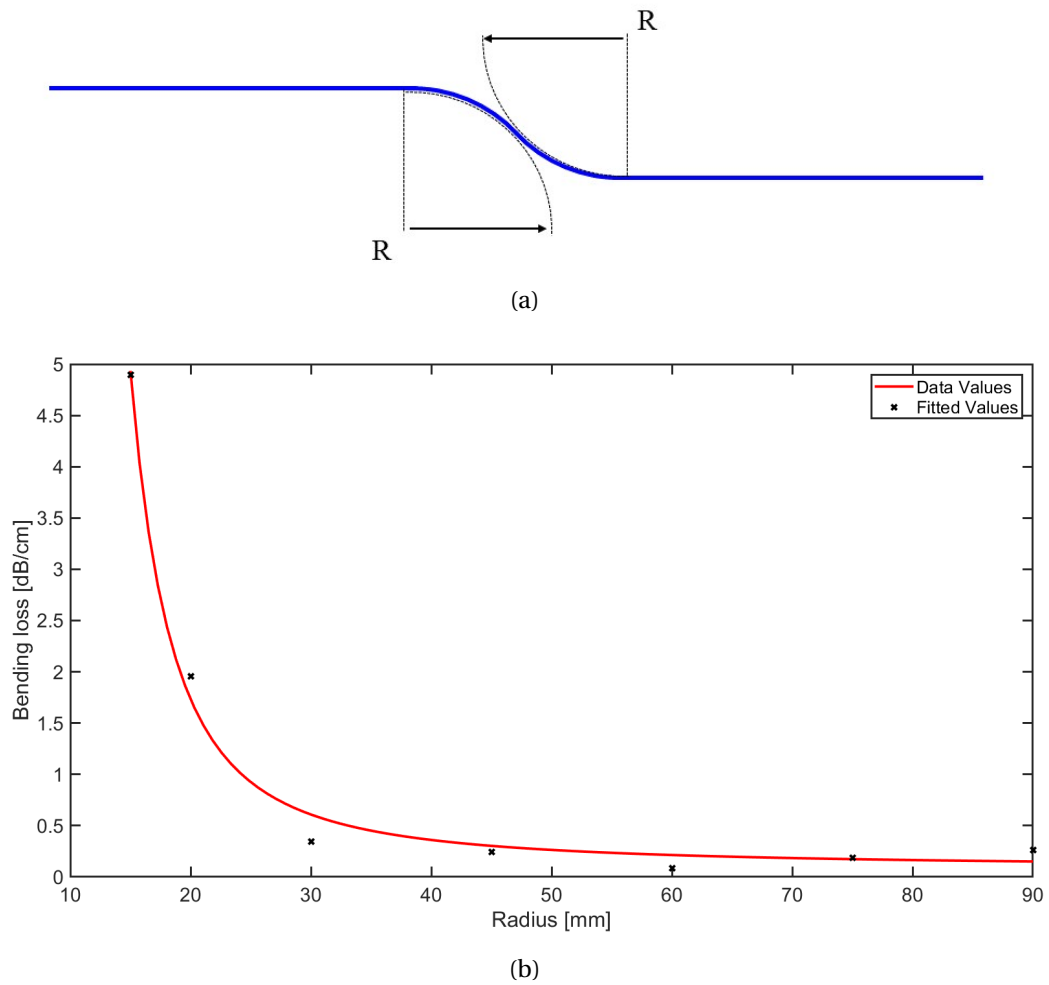
(a)

(b)

Figure 5.11: (a) Schematic of the S-band used to characterize the bending losses. (b) Analysis of the bending losses. Data taken by fiber-butt coupling with the sample are fitted via an exponential function, as already discussed in Section 5.11b.

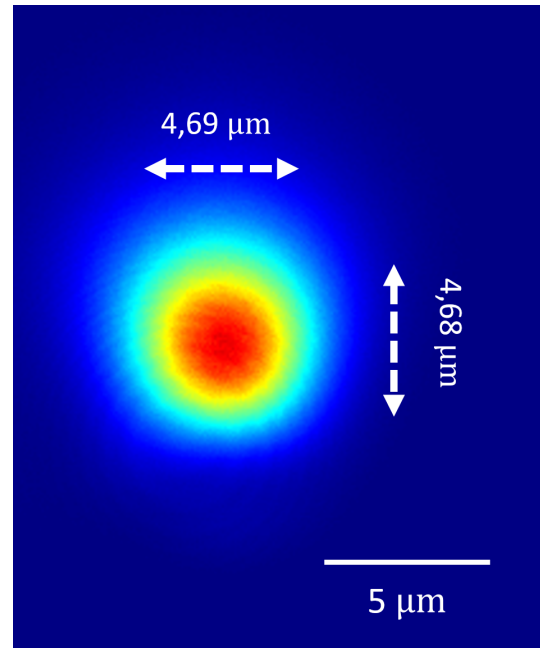| Substrate	Eagle XG
Laser system	Yb:KYW cavity dumped
Wavelength	1030 nm
Repetiotion rate	1 MHz
Objective	50x, 0.6 NA
Depth	170 μm
Number of scan	5
Writing power	270 mW
Writing speed	40 mm/s
Propagation losses	0.47 dB/cm
Bending losses	0.35 dB/cm (@30mm)

Table 5.2: Fabrication and irradiation parameters and associated parameters of the best guide. An image of the waveguide mode is reported.

posed in the work of Spagnolo et al. [93] and reported in Figure 5.12. We decided to follow a different path, coupling modes just by means of simple DCs. Thus our quarter will be composed by four directional couplers and a waveguide crossing, as in Figure 5.13. The unitary matrix describing this configuration is the same as Equation 4.2.2, as we show in Appendix 6.4.2. Without considering the latter, the four waveguides are design to have the same optical path, i.e. to induce the same phase shift. The complete interferometer is composed by two of these quarter, together with a straight waveguide part in between of the two. This part will be necessary for the implementation of the thermal phase shifter acting on the four
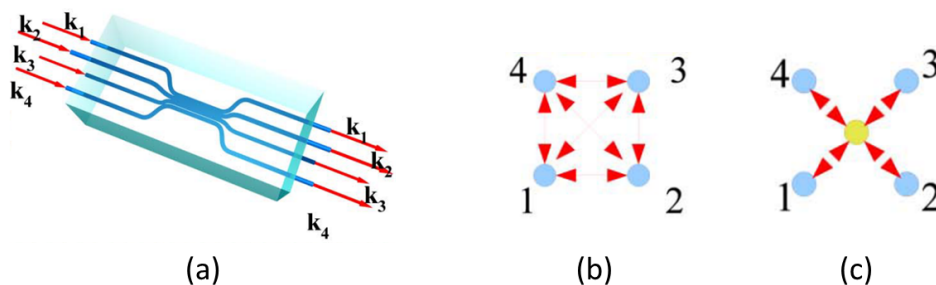

(a) (b) (c)

Figure 5.12: (a) 3-dimensional structure of quarter. (b) Geometry showing the direct coupling between the four modes of the quarter. (c) Indirect coupling between the four modes of the quarter by means of one ancillary mode.
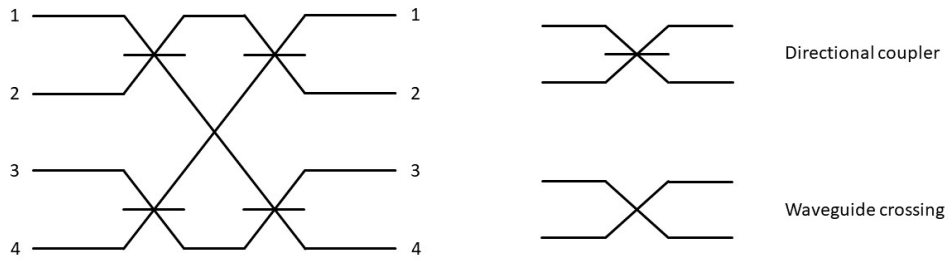
Figure 5.13: Schematic of our quarter implementation.
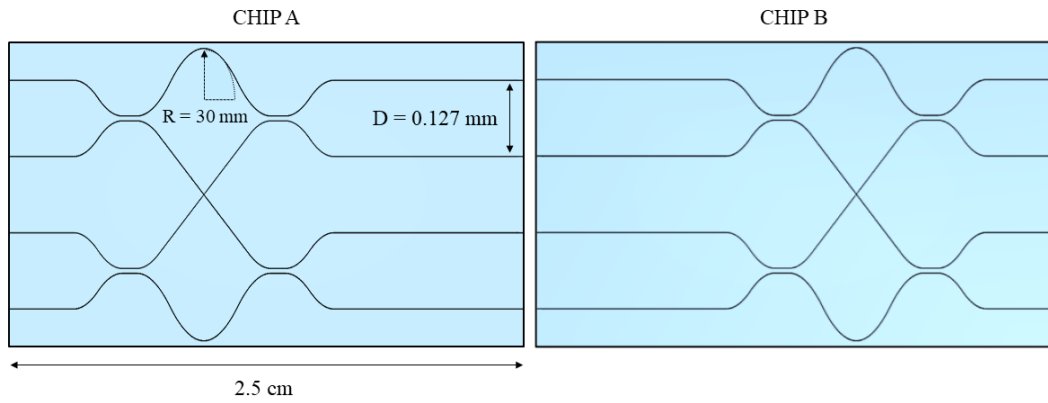
Figure 5.14: Schematics of the final chip. In order to be able to characterize the behaviour of the DCs, we need to split the device in two different chip of 2.5 x 2.5 cm each.

modes. However, in order to be able to fully characterize the behaviour of the DCs, we need to have access to the modes after each quarter. The final device will be then composed by two different chip of 2.5 x 2.5 cm each. A schematic of the complete device is reported in Figure 5.14. The input and output waveguides are spaced by $127\,\mu m$, in order to make the device compatible with a common fiber array.

5.2.2 Directional couplers

Being the directional coupler the basic element of the optical design reported in Section 5.17, a precise characterization of it's behavior was mandatory. As seen in Section 2.4.1, power splitting in DC is achieved by means of evanescent coupling. Developing the coupled mode theory, is easy to see that in the case of identical propagation constants in the two waveguides, the reflectance and transmittance are given by

$$R = \cos^2(\kappa L + \Phi) \qquad T = \sin^2(\kappa L + \Phi) \tag{5.2.1}$$

in which κ is the coupling coefficient, typically modeled as $\propto e^{-d}$, L is the interaction length and Φ represents the power exchange in the limit $L \to 0$ and is due to evanescent coupling in the curved sections preceding and following the interaction region. This behavior led to a trade-off in the choice of the parameters: the shorter the interaction distance, the shorter will be $L_{1/2}$ (i.e. the lowest interaction length required to have a balanced power splitting at the output ports, $R = T = 50$), but if d is too small, the process of writing the second waveguide could influence or damage the first, introducing a difference in the propagation constants or leading to an imbalance in the propagation losses. We studied the behavior of various directional couplers, fabricated with the optimized parameters found previously varying the interaction distance d between $8 \longleftrightarrow 10 \, \mu m$ as and we scanned L within the range of $0.35 \longleftrightarrow 1.2$ mm. The analyzed reflectances are reported in Figure 5.15b, showing a very good agreement with Equation 5.2.1. From the data, we find out that for $d = 8 \, \mu m$ for $L \approx 0.85$ mm we are able to fabricate balanced DC.

5.2.3 Waveguide crossing

The waveguide crossing is implemented by exploiting the 3-dimensional capability of the FLM technique. One of the two guide crossing is slightly curved towards the bottom, creating a bridge. In order to find the right relative depth of this structure, we fabricated several waveguide crossing spanning this parameter from 5 to 35 μm with a step of 5 μm. Since in any of the tested device we noticed a coupling between the modes of the crossing waveguides, probably due to a mismatch in the propagation constant induced by the depth variation, we selected the middle value of 20 μm. Indeed, being the length fixed to fit in the chip, it corresponds to a radius of curvature of 117 mm. From the previous analysis of the radius of curvature, the associated losses are negligible.

5.3 Device fabrication and characterization

5.3.1 Fabrication

Even if we had yet optimized the coupling parameters, the coupling coefficient κ is very sensitive on writing power fluctuations [97], and fabrication tolerances imply that optical properties cannot be perfectly reproduced with the same geometrical parameters between different fabrication runs. This issue was tack-

(a)

(b)
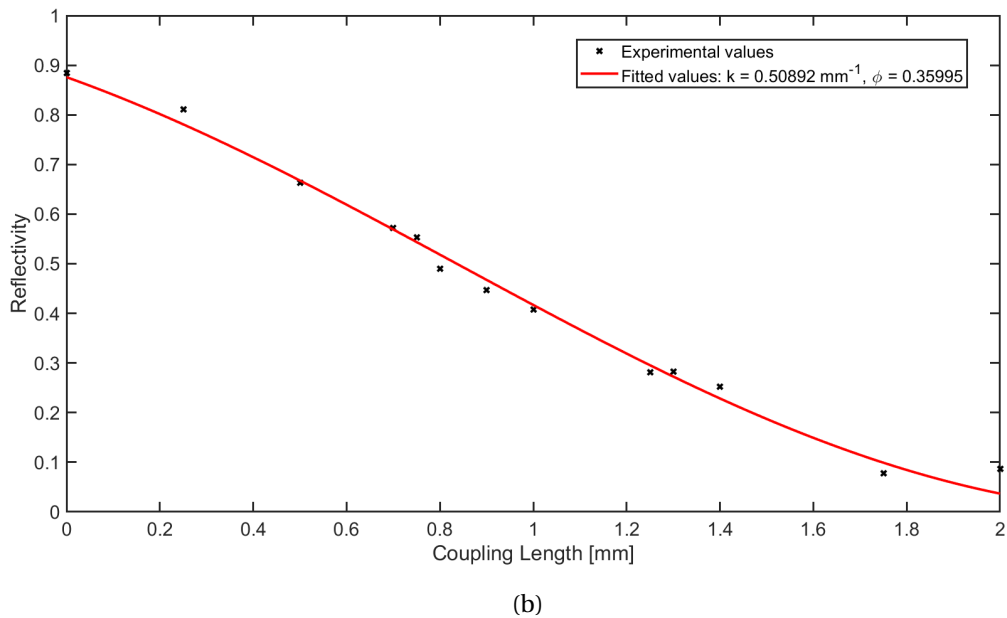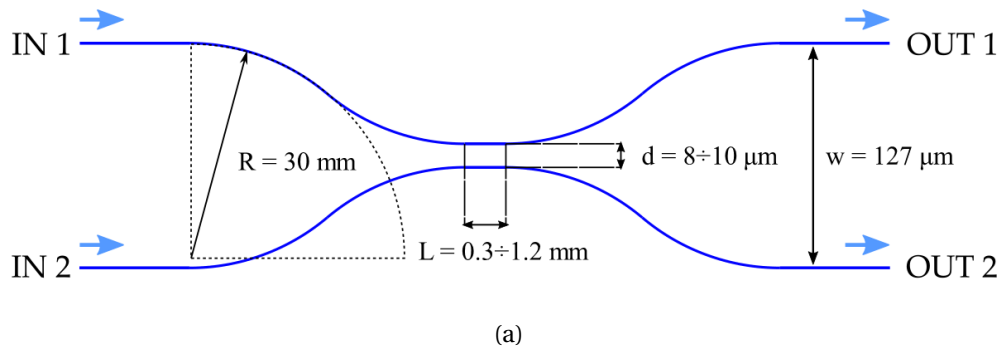
Figure 5.15: (a) Schematic layout of the directional coupler design. R is the radius of curvature of the bent waveguide sections, w is the distance between input (output) ports, d and L are the interaction distance and length of the region where evanescent coupling takes place. The geometrical values chosen for the preliminary studies are reported. (b) Analysis of the reflectance of the device at coupling distance $d = 8\,\mu m$ when varying the coupling length L. A sinusoidal fit, referring to Equation 5.2.1, is also shown.
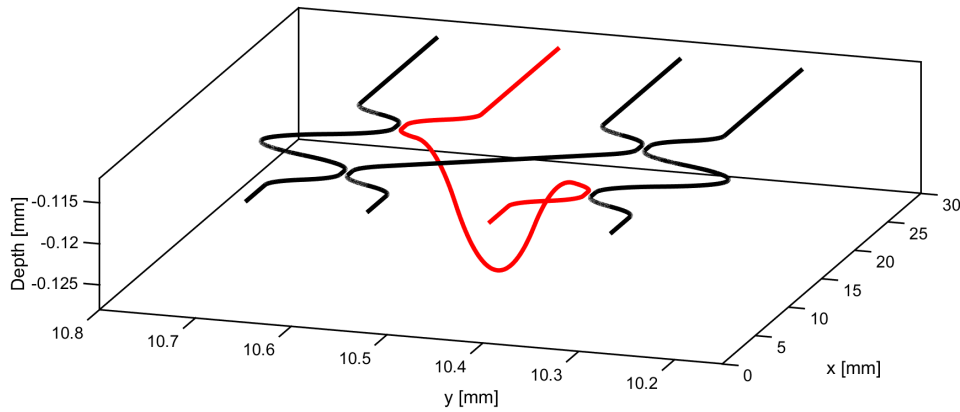
Figure 5.16: 3D projection of the chip scheme in order to show the waveguide crossing geometry.

led by keeping *d* and *R* fixed for the subsequent fabrications and writing several copies of the integrated optical circuits with a set of different values of *L* (eighteen per chip). This was sufficient to compensate for the drifts and noise affecting the fabrication setup, and, in our case, to obtain almost balanced directional couplers in the different sessions. Other than the optical circuits, we needed also to prepare the chip for the successive fabrication steps: the chemical etching and the micro-heaters design. For the former process, we added two waveguides at a depth of $140\,\mu m$ from the surface (so $30\,\mu m$ higher than the rest of the circuit). In this way, during the etching process, we would have known when to stop being $30\,\mu m$ the goal distance from the micro-heaters we wanted to obtain. For the latter process, we needed to leave some free space on top of witch some pin will be glued in order to externally command the resistances. Furthermore, to precisely align the resistors patter with the optical circuit beneath in the second fabrication stage, markers on the surface of the device had been included. The scheme of the fabrication for both chips is reported in Figure 5.17. Once fabricated, the chips were annealed and etched as described in the above sections. A polishing of the input and output facet with an abrasive disk was performed.

5.3.2 Characterization

In order to characterize the reflectivity of the DC, we coupled classical light at $780\,nm$ in the device (as shown in Section 3.2.2), acquiring the signal of the four output guide for each input guide with a powermeter. Following the next protocol in which P_i is the output power measured for the i-th guide, we were
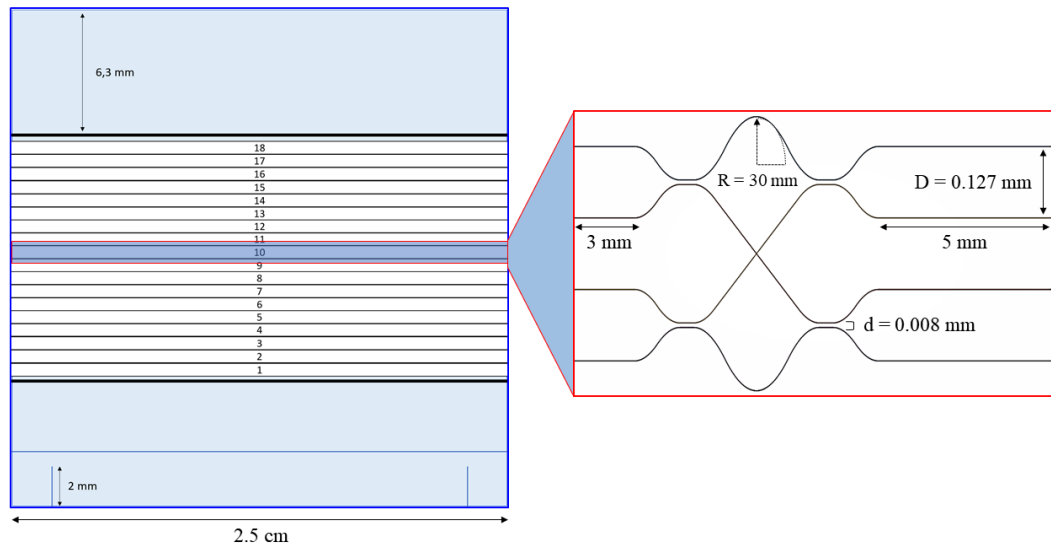
Figure 5.17: Fabrication design of the two chips. Eighteen copies of the same optical circuits, each varying the coupling length *L*, are fabricated. The black tick lines represents our reference guides, written 30 μm upon the rest of the circuit, to have a reference of the distances during the etching process. 6.3 mm of free space are needed for the connectorization of the resistor patter that will be produced afterwards. Ablation markers must be ablated on the surface in order to precisely allign the eletrical patter with the optical one. The distance *D* between the guides is choosen in order to make the device compatible with a fiber array.
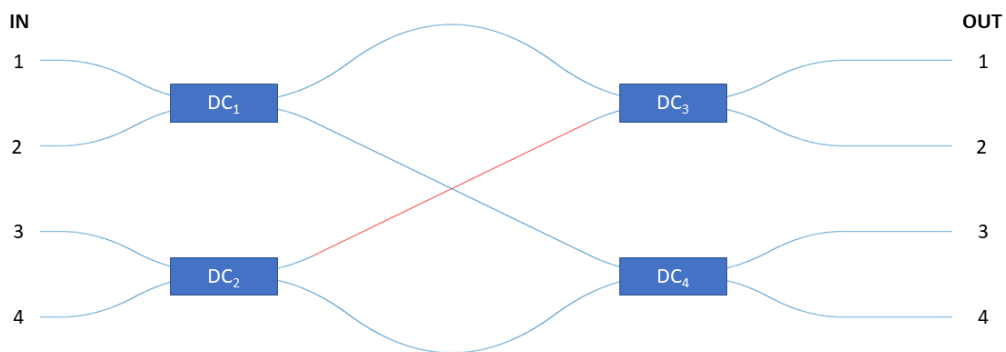
Figure 5.18: Schematic of the fabricated device numbering the DCs.

able to determine the reflectance R_j of the j-th directional coupler (as shown in Figure 5.18):

- Entering from IN_1

$$R_1 = \frac{P_1 + P_2}{P_1 + P_2 + P_3 + P_4} \qquad R_3 = \frac{P_1}{P_1 + P_2} \qquad R_4 = \frac{P_3}{P_3 + P_4} \tag{5.3.1}$$

- Entering from IN_2

$$R_1 = \frac{P_3 + P_4}{P_1 + P_2 + P_3 + P_4} \qquad R_3 = \frac{P_1}{P_1 + P_2} \qquad R_4 = \frac{P_3}{P_3 + P_4} \tag{5.3.2}$$

- Entering from IN_3

$$R_2 = \frac{P_1 + P_2}{P_1 + P_2 + P_3 + P_4} \qquad R_3 = \frac{P_2}{P_1 + P_2} \qquad R_4 = \frac{P_4}{P_3 + P_4} \tag{5.3.3}$$

- Entering from IN_4

$$R_3 = \frac{P_3 + P_4}{P_1 + P_2 + P_3 + P_4} \qquad R_3 = \frac{P_2}{P_1 + P_2} \qquad R_4 = \frac{P_4}{P_3 + P_4} \tag{5.3.4}$$

Taking the mean of the repeated measure, we obtained the data shown in Table 5.2.1. These values correspond to an average power division of 25% ± 0.16% among all possible input-output channels.

Chip	R_1	R_2	R_3	R_4
a	0.519	0.492	0.390	0.484
b	0.535	0.522	0.432	0.555

Table 5.3: Reflectances values of the DCs in the final devices.

We noticed that, in both the fabrication, the reflectivity of the third DC was lower with respect to the others. To see how this non ideality would affect the behaviour of the device, some numerical tests have been conducted. From now on, we will consider a device in which both internal phases (ϕ_1 and ϕ_2) and the interferometric phases (A, B and C) are null, so that we have a unique relation between an input and output guides (Equation 4.2.6).
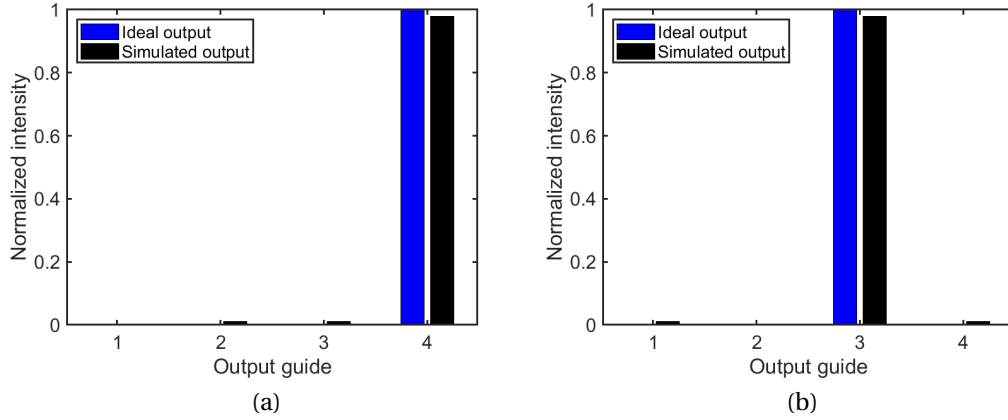
Figure 5.19: In order to understand what happens when we fabricated non ideal directional coupler, we made a comparison between the ideal behavior and the expected one. We selected the case in witch the reflectivity of the DC of the first chip were 0.4, while the one of the second were set to 0.6 (R_5 to R_8). Choosing the input guide, 1 for (a) and 2 for (b), we made the comparison showing just a small variation from the ideal result.

5.3.2.1 Parameters constrain

To understand these simulations, let's focus on a simple example. If on the first chip we were able to fabricate all the directional coupler with a splitting ratio of 30/70, while on the second we were able to reach a splitting ratio of 60/40, how much the ideal behavior of the device would change? Less than 1%. The results of the simulation are reported in Figure 5.19. To make a complete study on the robustness of the device in order to select a range of acceptable parameters, we performed the same simulation taking into account all the combination of the possible different splitting ratio in the range between 0.3 and 0.7. The results are shown in Figure 5.20a. Setting an acceptable range of splitting ratio between 0.4 and 0.6, we're able to improve drastically the quality of the output: once established a figure of merit as the contrast, defined as:

$$\Delta(i) = \frac{2 \cdot I_j - \sum_1^4 I_n}{\sum_1^4 I_n} \tag{5.3.5}$$

where I is the optical intensity, i is the input guide we're considering, j is the corresponding ideal output guide (that should be unique for a perfect device as we've seen in Subsection 4.2.3), we are able to guarantee a value of it greater than

0.84 as we can see from Figure 5.20b. This value corresponds to a 92 of agreement between the ideal and simulated values of intensity on the single guide. Since our results were well within these limitations, we were able to continue with the fabrication of the micro-heaters.
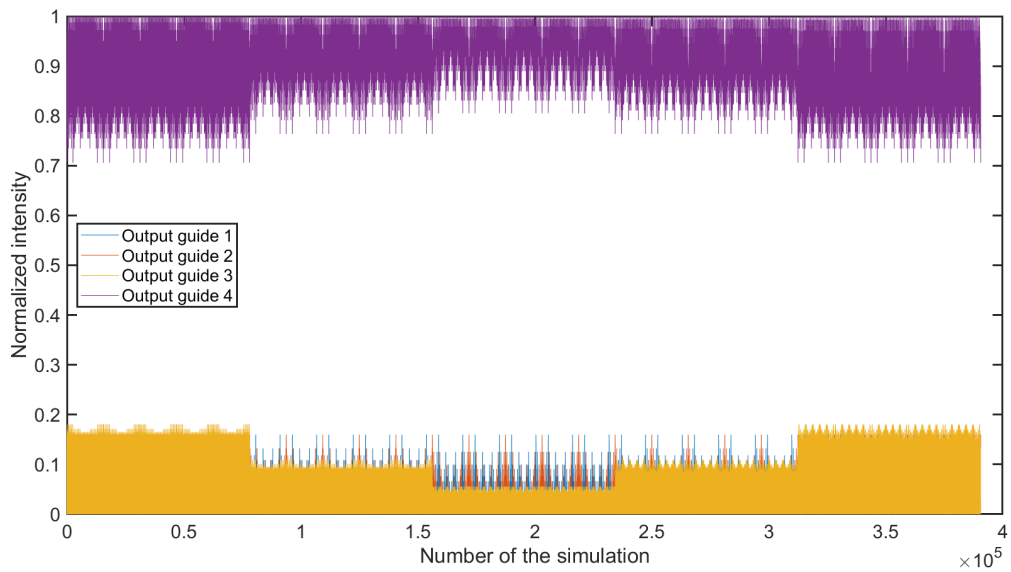
(a)
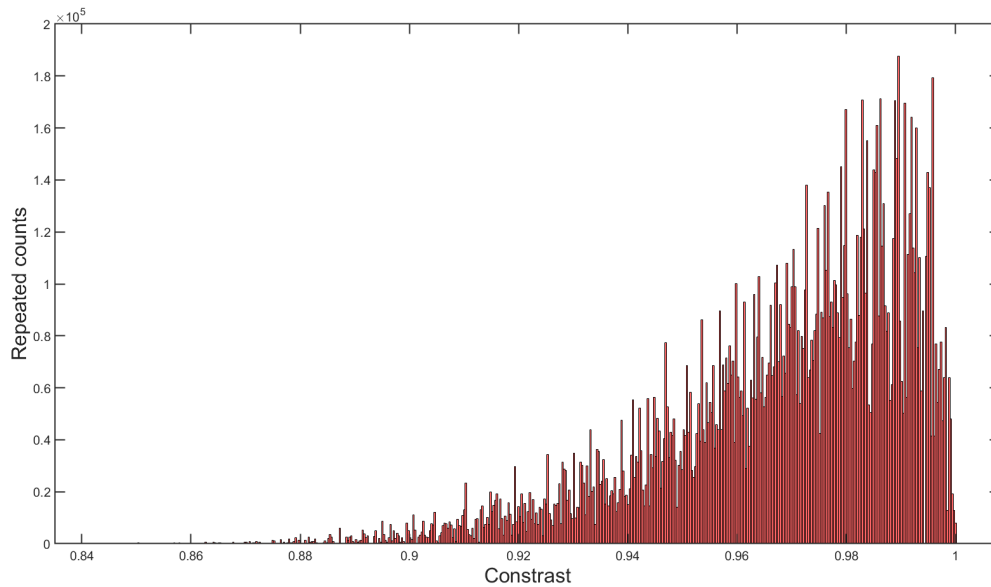
(b)

Figure 5.20: *(a)* In order to test the robustness of the device, we performed some simulation on the final device when the splitting ratio of the single directional coupler is not in the ideal situation of 50/50. To do that, we simulated the four output entering on the first guide when the splitting ratio of each directional coupler is varied between 0.3 and 0.7 with a step of 0.1. In the ideal case, entering from guide 1 we expect to exit only from guide 4: from the simulation we see that in the worst case the efficiency reaches the 70 %. *(b)* To further improve the quality of the fabricated device with respect to the results shown in Figure 5.20a, we tightened the limits of the splitting ratio to 0.4 ⟷ 0.7 (with a step of 0.02). In this way we were able to evaluate the contrast Δ entering from the first guide. In the histogram we reported, for each value of the constrast the corresponding counts are shown, such as the combination of splitting ratio that lead to that specific value of Δ. Within this shorter range, we're able to guarantee a constrast ≥ 0.84.

Achieving a high reconfigurability

6.1 Optimization of the micro-heaters

As already mentioned in Section 2.4.2.1, in order to have a reconfigurable optical circuit we need to fabricate micro-heaters to locally modify the refractive index of the waveguides. The fabrication process adopted previously by the group was based on the deposition of a single gold thin film on the glass substrate on which the waveguides are written. However, preliminary characterizations demonstrated that this approach leads to heaters showing important limitations. First of all, the values of the resistance undergoes to irreversible changes caused by the heating process. This can be seen in Figure 6.1, where we observed a drift in R of around 3.5% in just three hours of operation when injecting a power
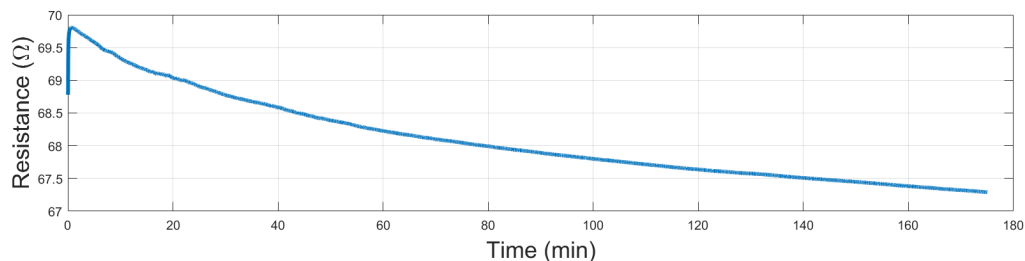

Figure 6.1: Poor resistance stability of a gold film, as in the previous recipe of the microheaters. We observed a drift in R of around 3.5% in just three hours of operation, when injecting a power of 500 mW.
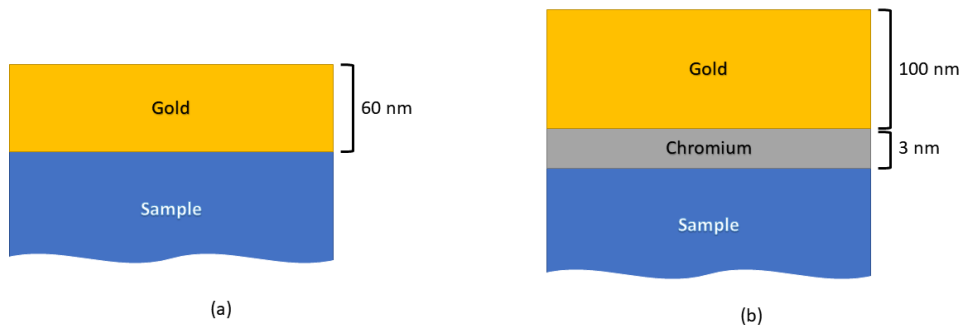
Figure 6.2: Schematic comparison between the old recipe (a) and the new one (b). In the latter, a thin film of chromium has been introduced in order to enhance the adhesion of gold. The figure in not in scale.

of $\approx$ 500 mW. This effect can be explained by a restructuring of the metal film caused by the high temperature reached during the heating. This is a major issue when performing the single photon measurement on active devices, since it implies the necessity to recalibrate the system every few hours. Secondly, the adhesion of the gold layer on the top of the glass substrate is particularly poor, and, for this reason, the layer is particularly fragile from the mechanical point of view, as verified by simple peel tests.

6.1.1 A new recipe

For this reasons, we developed a new recipe for the microheaters fabrication. First of all, we studied a method for improving the adhesion on glass. In order to do so, one could replace gold with chromium since the adhesion of the latter on glass is much higher. On the other hand, chromium is extremely prone to oxidation, making the connection of the resistors to the external power supply a critical task. So we moved to a different recipe, that exploits a chromium layer beneath the gold film (see Figure 6.2) as an adhesion layer [98]. More specifically, we decided to use a 3 nm layer of chromium and a 100 nm film of gold on it. This recipe guarantees good adhesion on glass, high mechanical stability and prevents the interdiffusion of chromium atoms inside the gold film during the heating, a side effect that would introduce a further cause of instability on the heater operation [99]. Finally, it is worth noting that the new design is electrically equivalent to the former one, since the very different resistivity of the two materials ($\rho_{Cr} = 13 \cdot 10^{-8}$, $\rho_{Au} = 2 \cdot 10^{-8}$) and the very different thickness of the two films make sure that the current will flow only on the gold layer.

Nevertheless, the issue concerning the operating stability still had to be faced,

by virtue of the fact that with this recipe R still drifted. For this reason we introduced a sample annealing step after the metal deposition. It consists of a rising ramp at 10 °C/min from room temperature to 500 °C , which is then kept constant for a time interval of 30 minutes. It is worth pointing out that, being the max temperature smaller than the strain point of the glass substrate (669 °C), this process has no effect on the optical properties of the waveguides. This annealing operation has the effect of inducing a complete metal structure relaxation, which reflects in the high stability of its resistance over time in subsequent operations. This improvement can be seen in Figure 6.3a: after a rapid initial thermal stabilization, corresponding to a resistance variation lower than 0.3 %, fluctuations remain lower than 0.05 % even after 8 hours of operation at 600 mW.

We also tested the performance at high dissipated power of the new resistors, in order to set an upper bond for a safe operation, namely without inducing permanent modifications or damages to the device. As shown in Figure 6.3b the heater can sustain a power dissipation up to 3.6 W, which is about four times larger than the breaking point achieved with the former recipe, for resistors of equal dimensions. Furthermore, the reliability of the micro-heaters was tested not only with an IV characterization, but also with stability measurements that demonstrated a correct operation up to many hours with similar dissipated powers. The IV curve reported in Figure 6.3b also shows the non linearity of the resistance at high temperature. For this reason, to monitor the injected power we needed to calculate it as $P = V \cdot I$ instead of the ohmic $P = {V^2}/{R}$, since we are injecting less power than what we expect.

6.1.2 Thermal cross-talk

In Equation 2.4.4 we have seen how the phase dependence on the dissipated power in a MZI is related to the ratio of the distances between its arms and the heater. It's clear that, if the heating is not localized on just one arm but reaches also the other one, the efficiency of the thermal phase shifter is reduced. This is the case when a thermal cross-talk between the two arms is present. Indeed, we would like to heat only one waveguide, but instead also the refractive index of the second arm is going to be influenced by the power dissipation. This cross-talk effect will affect even different phases in case of more complex circuits.

In order to reduce this problem we decided to remove the metal film between the two waveguides. This fact , schematically represented in Figure 6.4a by a simple lumped element model, should improve the thermal insulation between one
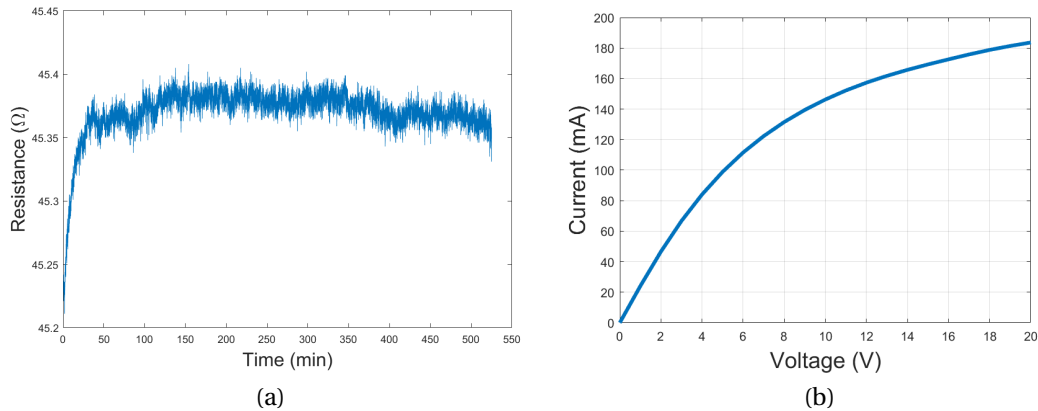
Figure 6.3: *(a)* Resistance value of the metal film after the annealing process. A high stability over time is achieved, with an instability of just 0.05 % even after 8 hours of operation at 600 mW. *(b)* Performance test at high dissipated power of the new resistors. The heater can sustain a power dissipation up to 3.6 W, which is about four times larger than the breaking point achieved with the former recipe, for resistors of equal dimensions.

heater and the waveguides that are distant from it. Indeed, in a MZI with arms separated by 127 μm, we were able to reduce the power dissipation required for a 2π phase shift of around 15%, from 480 mW to 400 mW. This result is shown in Figure 6.3a. To get a further improvement in the cross-talk reduction, one could dig some trenches between the two waveguides, as proposed by Chaboyer et al. [100]. This kind of solution, though, is not easily implementable in our fabrication process, so it will require further studies.

6.2 Design of the electrical circuit pattern

The number and the position of the micro-heaters had to be chosen accordingly to the degrees of freedom on the phases we needed to control for the experiment. On the one hand, we must have the possibility to change the internal phase of the quarter in order to set an arbitrary equivalence class of the transformation matrix of the quarter itself. Furthermore, we needed to control the four phases of the optical modes after the quarter, that will become the internal interferometric phases during multi-parameter estimation experiment. A schematic of the resistors pattern it showed in Figure 6.5. The design is symmetric along the selected optical circuit. Two thermal phase shifters are placed on the outer arms of the quarter, giving us the possibility to control the internal phase ϕ. Other four

(a)

(b)

(c)
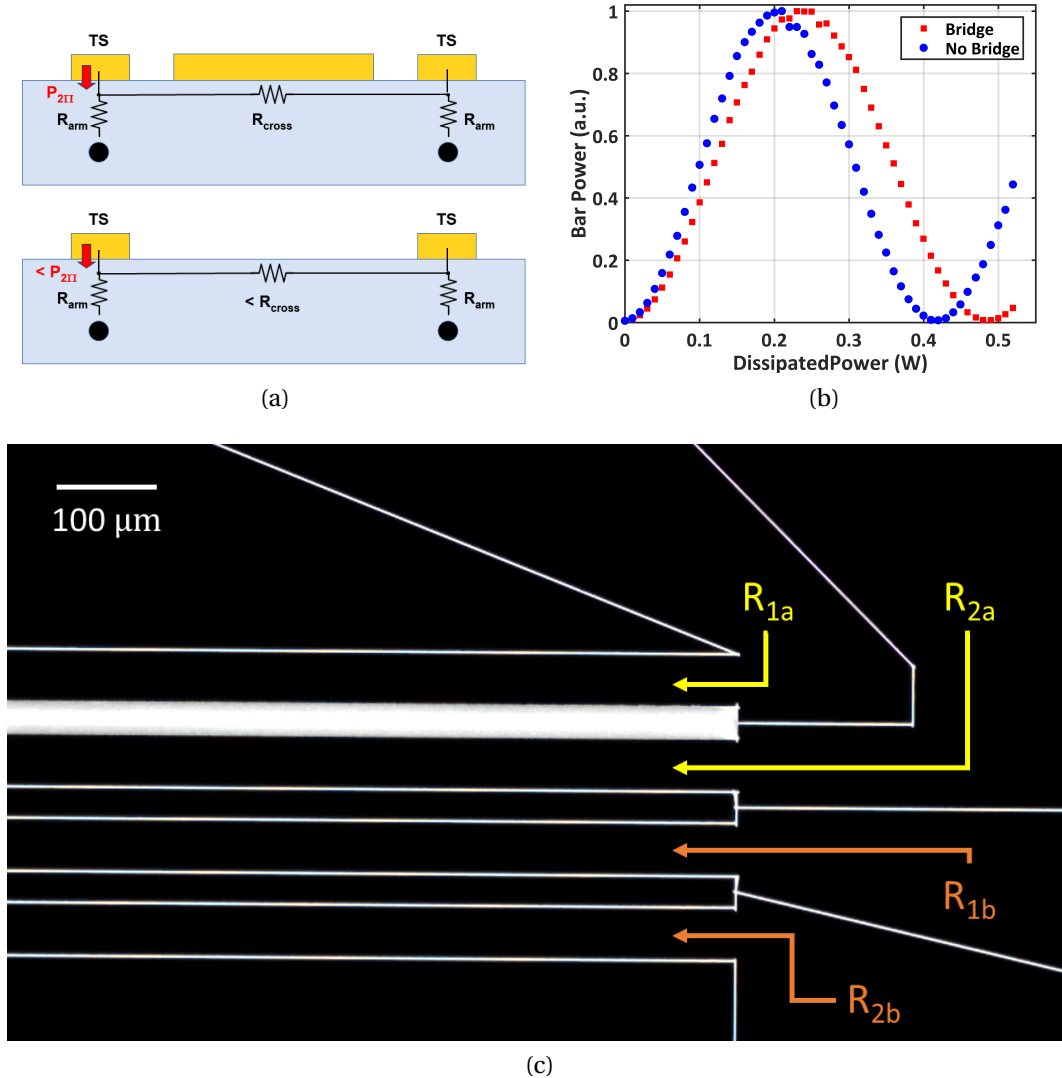
Figure 6.4: *(a)* Simple lumped element model to show the standard configuration (top), in which the golden bridge is still present between the phase-shifters (TS), and the novel configuration (bottom). By removing, at least in part, R_{cross}, we increase the efficacy of the TS on the MZI. *(b)* Comparison of the power dissipation that induces a 2π phase shift in a MZI with (blue) and without (orange) the metal bridge between the arms. A reduction of around 15%, from 480 mW to 400 mW, is reached. *(c)* Microscope image of the device used in the study. Between R_{1a} and R_{2a} the thermal bridge has been ablated, while between R_{1b} and R_{2b} it has been left.

Figure 6.5: Actual implementation of the thermal-phase shifters on the quarter chip. Two thermal phase shifter are placed on the inner arms of the quarter, giving us the 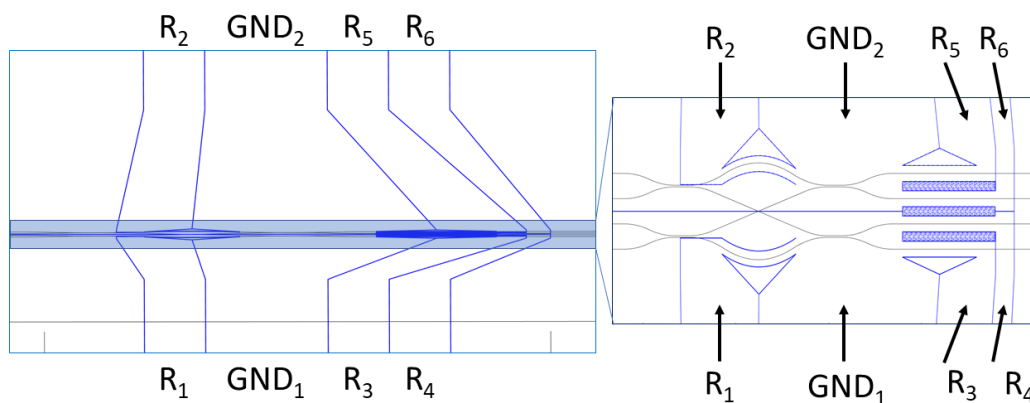possibility to control the internal phase ϕ. Other four thermal phase-shifter need to be placed on each arms of the device: together with the ones of the second half, this choice will produce eight phase shifter to actively select the internal phase of the interferometer. Note that, in the inset, H and V scales are different in order to highlight the optical circuit.

thermal phase-shifters are placed on each arm of the device. The upper and the lower part are electrically separated, so we have two different ground. The geometric parameters of the resistances have been chosen to have resistance values of about 50 Ω for the linear heater and about 70 Ω for the curved one.

6.3   Fabrication of the thermal phase shifter

The chromium-gold film was sputtered on the sample with a sputter coater (Cressington 108auto). A real-time measurement of the thickness was enabled by a thickness monitor (Cressington MTM-10), whose functioning is based on the dependence of the sample capacitance on the layer thickness. After the coating, the resistors were ablated with the same setup used for the inscription of the circuit. A precise alignment with respect to the waveguides was obtained by imaging with a CCD camera and exploiting the ablation lines fabricated during the waveguide inscription process, for restoring the same reference frame. Due to the etching process, these markers increased their width from 5 to 70 μm (Figure 6.6), slightly affecting the accuracy of the positioning which however remains > than 10 μm. For the resistors inscription, a 10x microscope objective and a power of 200 mW with a writing speed of 2 mm/s were used. The contours of the resistors were etched 5 times, with a 1.5 μm offset between every inscription to increase
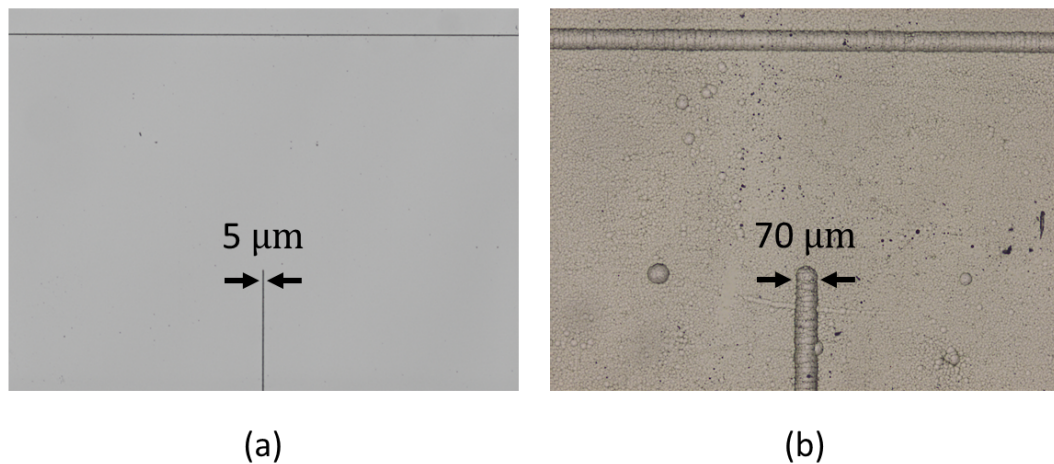
Figure 6.6: Ablated markers ($\approx 5\,\mu m$ of thickness) on top of the sample needed to align the resistors patter upon the optical circuits (a). In panel (b) the same image is taken after the etching process ($\approx 70\,\mu m$ of thickness).
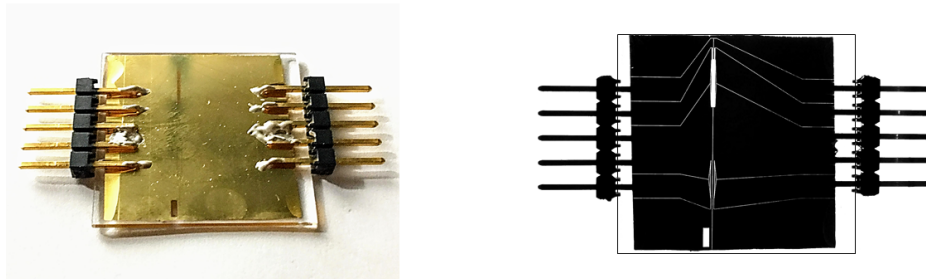
Figure 6.7: Photos of the final chip. The ablated windows on the bottom left was introduced in order to check the alignment between the waveguide and resistor frame.

their width. In this way, 3 μm wide ablations were obtained. After the laser ablation, the chip was connected to standard pin headers with a 0.1 inch pitch, which were connected on top of the pads by an electrically conductive epoxy glue. We decided to dedicate four pins to the ground connections, two per side, in order to have some spare ones in case some of them did not work properly, and for the possibility to connect them in parallel to reduce the ground resistance, which can be a cause of non linearities. An image of the final chip is reported in Figure 6.7.

6.3.1 Resistors characterization

After their connections, we measured the resistances of the phase shifters, to verify that their values were similar to what we expected. The results are reported in Table 6.1. It is possible to notice that the values are generally in line with the

expectations.

Chip	$R_1\,[\Omega]$	$R_2\,[\Omega]$	$R_3\,[\Omega]$	$R_4\,[\Omega]$	$R_5\,[\Omega]$	$R_6\,[\Omega]$
a	80.1	81.2	42.2	44.5	45.1	39.1
b	73.5	74.3	50.9	54.4	55.4	48.1

Table 6.1: Value of resistances in the two chips.

6.4 Calibration of the phase shifters

6.4.1 Far field interference

In order to find the dependence of the induced phase on the applied voltage, a calibration of the resistors was needed, consisting in applying an increasing voltage to every shifter, and then measuring the induced phase difference on the output guides. The problem is that any induced phase term does not influence the power distribution collected from the output ports (Equation 4.2.2). Thus we implemented a technique, similar to Young's experiment, to assess the operation of our six heaters. When light is coupled in one of the device inputs, the output ports acted as four point-like sources, spaced by $D = 127\,\mu m$, each of them emitting light with approximately the same amplitude, and a relative phase relations established by the phase shifters. The interference pattern generated in far field carries information about this phase difference relations. In fact, assuming to observe the far field interference fringes produced by N point-like sources, under the assumption of small angles of view with respect to the propagation direction, the intensity profile can be calculated as:

$$I \propto \sum_{i=0}^{N-1}\left(\sum_{k=j}^{N-1}\left(E_k E_{k-j}e^{i(\varphi_k-\varphi_{k-j})}\right)e^{i\left(2\pi j\frac{\omega}{\lambda L}y\right)}\right)+\text{c.c.} \qquad (6.4.1)$$

Here E_k is the real field amplitude of the k-th source, φ_k is its phase, y is the horizontal coordinate, on the imaging plane, and c.c. identifies the complex conjugate of the sum. $I(y)$ is therefore a finite Fourier series, with the contribution of $N-1$ different spatial frequencies, $f_j = j\frac{\omega}{\lambda L}$. Each Fourier coefficient is determined by the amplitude and phase of all the point sources separated by a distance $j\cdot\omega$. If only two such sources contribute to the interference pattern, the Fourier coefficient for f_j simplifies to $E_k E_{k-j}e^{i(\varphi_k-\varphi_{k-j})}$ and the phase difference between the two modes can be extracted as the phase of the Fourier peak, while

the heaters are driven. In general, the phase of the Fourier peak at the highest spacial frequency represents the phase difference between the most distant modes. This means that if we let interfere all four modes, the phase of the Fourier peak at the highest frequency, $f_3 = 3\frac{\omega}{\lambda L}$, will be $\varphi_4 - \varphi_1$. If now we block the output of the fourth guide, the phase of the Fourier peak at the highest frequency, $f_2 = 2\frac{\omega}{\lambda L}$, will be $\varphi_3 - \varphi_1$ and so on. Thus, fixing the phase of the 1st mode as a reference for the definition of each phase difference, we were able to fully reconstruct the matrix α describing the phase shifters.

6.4.2 Calculation of the α matrix

In Section 2.4.2.1 we have seen how we can model the effect of the microheaters on the intensity of the interference fringes. We can recast Equation 2.4.3 to highlight the phase dependence on the dissipated power as:

$$\phi \quad = \quad \phi_0 + \alpha P = \phi_0 + \alpha \frac{V^2}{R} \qquad (6.4.2)$$

where ϕ is the induced phase difference between two modes, P the dissipated power, V the applied voltage, R the resistance value and α the proportionality coefficient. Therefore, the Joule effect is more efficient for low resistances, since the same value of power is dissipated with a lower voltage. However, if the resistance is too low, then it becomes comparable to the one of the connections, so the heating is distributed and not localized on the waveguide. In the case of more phases to be controlled and more resistors, Equation 6.4.2 assumes a matricial form, since the effects of the resistors sum up linearly:

$$\boldsymbol{\phi} = \boldsymbol{\phi_0} + \underline{\boldsymbol{\alpha}} \boldsymbol{P} \qquad (6.4.3)$$

in which $\boldsymbol{\phi}$, $\boldsymbol{\phi_0}$ and $\boldsymbol{P}$ are vector, while $\underline{\boldsymbol{\alpha}}$ is a matrix. The experimental setup for this characterization method is portrayed schematically in Figure 6.8. A micrometric manipulator with a knife edge was positioned directly beyond the sample, in order to let interfere sequentially from 4 to 2 modes. Light was then propagated in free space for a distance L, where an image of the interference pattern was acquired with a CMOS camera. This spatial pattern was stored digitally and integrated along the vertical coordinate, which carried no information on the interference of the point sources. By employing a fast Fourier transform algorithm on the acquired profiles we obtained $N - 1$ peaks, where N is the number of in-
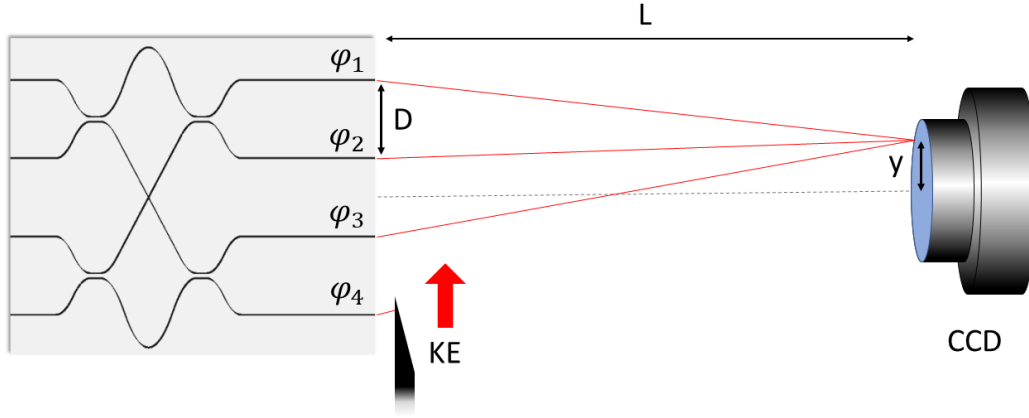
Figure 6.8: Experimental setup for the calibration of the phase shifters with the displacement of interference fringes. A knife edge (KE) is placed on a micrometric manipulator just at the end of the sample in order to cut, sequentially, modes 4 and 3,in order to allow the Fourier analysis of the fringe pattern. After the KE, light propagates in free space for a distance L, sufficient for the observation of far-field interference. There, an imaging camera (CCD) is positioned and the fringe pattern is acquired.

terfering modes. Focusing, for each N, on the peak at higher frequency, we were able to extract $\phi_{41} = \varphi_4 - \varphi_1$ with $N = 4$, ϕ_{31} with $N = 3$ (cutting the 4th mode) and ϕ_{21} with $N = 2$ (cutting also the 3rd mode). The value of these phases as a function of the power dissipated on each resistor follows a linear trend, with slopes that coincides with the elements of the matrix $\underline{\boldsymbol{\alpha}}$. Due to this, by performing a linear fit of the measured data, we could reconstruct the full matrix:

$$\begin{pmatrix} \phi_{21} \\ \phi_{31} \\ \phi_{41} \end{pmatrix} = \underbrace{\begin{pmatrix} 0.11 & -0.02 & -12.81 & 18.37 & 7.36 & 5.50 \\ -16.15 & 19.87 & -22.61 & 5.59 & 26.11 & 12.16 \\ -16.44 & 19.82 & -27.79 & -5.29 & 11.17 & 29.90 \end{pmatrix}}_{\boldsymbol{\alpha_a}} \boldsymbol{P} + \boldsymbol{\phi_0} \quad (6.4.4)$$

$$\begin{pmatrix} \phi_{21} \\ \phi_{31} \\ \phi_{41} \end{pmatrix} = \underbrace{\begin{pmatrix} 0.07 & 0.04 & -14.81 & 29.07 & 11.63 & 7.75 \\ -16.81 & 20.04 & -24.60 & 9.29 & 39.03 & 19.85 \\ -16.97 & 19.99 & -31.79 & -7.15 & 19.32 & 20.25 \end{pmatrix}}_{\boldsymbol{\alpha_b}} \boldsymbol{P} + \boldsymbol{\phi_0} \quad (6.4.5)$$

$\boldsymbol{\alpha_a}$ and $\boldsymbol{\alpha_b}$ are the α-matrices for the two chips. Each phase shifter allows to provide a full 2π modulation on its optical mode with a maximum power dissipation

of 500 mW. These results are well in line with the expected ones. An example of interference pattern analysis with the four mode interfering is reported in Figure 6.9.
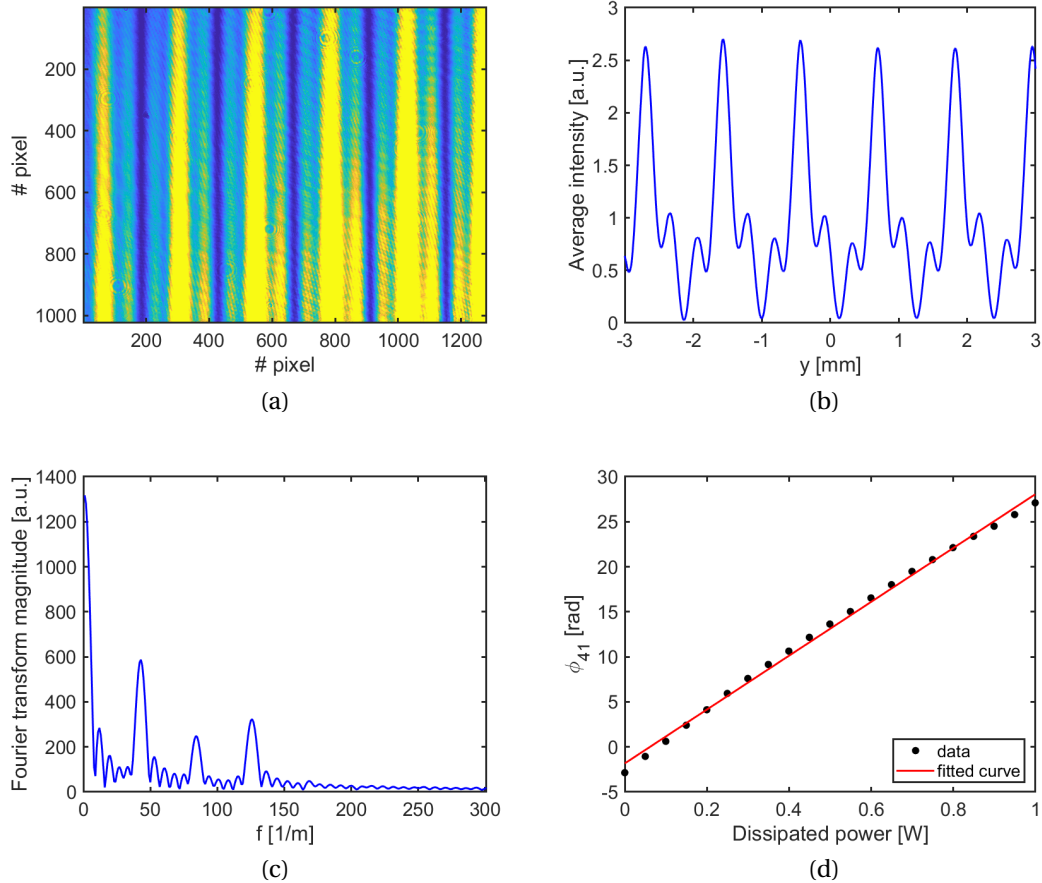
Figure 6.9: (a) Far-field fringe pattern obtained by interference of four modes on a CMOS camera. Integrating over the height, perpendicular to the line connecting the light sources, produces the oscillating function portrayed in (b). (c) The magnitude of the Fourier transformation of these function is reported. Three peaks are distinctly visible, corresponding to the three different spatial separation values between couples of sources. (d) Monitoring the phase of the Fourier transform at the higher spatial frequency, while the heaters dissipate different powers, allows to reconstruct their influence on $\phi_{41} = \varphi_4 - \varphi_1$ (i.e. a coefficient of the α matrix) by a linear fit of the acquired phase.

Conclusions and future perspectives

The design, the fabrication and the characterization with classical light of an integrated photonic device, which works as a four-modes interferometer was reported. The device is composed by the cascading of two 4x4 multi-port devices called quarters.

Thanks to the integration of several active phase shifters, it is possible to actively tune in a accurate way all the device internal phases. Such a device finds very important applications in the field of quantum metrology, and, in particular, for the implementation of super-resolved multi-parameters estimation algorithms. Experiments in this direction will be performed in the near future at Università La Sapienza, in Rome, employing the device described in this work once the two chip will be glued together.

The fabrication process consisted in fabricating deep waveguides in alumino-borosilicate glass by Femtosecond Laser Micromachining (FLM). A long thermal annealing process is then performed to release the mechanical stress that accumulates into the substrate during the writing process, achieving low propagation (0.4 $^{dB}/cm$) and bending (0.35 $^{dB}/cm$ at 30 mm) losses. A chemical etching is performed in order to make the waveguides close to the surface. Here, chromium-gold resistive heaters were patterned enabling the thermo-optic tuning of the internal phase and the four interconnection phases in the final tract of the quarter. These devices are among the most reconfigurable performing circuits realized by FLM up to date. In future, several kinds of experiments could be implemented thanks to the high possibility of tuning different phases which let to reach a great flexibility in the use of the device.
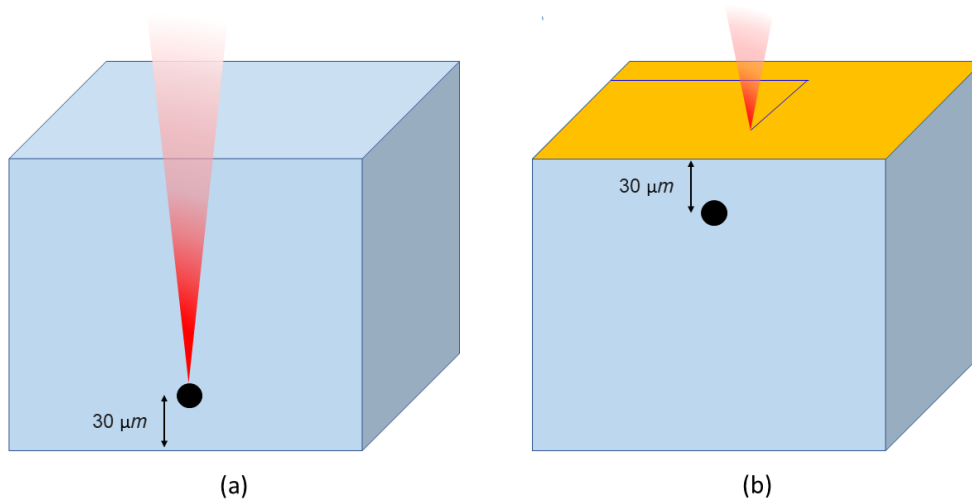
Figure 6.10: To avoid the etching process while writing deep buried waveguides, we can focus the laser beam near the bottom of the glass (a). In doing so, we just need to tilt the sample to be ready to fabricate the microheaters (b).

Future work will be devoted for the further optimization of the fabrication process. On the one hand, a complete investigation will be carried on in order to better understand and to reduce the fluctuations in splitting ratio of the directional couplers reported in Table 5.3. On the other, a different approach to the fabrication process will be studied. Indeed the presented process consists in three steps: the laser irradiation, the thermal annealing and the etching process. The last one is fundamental in order to achieve the reconfigurability with the microheaters placed on the surface. A different approach could be the one presented in Figure 6.10, in which the waveguides are fabricated near the bottom surface of the sample. In this «upside-down» approach, the benefits of the deep writing are preserved (i.e. low dependence on the surface condition) but no additional process is needed to make the waveguides close to the thermal-phase shifter. Moreover, this fabrication design is compatible with a water-assisted femtosecond laser pulse ablation technique [101]. This technique make usage of distilled water to enhance the femtosecond ablation rate significantly, placing the sample in the liquid and ablating the bottom surface. Mixing the two techniques, it would be possible to implement the dig of trenches in the glass to reduce the thermal cross talk, as anticipated in Section 6.1.2. A preliminary optimization of the fabrication and irradiation process has been carried out, in the same way we explained in Chapter 5. The results are synthesized in Table 6.2. We see that bending losses increase almost by a factor of 2 ($0.35 \rightarrow 0.66\,{}^{dB}/_{cm}$). This is mainly related to the wider extension of the waveguide mode. Furthermore,
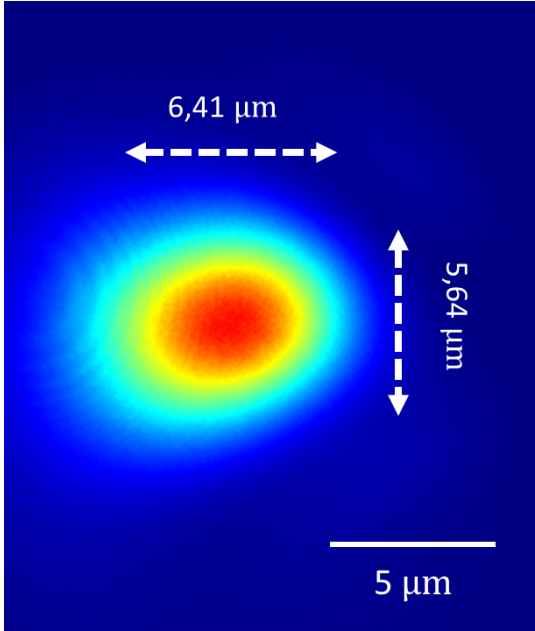
Substrate	Eagle XG
Laser system	Yb:KYW cavity dumped
Wavelength	1030 nm
Repetiotion rate	1 MHz
Objective	50x, 0.6 NA
Depth	-30 μm (from bottom)
Number of scan	5
Writing power	425 mW
Writing speed	20 mm/s
Propagation losses	0.35 dB/cm
Bending losses	0.66 dB/cm (@30mm)

Table 6.2: Fabrication and irradiation parameters and associated parameters of the best guide. An image of the waveguide mode is reported.

very deep waveguides turned out to be very sensitive to small depth variations, most probably because of the very pronounced aberration effects that take place during the laser writing. Indeed, during our study the inscription depth, we noticed a high variability dependence of the losses. Moreover, we could only get functioning waveguide at $-25\,\mu m$ from the bottom. Decreasing the distance, we were only able to ablate the glass, as reported in Figure 6.11, losing the possibility to guide light. Several solutions are yet available to face this depth-sensitivity. For example a compensation of the aberrations, due to the high depth, is possible with special objectives. A different solution could be the implementation of
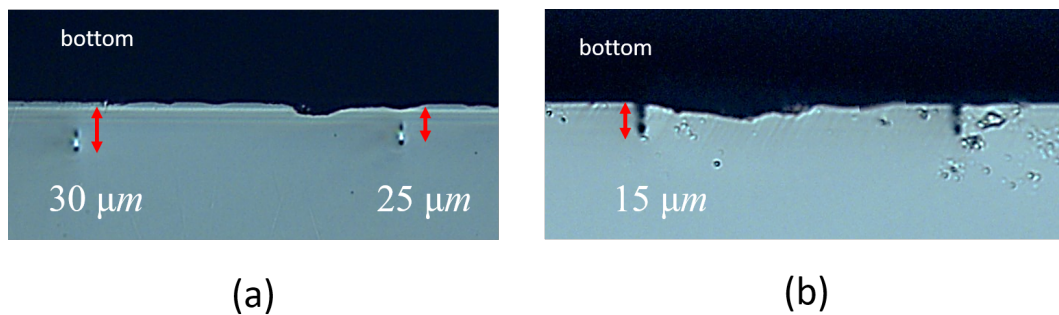
Figure 6.11: (a) Waveguides written in the «upside-down» configuration at different depth. (b) When we are too close to the bottom, we start ablating the glass, losing the possibility to guide light.

a spatial light modulator (SLM) to spatially varying the modulation of the laser beam inside the sample.

Ringraziamenti

Bibliography

[1] Bureau International des Poids et Mesures. Resolution 12 of the 11th CGPM, 1960.

[2] French College of Metrology. *Metrology in Industry:The Key for Quality*. ISTE, 2006.

[3] International Bureau of Weights and Measures. Convocation of the General Conference on Weights and Measures (25th meeting). Technical report.

[4] Sydney Schreppler, Nicolas Spethmann, Nathan Brahms, Thierry Botter, Maryrose Barrios, and Dan M. Stamper-Kurn. Optically measuring force near the standard quantum limit. *Science*, 2014.

[5] Tomohisa Nagata, Ryo Okamoto, Jeremy L. O'Brien, Keiji Sasaki, and Shigeki Takeuchi. Beating the standard quantum limit with four-entangled photons. *Science*, 316(5825):726–729, 2007.

[6] Vittorio Giovannetti, Seth Lloyd, and Lorenzo Maccone. Quantum-enhanced measurements: Beating the standard quantum limit. *Science*, 306(5700):1330–1336, 2004.

[7] C. W. Helstrom. Minimum mean-squared error of estimates in quantum statistics. *Physics Letters A*, 25(2):101–102, jul 1967.

[8] Marcin Zwierz and Pieter Kok. General optimality of the Heisenberg limit for quantum metrology. *Phys. Rev. Lett.*, 105(1):1–4, 2010.

[9] Sisi Zhou, Mengzhen Zhang, John Preskill, and Liang Jiang. Achieving the Heisenberg limit in quantum metrology using quantum error correction. *Nature Communications*, 9(1), 2018.

[10] R. Chaves, J. B. Brask, M. Markiewicz, J. Kołodyński, and A. Acín. Noisy metrology beyond the standard quantum limit. *Physical Review Letters*, 111(12), dec 2013.

[11] Martin B. Plenio and Susana F. Huelga. Sensing in the presence of an observed environment. *Physical Review A*, 93(3), oct 2016.

[12] Yuichiro Matsuzaki, Simon C. Benjamin, and Joseph Fitzsimons. Magnetic field sensing beyond the standard quantum limit under the effect of decoherence. *Physical Review A - Atomic, Molecular, and Optical Physics*, 84(1):012103, jul 2011.

[13] Vittorio Giovannetti, Seth Lloyd, and Lorenzo MacCone. Advances in Quantum Metrology. *Physical Review Letters*, 96(1):1–10, 2006.

[14] V B Braginsky, Y I Vorontsov, and K S Thorne. Quantum Nondemolition Measurements. *Science*, 209(4456):547–557, aug 1980.

[15] L Zehnder. *Ein neuer Interferenzrefraktor*. Springer, 1891.

[16] Christopher C. Gerry and Peter L. Night. Introductory Quantum Optics, 2005.

[17] P GRANGIER, G ROGER, and A Aspect. Experimental-Evidence For A Photon Anticorrelation Effect On A Beam Splitter - A New Light On Single-Photon Interferences. *Europhysics Letters*, 1986.

[18] C. K. Hong, Z. Y. Ou, and L. Mandel. Measurement of subpicosecond time intervals between two photons by interference. *Physical Review Letters*, 1987.

[19] J. J. Bollinger, Wayne M. Itano, D. J. Wineland, and D. J. Heinzen. Optimal frequency measurements with maximally correlated states. *Physical Review A - Atomic, Molecular, and Optical Physics*, 1996.

[20] Jonathan P. Dowling. Quantum optical metrology - The lowdown on high-N00N states. *Contemporary Physics*, 2008.

[21] Pieter Kok, Hwang Lee, and Jonathan P. Dowling. Creation of large-photon-number path entanglement conditioned on photodetection. *Physical Review A - Atomic, Molecular, and Optical Physics*, 2002.

[22] G. J. Pryde and A. G. White. Creation of maximally entangled photon-number states using optical fiber multiports. *Physical Review A - Atomic, Molecular, and Optical Physics*, 2003.

[23] Itai Afek, Oron Ambar, and Yaron Silberberg. High-NOON states by mixing quantum and classical light. *Science*, 2010.

[24] Albert Einstein. Die Grundlagen der allgemeinen Relativitätstheorie. *Annalen der Physik*, XLIX:769–822.

[25] Daisuke Nakane et al. Hidehiro Yonezawa. Quantum-Enhanced Optical-Phase Tracking. *Science*, 337(6101):1514–1517, 2012.

[26] M E Gertsenshtein and V. I Pustovoit. On the detection of low frequency gravitational waves. *Journal of Experimental and Theoretical Physics (U.S.S.R.)*, 43:605–607, 1962.

[27] B. P. et al Abbott. Observation of gravitational waves from a binary black hole merger. *Physical Review Letters*, 116(6), 2016.

[28] Popul Ar and Science Background. THE NOBEL PRIZE IN PHYSICS 2017 Cosmic chirps. (September 2015):1–8, 2017.

[29] Carlton M. Caves. Quantum-mechanical radiation-pressure fluctuations in an interferometer. *Physical Review Letters*, 45(2):75–79, 1980.

[30] J Et Al. Aasi. Enhanced sensitivity of the LIGO gravitational wave detector by using squeezed states of light. *Nature Photonics*, 7:613–619, 2013.

[31] Ulrich W. Rathe and Marlan O. Scully. Theoretical basis for a new subnatural spectroscopy via correlation interferometry. *Letters in Mathematical Physics*, 34(3):297–307, jul 1995.

[32] Agedi N. Boto, Pieter Kok, Daniel S. Abrams, Samuel L. Braunstein, Colin P. Williams, and Jonathan P. Dowling. Quantum Interferometric Optical Lithography: Exploiting Entanglement to Beat the Diffraction Limit. *Physical Review Letters*, 85(13):2733—-2736, sep 2000.

[33] Michael A. Taylor and Warwick P. Bowen. Quantum metrology and its application in biology, feb 2016.

[34] Peter A. Morris, Reuben S. Aspden, Jessica Bell, Robert W. Boyd, and Miles J. Padgett. Imaging with a small number of photons. *Nature Communications*, 6(1):5913, dec 2014.

[35] Magued B Nasr, Darryl P Goode, Nam Nguyen, Guoxin Rong, Linglu Yang, Björn M Reinhard, Bahaa E.A. Saleh, and Malvin C Teich. Quantum optical coherence tomography of a biological sample. *Optics Communications*, 282(6):1154–1159, 2009.

[36] Andrea Crespi, Mirko Lobino, Jonathan C. F. Matthews, Alberto Politi, Chris R. Neal, Roberta Ramponi, Roberto Osellame, and Jeremy L. O'Brien. Measuring protein concentration with entangled photons. *Applied Physics Letters*, 100(23), sep 2012.

[37] Michael A. Taylor, Jiri Janousek, Vincent Daria, Joachim Knittel, Boris Hage, Hans A. Bachor, and Warwick P. Bowen. Biological measurement beyond the quantum limit. *Nature Photonics*, 7(3):229–233, jun 2013.

[38] K. M. Davis, K. Miura, N. Sugimoto, and K. Hirao. Writing waveguides in glass with a femtosecond laser. *Optics Letters*, 21(21):1729, 1996.

[39] Feng Chen and J. R.Vázquez de Aldana. Optical waveguides in crystalline dielectric materials produced by femtosecond-laser micromachining, 2014.

[40] Arnaud Zoubir, Martin Richardson, Clara Rivero, A Schulte, Cedric Lopez, Kathleen Richardson, Nicolas Hô, and Réal Vallée. Direct femtosecond laser writing of waveguides in As2S3 thin films. *Optics Letters*, 2004.

[41] D. Liu, Y. Li, R. An, Y. Dou, H. Yang, and Q. Gong. Influence of focusing depth on the microfabrication of waveguides inside silica glass by femtosecond laser direct writing. *Applied Physics A: Materials Science and Processing*, 84(3):257–260, 2006.

[42] Kazuyoshi Itoh, Wataru Watanabe, Stefan Nolte, and Chris B. Schaffer. Ultrafast processes for bulk modification of transparent materials. *MRS Bulletin*, 31(8):620–625, 2006.

[43] R Ramponi, R Osellame, and G Cerullo. Femtosecond Laser Micromachining. *Springer*, 123:483, 2012.

[44] L. V. Keldysh. Ionization in the field of a strong electromagnetic wave. *Soviet Physics JETP*, 1965.

[45] Chris B Schaffer, André Brodeur, and Eric Mazur. Laser-induced breakdown and damage in bulk transparent materials induced by thightly focused femtosecond laser pulses. *Measurement Science and Technology*, 12:1784–1794, 2001.

[46] J. W. Chan, T. Huser, S. Risbud, and D. M. Krol. Structural changes in fused silica after exposure to focused femtosecond laser pulses. *Optics Letters*, 26(21):1726, 2001.

[47] K. Miura, Jianrong Qiu, H. Inouye, T. Mitsuyu, and K. Hirao. Photowritten optical waveguides in various glasses with ultrashort pulse laser. *Applied Physics Letters*, 71(23):3329–3331, 1997.

[48] Chris B. Schaffer, André Brodeur, José F. García, and Eric Mazur. Micromachining bulk glass by use of femtosecond laser pulses with nanojoule energy. *Optics Letters*, 26(2):93, 2001.

[49] Alexander M. Streltsov and Nicholas F. Borrelli. Study of femtosecond-laser-written waveguides in glasses. *Journal of the Optical Society of America B*, 19(10):2496, 2002.

[50] T. Toney Fernandez, P. Haro-González, B. Sotillo, M. Hernandez, D. Jaque, P. Fernandez, C. Domingo, J. Siegel, and J. Solis. Ion migration assisted inscription of high refractive index contrast waveguides by femtosecond laser pulses in phosphate glass. *Optics Letters*, 38(24):5248, 2013.

[51] Masaaki Sakakura, Masahiro Shimizu, Yasuhiko Shimotsuma, Kiyotaka Miura, and Kazuyuki Hirao. Temperature distribution and modification mechanism inside glass with heat accumulation during 250 kHz irradiation of femtosecond laser pulses. *Applied Physics Letters*, 93(23), 2008.

[52] L. Sudrie, M. Franco, B. Prade, and A. Mysyrowicz. Writing of permanent birefringent microlayers in bulk fused silica with femtosecond laser pulses. *Optics Communications*, 171(4):279–284, 1999.

[53] Yasuhiko Shimotsuma, Peter G. Kazansky, Jiarong Qiu, and Kazuoki Hirao. Self-organized nanogratings in glass irradiated by ultrashort light pulses. *Physical Review Letters*, 91(24):247405, dec 2003.

[54] E. N. Glezer, M. Milosavljevic, L. Huang, R. J. Finlay, T.-H. Her, J. P. Callan, and E. Mazur. Three-dimensional optical storage inside transparent materials. *Optics Letters*, 21(24):2023, 1996.

[55] S. Juodkazis, S. Matsuo, H. Misawa, V. Mizeikis, A. Marcinkevicius, H. B. Sun, Y. Tokuda, M. Takahashi, T. Yoko, and J. Nishii. Application of femtosecond laser pulses for microfabrication of transparent media. In *Applied Surface Science*, volume 197-198, pages 705–709, 2002.

[56] Giacomo Corrielli. *Integrated photonic circuits by femtosecond laser writing for qubit manipulation, quantum cryptography and quantum-optical analogies.* Phd thesis, Politecnico di Milano, 2015.

[57] Rafael R. Gattass and Eric Mazur. Femtosecond laser micromachining in transparent materials. *Nature Photonics*, 2(4):219–225, 2008.

[58] L. Huang at al. Aberration correction for direct laser written waveguides in a transverse geometry " Effect of refractive index-mismatch on laser microfabrication in silica glass. *Appl. Phys. A*, 24(10):257–260, 2016.

[59] Robert R. Thomson, Henry T. Bookey, Nicholas Psaila, Stuart Campbell, Derryck T. Reid, Shaoxiong Shen, Animesh Jha, and Ajoy K. Kar. Internal gain from an erbium-doped oxyfluoride-silicate glass waveguide fabricated using femtosecond waveguide inscription. *IEEE Photonics Technology Letters*, 18(14):1515–1517, 2006.

[60] S. Eaton et al. Heat accumulation effects in femtosecond laser-written waveguides with variable repetition rate. *Optics Express*, 13(12):4708, 2005.

[61] Shane Eaton. Contrasts in Thermal Dffusion and Heat Accumulation Effects in the Fabrication of Waveguides in Glasses using Variable Repetition Rate Femtosecond Laser. 2008.

[62] Shane M. Eaton, Haibin Zhang, Mi Li Ng, Jianzhao Li, Wei-Jen Chen, Stephen Ho, and Peter R. Herman. Transition from thermal diffusion to heat accumulation in high repetition rate femtosecond laser writing of buried optical waveguides. *Optics Express*, 16(13):9443, 2008.

[63] a.Q. Tool. Relaxation of stresses in annealing glass. *Journal of Research of the National Bureau of Standards*, 34(2):199, 1945.

[64] Werner Vogel. Glass Chemistry (1994). *Springer-Verlag Berlin Heidelberg*, 2:24–25.

[65] M. Rossi, O. Vidal, B. Wunder, and F. Renard. Influence of time, temperature, confining pressure and fluid content on the experimental compaction of spherical grains. *Tectonophysics*, 2007.

[66] Alexander Arriola, Simon Gross, Nemanja Jovanovic, Ned Charles, Peter G. Tuthill, Santiago M. Olaizola, Alexander Fuerbach, and Michael J. Withford. Low bend loss waveguides enable compact, efficient 3D photonic chips. *Optics Express*, 21(3):2978, 2013.

[67] Ned Charles, Nemanja Jovanovic, Simon Gross, Paul Stewart, Barnaby Norris, John O'Byrne, Jon S. Lawrence, Michael J. Withford, and Peter G. Tuthill. Design of optically path-length-matched, three-dimensional photonic circuits comprising uniquely routed waveguides. *Applied Optics*, 2012.

[68] Giacomo Corrielli, Simone Atzeni, Simone Piacentini, Ioannis Pitsios, Andrea Crespi, and Roberto Osellame. Symmetric polarization insensitive directional couplers fabricated by femtosecond laser waveguide writing. jan 2018.

[69] Graham D. Marshall, Robert J. Williams, Nemanja Jovanovic, M. J. Steel, and Michael J. Withford. Point-by-point written fiber-Bragg gratings and their application in complex grating designs. *Optics Express*, 18(19):19844, 2010.

[70] Martin Ams, Graham D. Marshall, Peter Dekker, James A. Piper, and Michael J. Withford. Ultrafast laser written active devices, 2009.

[71] Alexander M. Streltsov and Nicholas F. Borrelli. Fabrication and analysis of a directional coupler written in glass by nanojoule femtosecond laser pulses. *Optics Letters*, 26(1):42, 2001.

[72] Roberto Osellame, V Maselli, Nicola Chiodo, D Polli, R M Vazquez, R Ramponi, and Giulio Cerullo. Fabrication of 3D photonic devices at 1.55 mu

m wavelength by femtosecond Ti : Sapphire oscillator. *Electronics Letters*, 41(6):315–317, 2005.

[73] Shane M. Eaton, Wei Jen Chen, Haibin Zhang, Rajiv Iyer, Jianzhao Li, Mi Li Ng, Stephen Ho, J. Stewart Aitchison, and Peter R. Herman. Spectral loss characterization of femtosecond laser written waveguides in glass with application to demultiplexing of 1300 and 1550 nm wavelengths. *Journal of Lightwave Technology*, 27(9):1079–1085, 2009.

[74] W.-J. Chen, S. M. Eaton, H. Zhang, and P. R. Herman. Broadband directional couplers fabricated in bulk glass with high repetition rate femtosecond laser pulses. *Optics Express*, 16(15):11470–11480, 2008.

[75] M. Guillaume, L. A. Dunbar, Ch Santschi, E. Grenet, R. Eckert, O. J.F. Martin, and R. P. Stanley. Polarization sensitive silicon photodiodes using nanostructured metallic grids. *Applied Physics Letters*, 94(19), 2009.

[76] K Minoshima, A M Kowalevicz, E P Ippen, and J G Fujimoto. Fabrication of coupled mode photonic devices in glass by nonlinear femtosecond laser materials processing. *Optics Express*, 2002.

[77] Fulvio Flamini, Lorenzo Magrini, Adil S Rab, Nicolò Spagnolo, Vincenzo D'Ambrosio, Paolo Mataloni, Fabio Sciarrino, Tommaso Zandrini, Andrea Crespi, Roberta Ramponi, and Roberto Osellame. Thermally reconfigurable quantum photonic circuits at telecom wavelength by femtosecond laser micromachining. *Light: Science and Applications*, 4(11):354, 2015.

[78] Alexander Killi, Andy Steinmann, Jochen Dörring, Uwe Morgner, Max J. Lederer, Daniel Kopf, and Carsten Fallnich. High-peak-power pulses from a cavity-dumped Yb:KY(WO4)2 oscillator. *Optics Letters*, 30(14):1891, jul 2005.

[79] Jonas Söderholm, Gunnar Björk, Björn Hessmo, and Shuichiro Inoue. Quantum limits on phase-shift detection using multimode interferometers. *Physical Review A - Atomic, Molecular, and Optical Physics*, 2003.

[80] M. J. Holland and K. Burnett. Interferometric detection of optical phase shifts at the Heisenberg limit. *Physical Review Letters*, 1993.

[81] Mankei Tsang. Quantum imaging beyond the diffraction limit by optical centroid measurements. *Physical Review Letters*, 2009.

[82] L. M. Pham, D. Le Sage, P. L. Stanwix, T. K. Yeung, D. Glenn, A. Trifonov, P. Cappellaro, P. R. Hemmer, M. D. Lukin, H. Park, A. Yacoby, and R. L. Walsworth. Magnetic field imaging with nitrogen-vacancy ensembles. *New Journal of Physics*, 2011.

[83] Yuxiang Yang, Giulio Chiribella, and Masahito Hayashi. Attaining the ultimate precision limit in quantum state estimation. *arXiv preprint arXiv:1802.07587*, 2018.

[84] Carl W. Helstrom. Quantum detection and estimation theory, 1969.

[85] Sammy Ragy, Marcin Jarzyna, and Rafał Demkowicz-Dobrzański. Compatibility in multiparameter quantum metrology. *Physical Review A*, 2016.

[86] Peter C. Humphreys, Marco Barbieri, Animesh Datta, and Ian A. Walmsley. Quantum enhanced multiple phase estimation. *Physical Review Letters*, 111(7):1–10, 2013.

[87] Marek Z-dotukowski, Anton Zeilinger, and Michael A Horne. Realizable higher-dimensional two-particle entanglements via multiport beam splitters. *Physical Review A - Atomic, Molecular, and Optical Physics*, 55(4):2564–2579, 1997.

[88] Michael Reck, Anton Zeilinger, Herbert J. Bernstein, and Philip Bertani. Experimental realization of any discrete unitary operator. *Physical Review Letters*, 1994.

[89] Alberto Peruzzo, Anthony Laing, Alberto Politi, Terry Rudolph, and Jeremy L. O'Brien. Multimode quantum interference of photons in multiport integrated devices. *Nature Communications*, 2(1), 2011.

[90] Matteo G. A. Paris. Quantum estimation for quantum technology. pages 1–13, 2008.

[91] Jing Yang, Shengshi Pang, Yiyu Zhou, and Andrew N. Jordan. Optimal measurements for quantum multi-parameter estimation with general states. pages 1–17, 2018.

[92] Mario A. Ciampini, Nicolò Spagnolo, Chiara Vitelli, Luca Pezzè, Augusto Smerzi, and Fabio Sciarrino. Quantum-enhanced multiparameter estimation in multiarm interferometers. *Scientific Reports*, 6:1–8, 2016.

[93] Nicolò Spagnolo, Lorenzo Aparo, Chiara Vitelli, Andrea Crespi, Roberta Ramponi, Roberto Osellame, Paolo Mataloni, and Fabio Sciarrino. Quantum interferometry with three-dimensional geometry. *Scientific Reports*, 2(1):862, dec 2012.

[94] H E Hagy. Fine annealing of optical glass for low residual stress and refractive index homogeneity. *Applied optics*, 1968.

[95] G. A.C.M. Spierings. Wet chemical etching of silicate glasses in hydrofluoric acid based solutions, 1993.

[96] J. Blass, O. Köhler, M. Fingerle, C. Müller, and C. Ziegler. Properties and characteristics of wet (HF) and dry (RIE) etched borosilicate glass. *Physica Status Solidi (A) Applications and Materials Science*, 2013.

[97] Andrea Crespi. *Integrated optical circuits for biosensing and quantum information by femtosecond laser microfabrication*. Phd thesis, Politecnico di Milano, 2011.

[98] K. E. Haq, K. H. Behrndt, and Ilse Kobin. Adhesion Mechanism of Gold-Underlayer Film Combinations to Oxide Substrates. *Journal of Vacuum Science and Technology*, 1969.

[99] J. R. Rairden, C. A. Neugebauer, and R. A. Sigsbee. Interdiffusion in thin conductor films - chromium/gold, nickel/gold and chromium silicide/gold. *Metallurgical Transactions*, 1971.

[100] Zachary Chaboyer, A. Stokes, J. Downes, M. J. Steel, and Michael J. Withford. Design and fabrication of reconfigurable laser-written waveguide circuits. *Optics Express*, 2017.

[101] Xin Zhao and Yung C. Shin. Femtosecond laser drilling of high-aspect ratio microchannels in glass. *Applied Physics A: Materials Science and Processing*, 2011.

[102] Lucas B. Soldano and Erik C.M. Pennings. Optical Multi-Mode Interference Devices Based on Self-Imaging: Principles and Applications. *Journal of Lightwave Technology*, 1995.

As described in Section 5.2.1, our quarter is made up by four directional coupler and a waveguide crossing, as depicted in Figure 5.13. We can ideally divide the configuration in three part: two regarding the splitting part, one regarding the waveguide crossing. In the first case, the unitary matrix will be a simple combination of the balanced DC matrix seen in Equation 4.2.1:

$$
M_{\text{DCs}} = \frac{1}{\sqrt{2}} \begin{pmatrix} 1 & i & 0 & 0 \\ i & 1 & 0 & 0 \\ 0 & 0 & 1 & i \\ 0 & 0 & i & 1 \end{pmatrix} \tag{6.4.6}
$$

The wavecrossing part, ideally, just changes the 2nd and 3rd mode, so its unitary matrix will read

$$
M_{\text{cross}} = \begin{pmatrix} 1 & 0 & 0 & 0 \\ 0 & 0 & 1 & 0 \\ 0 & 1 & 0 & 0 \\ 0 & 0 & 0 & 1 \end{pmatrix} \tag{6.4.7}
$$

At the end we obtain

$$
M_{quarter} = M_{DCs} \cdot M_{bridge} \cdot M_{DCs}
$$

$$
= \frac{1}{2}
\begin{pmatrix}
1 & i & -1 & i \\
i & -1 & i & 1 \\
-1 & i & 1 & i \\
i & 1 & i & -1
\end{pmatrix}
\tag{6.4.8}
$$

Now, introducing some phase-shift at the input and output port, so without compromising the unitary transformation, we obtain:

$$
M'_{quarter} =
\begin{pmatrix}
-i & 0 & 0 & 0 \\
0 & 1 & 0 & 0 \\
0 & 0 & 1 & 0 \\
0 & 0 & 0 & i
\end{pmatrix}
M_{quarter}
\begin{pmatrix}
i & 0 & 0 & 0 \\
0 & 1 & 0 & 0 \\
0 & 0 & 1 & 0 \\
0 & 0 & 0 & -i
\end{pmatrix}
$$

$$
= \frac{1}{2}
\begin{pmatrix}
1 & 1 & 1 & 1 \\
-1 & -1 & 1 & 1 \\
-1 & 1 & -1 & 1 \\
1 & -1 & -1 & 1
\end{pmatrix}
\tag{6.4.9}
$$

that is Equation 4.2.2 in case of internal phase $\phi = 0$.

In the case of a MMI splitter, the value of the internal phase is, in principle, dictated by the self-imaging condition [102]. However, the presence of fabrication imperfections in the device would drive the multimode section away from exact self-imaging, and the relation between the optical phases would deviate from the expected value [89]. We can take into account these imperfection by introducing a phase term on each guide, as in Figure 6.12. Thus the unitary matrix
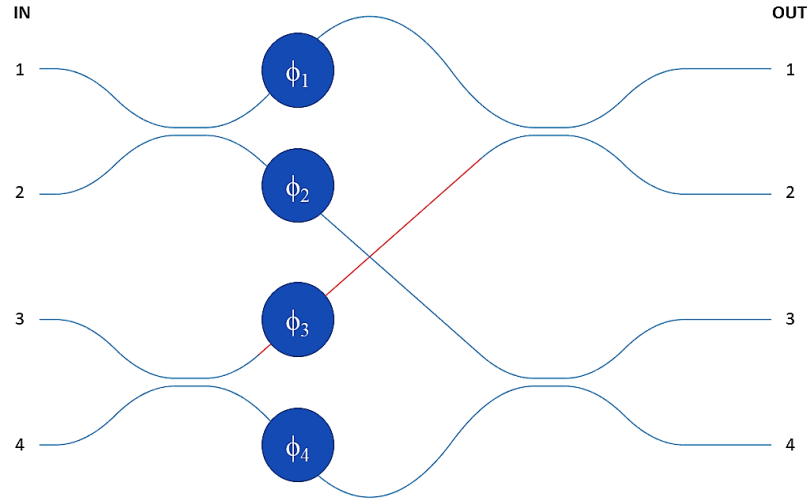
Figure 6.12: Schematic of the fabricated quarter. The presence of fabrication imperfections in the device is modeled as a phase term in each arm.

related to the imperfections will be:

$$
M_{\text{imperfections}} =
\begin{pmatrix}
e^{i\phi_1} & 0 & 0 & 0 \\
0 & e^{i\phi_2} & 0 & 0 \\
0 & 0 & e^{i\phi_3} & 0 \\
0 & 0 & 0 & e^{i\phi_4}
\end{pmatrix}
\tag{6.4.10}
$$

We can now calculate the total matrix as

$$
\begin{aligned}
M_{\text{quarter}} &= M_{\text{DCs}} \cdot M_{\text{bridge}} \cdot M_{\text{imperfections}} \cdot M_{\text{DCs}} \\
&= \frac{1}{2}
\begin{pmatrix}
e^{i\phi_1} & ie^{i\phi_1} & -e^{i\phi_4} & ie^{i\phi_4} \\
ie^{i\phi_1} & -e^{i\phi_1} & ie^{i\phi_4} & e^{i\phi_4} \\
-e^{i\phi_2} & ie^{i\phi_2} & e^{i\phi_3} & ie^{i\phi_3} \\
ie^{i\phi_2} & e^{i\phi_2} & ie^{i\phi_3} & -e^{i\phi_3}
\end{pmatrix}
\end{aligned}
\tag{6.4.11}
$$

We can recast this expression by fixing ϕ_4 in order to express $\Delta\phi_i$ as $\phi_i - \phi_4$. In

this case we can write:

$$
M_{\text{quarter}} = \frac{1}{2}
\begin{pmatrix}
e^{i\Delta\phi_1} & ie^{i\Delta\phi_1} & -1 & i \\
ie^{i\Delta\phi_1} & -e^{i\Delta\phi_1} & i & 1 \\
-e^{i\Delta\phi_2} & ie^{i\Delta\phi_2} & e^{i\Delta\phi_3} & ie^{i\Delta\phi_3} \\
ie^{i\Delta\phi_2} & e^{i\Delta\phi_2} & ie^{i\Delta\phi_3} & -e^{i\Delta\phi_3}
\end{pmatrix}
\tag{6.4.12}
$$

As before, introducing some phase-shift at the input and output port, we obtain:

$$
M'_{\text{quarter}} =
\begin{pmatrix}
-ie^{-i\Delta\phi_3} & 0 & 0 & 0 \\
0 & e^{-i\Delta\phi_3} & 0 & 0 \\
0 & 0 & 1 & 0 \\
0 & 0 & 0 & i
\end{pmatrix}
M_{\text{quarter}}
\begin{pmatrix}
ie^{-i\Delta\phi_2} & 0 & 0 & 0 \\
0 & e^{-i\Delta\phi_2} & 0 & 0 \\
0 & 0 & 1 & 0 \\
0 & 0 & 0 & -i
\end{pmatrix}
$$

$$
= \frac{1}{2}
\begin{pmatrix}
e^{i(\Delta\phi_1-\Delta\phi_2-\Delta\phi_3)} & e^{i(\Delta\phi_1-\Delta\phi_2-\Delta\phi_3)} & 1 & 1 \\
-e^{i(\Delta\phi_1-\Delta\phi_2-\Delta\phi_3)} & -e^{i(\Delta\phi_1-\Delta\phi_2-\Delta\phi_3)} & 1 & 1 \\
-1 & 1 & -1 & 1 \\
1 & -1 & -1 & 1
\end{pmatrix}
\tag{6.4.13}
$$

By defining the internal phase as a combination of the phase delay $\Delta\phi_i$, $\phi = \Delta\phi_1 - \Delta\phi_2 - \Delta\phi_3$, we are back to Equation 4.2.2. So by controlling the phase of the modes inside the quarter, we can control its internal phase thus selecting any equivalence class.